



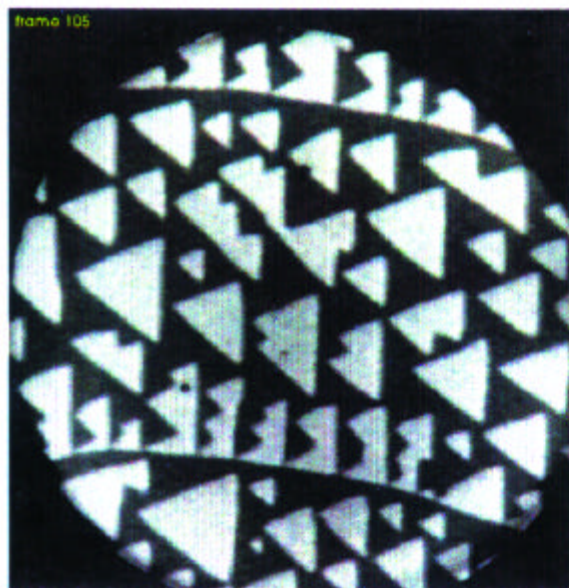
Physical and Chemical Sciences Center

Research Briefs

January 2000

**Sandia National Laboratories
Albuquerque, New Mexico**

A Department of Energy Multiprogram Laboratory



Research Briefs for the Physical and Chemical Sciences Center is published by Sandia National Laboratories. Additional complimentary copies are available by contacting:

S. Tom Picraux
Physical and Chemical Sciences Center, 1100
Sandia National Laboratories
Albuquerque, NM 87185-1427

Phone: (505) 844-7681
Fax: (505) 844-6098
E-mail: picraux@sandia.gov
url: <http://www.sandia.gov/1100/1100hp.htm>

Research Briefs

Editors

S. T. Picraux
J. A. Nichelason

Production

Bernadette Fulton

Cover Page: Low energy electron microscope images showing the decay of 7x7 domains during the 7x7 to 1x1 phase transition on Si(111). See page 62.

Message from the Director

The Physical and Chemical Sciences Center provides new scientific knowledge in support of Sandia's missions for the Department of Energy. We emphasize research to create and enable emerging technologies. We also provide new understanding needed to support predictive reliability for existing systems. The focus of our work derives from Sandia's role as a multiprogram laboratory with broad-based research and development responsibilities for nuclear weapons, non-proliferation, energy, environment and other areas of importance to the nation.

Within our portfolio of research investments, this issue of Research Briefs gives emphasis to our recent accomplishments supporting applied program needs. We address a focused set of strategic themes: science underlying materials performance and reliability, nanoscale structures and devices, advanced sensing science, and the science of semiconductor technologies. We employ a wide range of multidisciplinary capabilities based on the physical and chemical sciences, from first principles modeling and atomic scale measurement to remote laser sensing and nanoscale science and technology. Looking to the future, we are investing in the science that underlies future generations of integrated microsystems, and the microscopic-based physical models needed for predictive reliability of systems in a new era of teraflop computing.

The activities of the Physical and Chemical Sciences Center are supported by a diverse set of funding sources, and are managed to assure integration and synergy between projects. The research described here provides examples that illustrate the importance of a strong science base in physics and chemistry to the success of DOE's Stockpile Stewardship mission and its campaigns. The work also provides insights into the connections between science and the wider range of DOE technologies. In essentially all the research described, our partnerships with colleagues in universities, industry, and in program areas across the Labs have been critical, and we acknowledge with gratitude their collaboration.



A handwritten signature in black ink, which appears to read "S. Tom Picraux". The signature is written in a cursive style and is positioned above a vertical line.

S. Tom Picraux
Director

Table of Contents

Integrated Product Realization Environments

Model for Regulation of Deuterium Emission in the Neutron Tube	4
Pressure-Temperature Phase Diagram and Dielectric Properties of Chem Prep PZT 95/5-Nb	6
Shock Properties of Poled PZT Ferroelectric Ceramics	8
Scale-Up Challenges in Photonic Driver Techniques for Microshock Studies	10

Certification in Hostile Environments

Photocurrent Effects Microscopy	12
Single Event Upset Imaging of CMOS Memories Using Radiation Microscopy	14

Enhanced Surety Options for Stockpile

High Pulse-Power Semiconductor Laser Technology for Advanced Laser Diode Ignition	16
The Role of Self-Assembly on the Performance of Anti-Stiction and Anti-Friction Coatings for Micromachines	18
Optical Triggering of High-Voltage Switches	20

Lifetime Assessments of Materials, Subsystems and Components

Combinatorial Corrosion Science	22
Predicting Corrosion Initiation in Aluminum from the Oxide Electrical Properties	24
Multi-Phase Reactive Chemical Flow Modeling for Corrosion	26

Non Proliferation

TRIBICC Measurements of Charge Transport in Gamma-Ray Surveillance Monitors	28
GaN-Based UV Light-Emitting Devices	30
UV Fluorescence Lidar Field Test Measurements	32

Nanoscience Research

Total Destruction of a Toxic Chlorinated Organic Using Visible Light and Nanoparticles of MoS ₂	34
---	----

Table of Contents

6The Dynamics of Giant Spins on Magnetic Nanoclusters36
Enhanced Composition Modulation in InAs/AlAs Superlattices38
Simulation of H Behavior in p-GaN(Mg) at Elevated Temperatures40
Localized Corrosion Initiation at Nanoengineered Cu-rich Defects in Al Thin Films42
Fracture in III-Nitride Alloys Permits Dislocations to Relieve Tensile Stress44
Electronic Transport in Complex Molecular Solids46
Novel Energy Conversion Devices of Icosahedral Borides48
Thermophotovoltaic Materials and Device Development50
Terahertz Detection in Double Quantum Well Devices52
Exciton Mass in InGaAsN Photovoltaic Materials54
Tribological Properties of Self-Assembled Monolayers on Si56
Self-Assembly and Viscoelastic Response of Alkanethiol Monolayers58
Metal Deposition, Growth and Adhesion at Oxide Surfaces60
Atom Diffusion Controls Dynamics of Surface Phase Transition on Si (111)62
Membrane-Based Sensors for Detecting Heavy Metal Ions64
Gallium Nitride Epitaxial Lateral Overgrowth Kinetics66
Divertor Erosion Eliminated by Using Detached Plasmas on DIII-D68
Mechanical Properties of Alumina Films are Correlated Primarily to Film Density70
Electrostriction in Field-Structured Composites: Basis for an Artificial Muscle?72
 Recent Awards and Prizes74
 Resources and Capabilities76
 Physical & Chemical Sciences Center FY00 Budget-By Customer80



Integrated Product Realization Environments

Model for Regulation of Deuterium Emission in the Neutron Tube

Merle E. Riley

Motivation—The present-day dependence on large-scale computing has encouraged the simulation of many aspects of components and devices that were not previously subject to theoretical investigations. The low-temperature plasma that is present in the ion source region of the neutron generator tube is an example. Much early research was devoted to the properties of the deuterated scandium (ScD) storage layer but few studies were done to model or simulate the plasma environment. This plasma region is the key to both the delivery of energy to the layer and to the extraction of neutral D from the layer and transport of its ions to the accelerator region of the tube. Present ASCI efforts include the simulation of the low-temperature plasma as well as other aspects of the tube operation. The goal is a predictive capability for tube performance.

From early studies (D. Benson, SNLA) one has a kinetic basis for describing the neutral D release from the storage layer. In order to simulate the observed temporal behavior, however, it was necessary to invoke an ad hoc "flux regulation" parameter to restrict the D release. The argument was that the increased ion density over the source interacts with the arc discharge by some unknown mechanism, reducing the power input to the ScD surface. W. Wampler (SNLA) has improved this model by doing numerical 1D space and time solutions of the thermal and mass transport within the ScD layer. The flux regulation was included by a flux-dependent, one-parameter cutoff in the thermal input to the surface. With this parameter properly chosen, the results agree remarkably well with the observed temperature rise of the ScD layer during operation. The flux regulation assumption has seemed a mysterious part of the operation of

the device, as there is no mechanism that explains how the increased ion density above the ScD layer could produce the required reduction in power input to the layer itself.

Accomplishment—We have found that a model containing the source plasma, the ScD storage layer, and an external circuit explains the flux regulation. In addition, we have made improvements on the material properties for thermal and mass transport within the ScD layer and are posed to combine this code with the low temperature plasma simulation code that is in development. The explanation of the flux regulation became apparent when the operation of the discharge was simulated with a simple circuit model of the system. We approximated the plasma behavior by some simple global properties: (1) The thermal input to the ScD layer is proportional to the product of current and the voltage across the discharge gap. (2) The electric current is proportional to the emitted D flux from the active electrode. From these assumptions we find that the temperature and flux regulation of the arc source region of the tube is predicted. In other words, the mysterious flux regulation is just a consequence of having the discharge, the surface layer, and a circuit all within a consistent description of the system.

Significance—We have shown that a simple model of the plasma behavior predicts the flux and temperature regulation of the discharge. Thus we are confident that the ASCI plasma simulation, when combined with the circuit and ScD material model, will give a good description of the observed tube characteristics. At this point we will have a simulation capability for the neutron tube that will afford examination of design modifications to the device.

Sponsors for various phases of this work include: DP-Research Foundations and ASCI

Contact: Merle E. Riley, Laser, Optics and Remote Sensing Dept., 1128

Phone: (505) 844-8879, Fax: (505) 844-5459, E-mail: meriley@sandia.gov

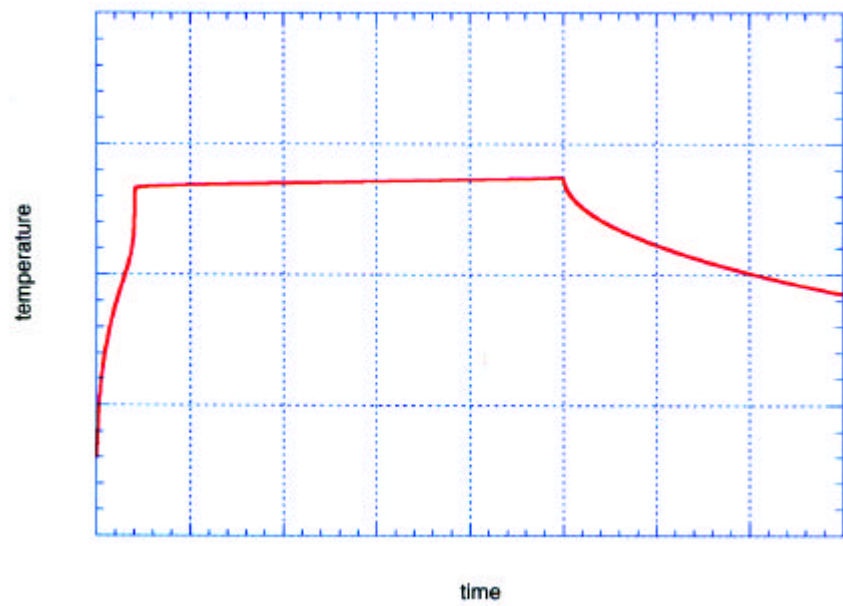


Figure 1. Surface temperature of ScD vs time from the material response simulation including circuit model.

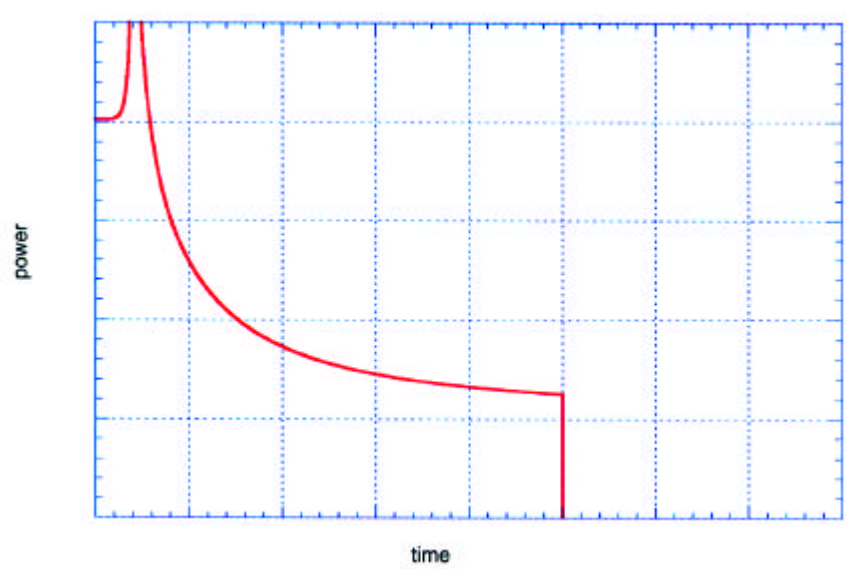


Figure 2. Power into the ion source discharge as predicted by the simple circuit model.

Pressure-Temperature Phase Diagram and Dielectric Properties of Chem Prep PZT 95/5-Nb

G. A. Samara, L. V. Hansen, J. A. Voigt, and B. A. Tuttle

Motivation—A substantial R&D effort is underway at Sandia to develop a reliable and reproducible process to replace the traditional multi-step, mixed-oxide processing route for producing PZT 95/5 ceramics for device applications. PZT 95/5 is a difficult material to produce requiring tight control over composition, density, and microstructure to meet device performance requirements. The new approach employs a non-aqueous chemical preparation (chem prep) route for synthesizing PZT 95/5 powder which is subsequently processed to produce the ceramic parts. Ceramics that meet electrical and mechanical requirements have been produced by this approach. We have begun a study of the dielectric properties and phase transitions of the new material to determine its pressure-temperature phase diagram and compare the responses to those of the conventional mixed-oxide PZT 95/5. In this initial study we investigated material that has a Zr-to-Ti ratio of 95.4 to 4.6 with a niobium substitution level of 0.019 processed into 94% dense ceramic form without the addition of a pore former.

Accomplishment—The Temperature-Pressure phase diagram for the chem prep PZT 95/5 studied is shown in Fig. 1. The phase boundaries were determined from anomalies in the dielectric constant, ϵ' , or dielectric loss, $\tan \delta$, measured as functions of temperature and hydrostatic pressure. Most of the phase transitions are thermodynamically first-order accompanied by substantial hysteresis between increasing and decreasing temperature or pressure. The hysteresis is depicted by the arrows marked on the various phase boundaries. Ferroelectric phases are designated by the letter F, antiferroelectric phases by the letter A, and the high temperature non-polar paraelectric phase by the letter P. The subscripts O, R1, R2

and T refer to the crystal symmetry of the various phases, namely orthorhombic, rhombohedral 1 and 2 and tetragonal, respectively. Each of these phases has a unique dielectric signature as shown in Figs. 2 and 3, and the phase boundaries are thus easily established. Overall, the phase diagram is qualitatively similar to that of conventional mixed-oxide PZT 95/5 shown by the wide, cross-hatched, light gray lines in Fig. 1. However, the quantitative differences are significant especially in the region of the F_{R1} - A_0 transition. From an applied point of view, this is the most important transition is the material. In pulse power sources this transition is induced by shock loading and results in the release of bound electrical charge. A significant result relevant to the application is that the A_0 phase does not revert back to the F_{R1} phase upon releasing the pressure at and below room temperature as shown in Fig. 3. The recovered phase at 1 bar is A_0 . Thermal cycling consisting of heating followed by cooling to room temperature at 1 bar is required to recover the F_{R1} phase.

Significance—Detailed characterization and understanding of the properties of the new chem prep PZT 95/5 are necessary for qualifying this material for device applications. Towards this end, there is a large body of data on conventional, mixed-oxide PZT 95/5, and it is prudent to capitalize on this data base as much as possible. It is important to learn about and understand both similarities and differences between the two materials and to take differences into consideration for both design and simulation purposes. The present work is a step in this direction, and it establishes the baseline for the temperature-pressure phase diagram for chem prep PZT 95/5.

Sponsors for various phases of this work include: DP-Research Foundations, PDP, ADAPT, and Advanced Exploratory Development

Contact: George A. Samara, Nanostructures and Advanced Materials Chemistry Dept., 1152

Phone: (505) 844-6653, Fax: (505) 844-4045, E-mail: gasamar@sandia.gov

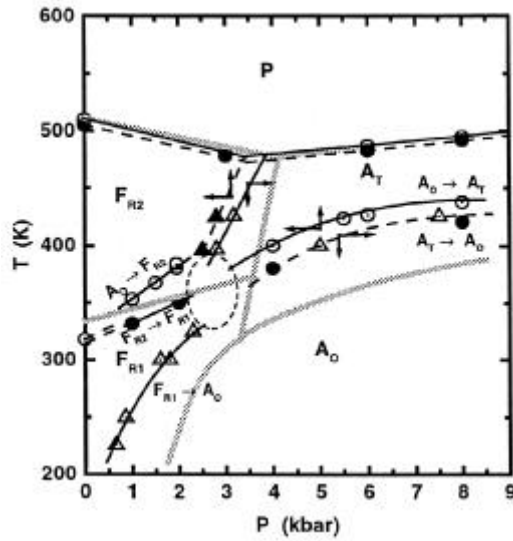


Figure 1. Temperature-Hydrostatic Pressure phase diagram for dense chem prep PZT 95/5 with 1.9 mol% Nb and no pore formers. Superimposed on this phase diagram (wide light grey lines) is the phase diagram for the standard, porous mixed oxide PZT 95/5 with 2% Nb.

Figure 2. Temperature dependence of the dielectric constant of dense chem prep PZT 95/5-1.9 Nb showing the signature of the F_{R2} -P transformation for the 1-bar and 3-kbar isobars. Note that while the F_{R2} -P transition temperature decreases with pressure, the A_T -P transition temperature increases with pressure.

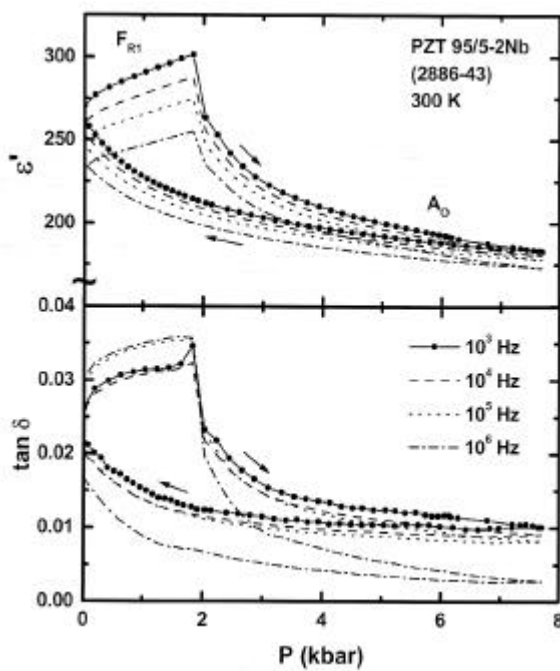
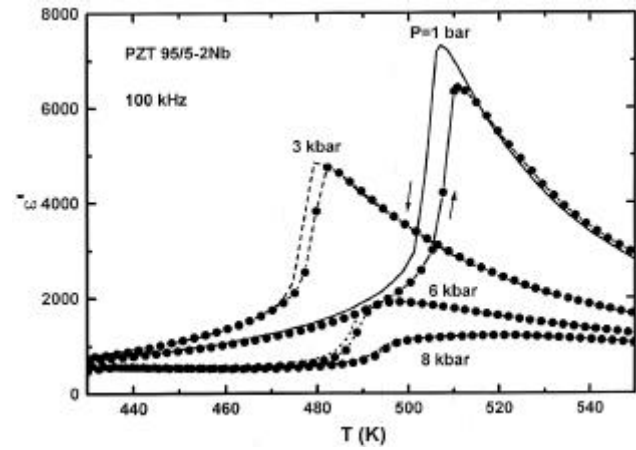


Figure 3. Pressure dependences of the dielectric constant (ϵ') and dielectric loss ($\tan \delta$) of dense, chem prep PZT 95/5-1.9Nb showing the signatures and irreversibility of the F_{R1} - A_0 transformation.

Shock Properties of Poled PZT Ferroelectric Ceramics

R. E. Setchell, S. T. Montgomery and R. J. Lawrence

Motivation—High voltages and currents are generated in pulsed power devices through the shock-induced depoling of ferroelectric ceramics based on PZT (lead zirconate - lead titanate). Although such devices have been in use for many years, challenging new design and certification requirements have motivated a significant effort to achieve accurate numerical simulations of device operation. In order to develop improved models for the complex behavior of poled PZT ceramics under shock loading, an extensive experimental program was started in FY97 to provide new insights and well-characterized data for these materials.

Accomplishment—During the first year, this study addressed the mechanical behavior of unpoled PZT 95/5 under uniaxial strain conditions. Planar impact techniques were used with laser interferometry (VISAR) to examine wave evolution over the range of shock pressures of interest. In the second year, emphasis was placed on shock-induced depoling of PZT 95/5 samples that were either normally or axially poled (poled perpendicular or parallel to the intended shock motion, respectively). Different passive resistive loads were used with normally poled targets to vary the internal electric field strengths. Axially poled targets had short-circuit external conditions, but generated very strong, opposed electric fields on either side of the shock within the samples. In the past year, selected experiments were performed on both normally and axially poled PZT 95/5 to facilitate development of a more comprehensive model for this material. Figure 1 shows shock-induced currents from axially poled material passing through a shorted external circuit. Figure 1a shows a prior result in which the current is strongly inhibited as impact stresses increase

above 0.9 GPa. Shock-induced conductivity has been suggested for the abrupt changes at higher stresses. Figure 1b shows currents from repeat experiments in which much smaller electric fields were generated by using samples with a reduced remanent polarization. The higher stress profile suggests both a field and a strong stress dependency in the current-limiting process. Other experiments on PZT 95/5 this past year have extended the peak fields generated during normally poled experiments, and have examined the effect of shock rise time on an early high-voltage breakdown mechanism. Experiments were also performed on other PZT compositions, PBZT and PSZT (containing barium or tin), that are used in pulsed power devices. Figure 2 shows currents generated in normally poled PSZT experiments. Figure 2a shows a reduction in depoling currents with lower shock stresses and higher electric fields, as observed in PZT 95/5. Figure 2b shows currents from three-dimensional experiments in which shock amplitudes decayed due to lateral unloading as the waves propagated down long, thin samples. The high-field case showed current slowly rising as expected due to the capacitance of the PSZT sample, then falling rapidly due to the stress and field effects shown in Figure 2a.

Significance—Successful simulation of the extensive data base now available will represent a significant milestone in the effort to accurately predict the operation of pulsed power devices. Current experimental studies are adding the additional complexity of extreme temperatures, and corresponding model development could bring to fruition a unique capability for meeting design and certification responsibilities.

Sponsors for various phases of this work include: MAVEN and DP Research Foundations

Contact: Robert E. Setchell, Nanostructures and Advanced Materials Chemistry Dept., 1152

Phone: (505) 8443847, Fax: (505) 844-4045, E-mail: resetch@sandia.gov

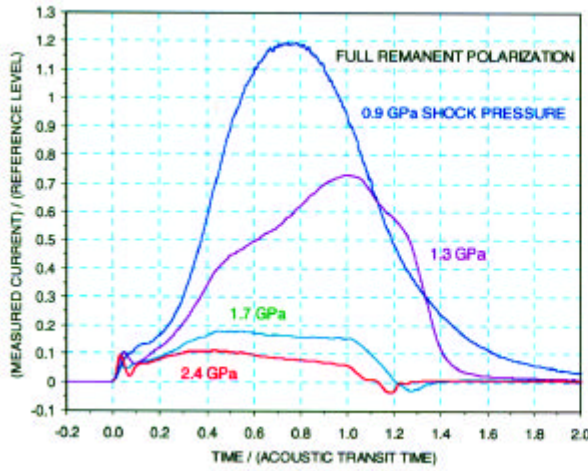


Figure 1a. Shock-induced currents from axially poled PZT 95/5 samples. The reference level is from the simplest short-circuit model and is determined from sample dimensions, initial polarization, and shock velocity.

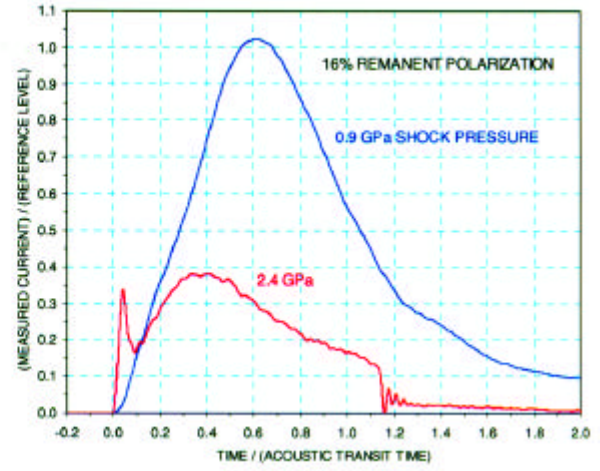


Figure 1b. Currents from axially poled PZT 95/5 samples with a much smaller remanent polarization.

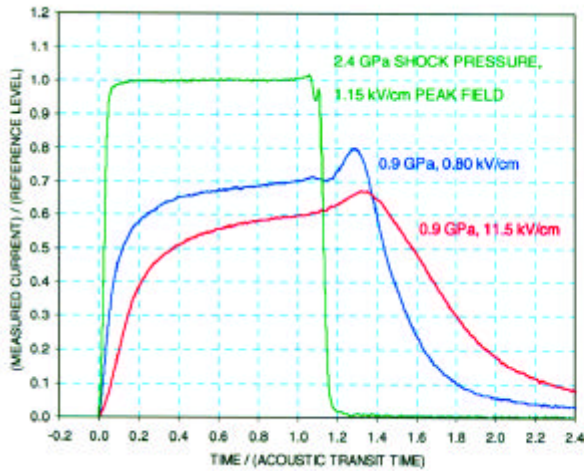


Figure 2a. Shock-induced currents from normally poled PSZT samples. Different load resistors were used to vary the electrical field strengths.

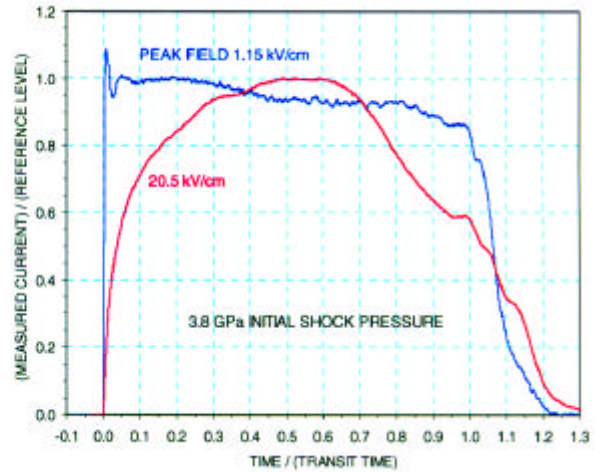


Figure 2b. Currents from three-dimensional targets in which shock amplitudes decay during passage through the samples.

Scale-Up Challenges in Photonic Driver Techniques for Microshock Studies

R. E. Setchell and W. M. Trott

Motivation—Shock wave physics is fundamental to critical Sandia responsibilities, from the specific need to design and certify shock-actuated devices to the more general need to certify systems subjected to shock loading in normal and abnormal environments. For many years the basic research tool for shock physics has been the gas gun, where materials of interest are subjected to planar shocks through the high-velocity impact of flat-faced projectiles. In recent years, however, high operational costs have led to a significant reduction in the number of gas gun facilities at Sandia and elsewhere. At the same time, the development of microscale electro-mechanical systems has led to important possibilities for technology replacements. Eventual certification of microscale systems could be challenging, however. The shock properties are unknown for basic structural materials such as polycrystalline silicon film, and this material cannot be made in bulk samples large enough for conventional shock testing.

A research program was started in FY99 with the goal of developing a shock-physics capability that would address both the high cost of conventional shock techniques and the need to study the shock properties of microscale materials. This program is based on earlier Sandia work that developed optical detonators incorporating laser-driven metal flyers. To accelerate flyer materials with useful dimensions to adequate impact velocities, laser (photonic) driving conditions must be scaled-up several orders of magnitude beyond detonator levels. The primary scale-up challenges are to develop a beam delivery and launch system that produces a very uniform laser intensity over the flyer area, and to do so in a manner that avoids laser-induced damage in the delivery optics.

Accomplishment—The first-year objective was to demonstrate photonic driving of metal flyers using laser energies of at least 250 mJ (roughly one order of magnitude beyond detonator conditions). The cavity of a commercial, Q-switched, 1.5 Joule/pulse Nd:glass laser was modified to produce more desirable beam properties (a very multimode beam having an air breakdown threshold nearly ten times higher than previously). This beam is shown in Fig. 1. To achieve a uniform intensity at a flyer we chose to use a "beam conditioning" optical fiber. Taking 50 J/cm² as an upper limit for average fiber fluence before laser-induced damage, we obtained pure fused-silica fiber having an 800-micron diameter core. To successfully inject the beam shown in Fig. 1 into this fiber we needed injection optics that would mitigate the high local fluences. A special diffractive optic was designed and fabricated for this purpose. The flat intensity profile achieved at the exit face of the fiber is shown in Fig. 2. Finally, low-aberration lenses were used to re-image the fiber exit face onto the rear surface of an optical substrate where metal flyers have been deposited. Figure 3 shows a profile at a clear location on this surface. With a 250 mJ laser pulse, a 100-micron-thick aluminum flyer can be accelerated to 1.0 km/s, producing an 8.0 GPa shock sustained for 30 ns in an aluminum target.

Significance—The initial goal of demonstrating photonic driving conditions at a pulse energy of 250 mJ was achieved. This capability is adequate for addressing shock properties in microscale materials up to 10s of microns thick. To address a broader range of materials, the present goal is to achieve another order of magnitude in photonic driving levels.

Sponsors for various phases of this work include: LDRD

Contact: Robert E. Setchell, Nanostructures and Advanced Materials Chemistry Dept., 1152
Phone: (505) 8443847, Fax: (505) 844-4045, E-mail: resetch@sandia.gov

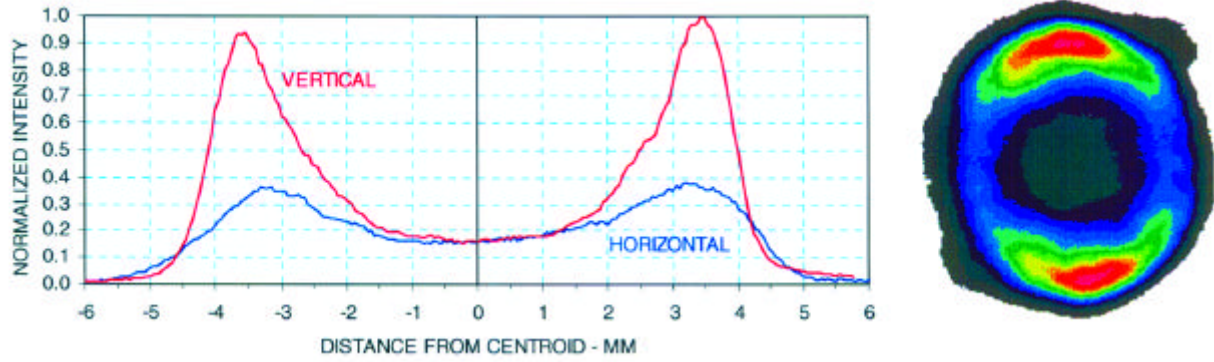


Figure 1. Near-field beam profile of the 1.5 Joule Nd:glass laser

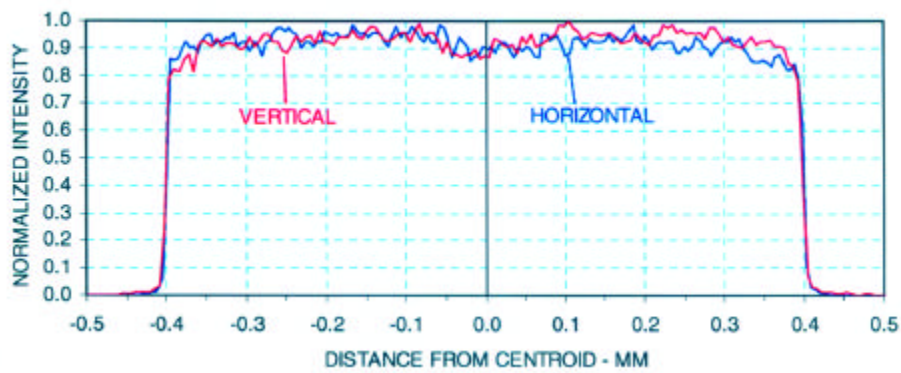


Figure 2. Beam profile at the exit face of the 800-micron-diameter conditioning fiber

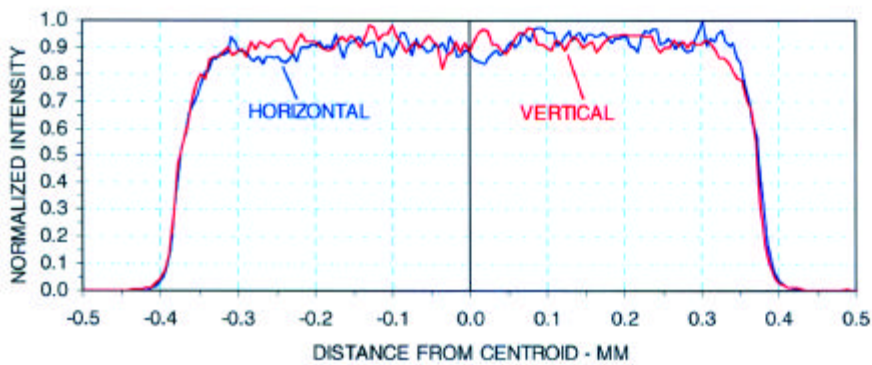


Figure 3. Beam profile at the substrate/flyer interface



Certification in Hostile Environments

Photocurrent Effects Microscopy

S. N. Renfrow, W. Beezhold, P. E. Dodd, and D. S. Walsh

Motivation—Modeling and simulation tools are increasingly necessary in the design of microelectronic devices, circuits, and subsystems. In the area of radiation hardening for x-rays and gamma-rays, existing prompt photocurrent modeling and simulation tools fall short at high dose rates [$> 10^9$ rad(Si)/s]. The most promising device level and circuit code for high dose rate conditions is Davinci. However, Davinci, a 3-D numerical code used primarily for cosmic ray upset analysis, has not been rigorously applied (nor validated) to the study of x-ray and gamma ray induced photocurrents. Key phenomena in Davinci include the non-linear effects of the variation of lifetime with injection level, internal electric fields, the variation of mobility and diffusion constants with injection level, and conductivity modulation.

Accomplishment—A newly developed capability on our accelerator-microbeam, called Photocurrent Effects Microscopy (PEM), now provides us with the ability to supply enormous doses (~giga-rads) of pulsed (~seconds) ionizing radiation to selected micro-regions of a device. We have developed the microbeam as a dose-rate radiation source with the capability to produce 5×10^8 rad/s with pulses as short as 150 ns. We expect higher dose rates with further development. PEM will be used to validate Davinci for the application of making high dose rate prompt photocurrent predictions for devices and circuits. The initial PEM data runs were made with a 35 MeV Cl beam for several reasons. First, it is one of the most abundant beams available from the tandem accelerator. Second, it is focusable with the microbeam quadrupole. And third, it has a range of ~ 10 μm in Si,

which deposits energy in regions of interest. The beam pulsing system is a parallel plate deflector controlled by a high voltage switch with a variable pulse length of 150 ns to infinity. The beam spot diameter can be varied from 50 μm to 500 μm . Figures 1 and 2 show plots of data taken on a 3.6 mm x 3.6 mm PIN diode. In Fig. 1 only the 0.5 nA pulse follows the deflector pulse. Fig. 2 shows the response fall off from the beam damage of the PIN during a long pulse. We will compare PEM results with new full-area experiments on the same devices using SPHINX, and other offsite facilities. We will also examine the analytical photocurrent codes (Wunch-Axness, e.g.) and identify their applicability at high dose rates.

Significance—Prior to our work, there were no experimental tools to generate photocurrents in a selected micro-region of a device to fully test Davinci. Improved and validated codes will provide weapon designers with high fidelity computational tools that address hostile radiation requirements with minimum build and test cycles. Model-based design trade-off studies at Sandia for new microelectronic devices could in principle be significantly cheaper, with months to years shorter development times. Also, another potential application of PEM is the localized reduction of photocurrents in selected regions of a device (see Fig. 2). Killing undesired photocurrents could raise the dose rate tolerance of the device without effecting the overall performance. Finally, prior to this work, there were no radiation sources able to produce arbitrarily long pulses of ionizing radiation for sustained dose studies.

Sponsors for various phases of this work include: LDRD, DP Physics S&T, and WREMS

Contact: David Walsh, Radiation-Solid Interactions Dept., 1111

Phone: (505) 844-9590, Fax: (505) 844-7775, E-mail: dswalsh@sandia.gov

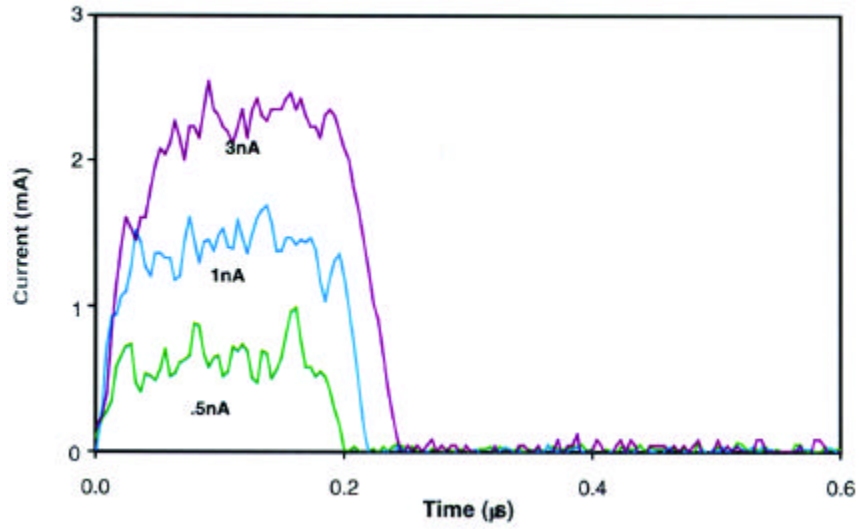


Figure 1. 200 ns pulses of 35 MeV Cl on PIN with 25 V bias in a 300 μm x 300 μm spot. The plot shows direct photocurrent measurement.

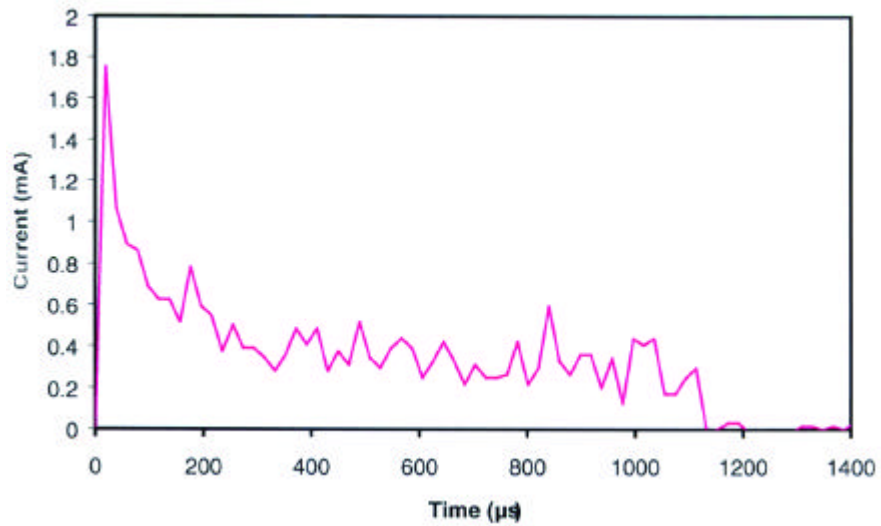


Figure 2. 30nA, 1 ms pulse of 35 MeV Cl on PIN with 10 V bias in a 60 μm x 60 μm spot. The beam damage quickly lowers the photocurrent.

Single Event Upset Imaging of CMOS Memories Using Radiation Microscopy

D. S. Walsh, P. E. Dodd, M. R. Shaneyfelt and B. L. Doyle

Motivation—The operation of electronic devices in space and hostile radiation environments is a primary concern for Sandia integrated circuit designers. The charge deposited by high energy ion strikes to a VLSI transistor, depending upon the location of the ion strike, may induce a change of logic state (a single event upset) in, for example, a SRAM cell. Complex, three-dimensional models (e.g. DAVINCI) of device and circuit responses to individual ion strikes have been developed and are currently used to predict the radiation hardness thresholds of VLSIC designs. Validation of these models depends at least partly upon the ability to measure the response of individual transistors and other test structures to ion strikes at precisely known locations. Broad-beam testing of CMOS static memories is a well established technique for measuring the ion-induced upset threshold of the memory design. The technique does not however, directly provide information concerning the sensitivity of specific structures within a SRAM. Therefore, we have two driving forces for the development of techniques to measure dependence of ion-induced charge collection and upset response of devices upon ion strike location.

Accomplishment—In response to these needs we have developed Radiation Microscopy techniques which utilize a scanned, high energy ion microprobe to map (1) the amount of charge collected (IBICC imaging) and (2) single event upset occurrence (SEU imaging) in correspondence with the exact location of individual ion strikes. Positional accuracy of our system is on the order of one micron. We are capable of

imaging strikes with ions of ≤ 30 LET-Si (LET-Si is a measure of the charge a single ion deposits in a Silicon device). The facility has been used to image the SEU sensitivity of parts from SNL, Motorola, Texas Instruments and Hughes Space. In fact, the Hughes experiment set a world record for SEU imaging as a function of device speed (10 GHz). Ion induced charge collection experiments on CMOS, extreme ultraviolet lithography, and SOI transistor test structures and SEU imaging of single cell memory test structures have been and will continue to be performed. These measurements are designed to help validate the DAVINCI codes.

Significance—Routine broad-beam testing of the SNL SA3953 256k-bit SRAM at the Brookhaven National Laboratory suggested that some portion of the control circuitry was much more sensitive to single-event upset (SEU) than the memory cells, which are rad-hardened by feedback resistors (the small, lower threshold "knee" in the data displayed in Fig. 1). Subsequent Radiation Microscopy here at SNL successfully pinpointed the specific n-channel transistors (associated with data output latch/buffer circuits-Fig. 2) responsible for the unexpectedly poor SEU performance of the SRAM. It is estimated that by using the radiation microscopy to correctly identify the critical circuitry that was limiting the SEU threshold response of the SRAM, \$1,000,000 in cost has been saved in the manufacturing/test cycle for this SRAM. The radiation microscopy program provides a unique capability to diagnose SEU, and is an important tool for calibrating 3-D models supported by ASCI.

Sponsors for various phases of this work include: DP Research Foundations, LDRD, MAVEN, and WREMS

Contact: David S. Walsh, Radiation-Solid Interactions Dept., 1111

Phone: (505) 844-9590, Fax: (505) 844-7775, E-mail: dswalsh@sandia.gov

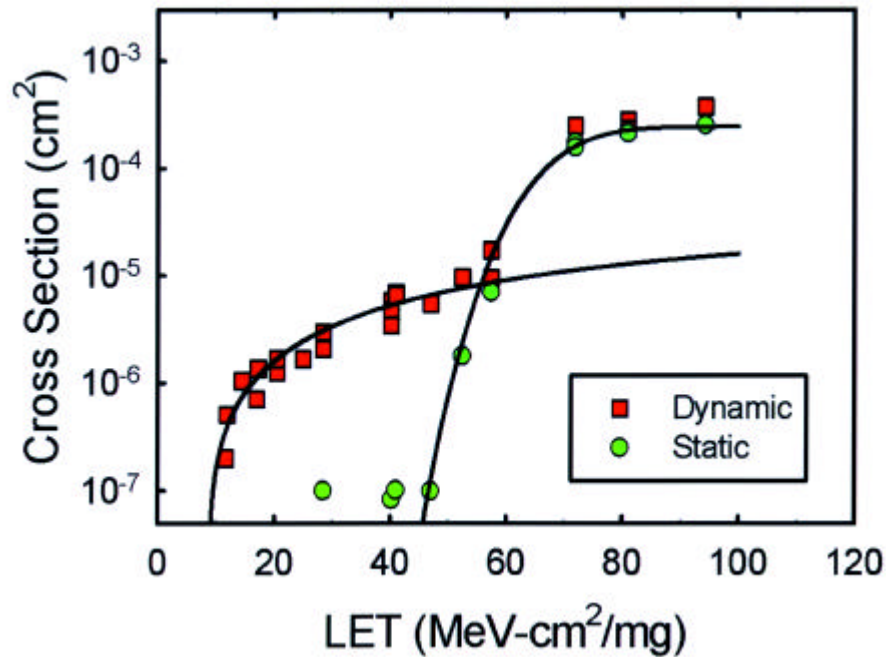


Figure 1. A plot of sensitive area versus LET upset threshold from broad-beam testing of the SNL 256k SRAM. These results show that unexpectedly, a small area of the chip causes upsets below the 50-55 LET threshold for the memory cells.

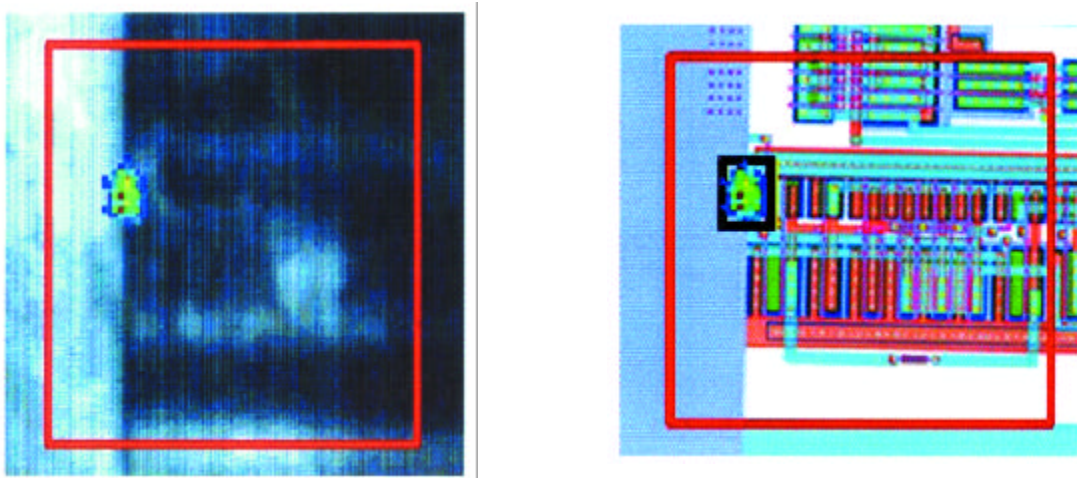


Figure 2. (a) Overlay of single event upset events measured using the ion microprobe with 43 MeV Cl^{+7} ions (LET=18) on a camera image of the 256k SRAM taken during the ion exposure. (b) Overlay of the same upset image on the SRAM design mask layout. The upsets are occurring in the enable read control latch circuitry of the SRAM, not in the memory cells themselves which have an upset threshold of ~55 LET. The red square indicates the extent of the microprobe scan.

Enhanced Surety Options for Stockpile



High Pulse-Power Semiconductor Laser Technology for Advanced Laser Diode Ignition

W. W. Chow, G. A. Vawter, F. J. Salas, and J. A. Merson

Motivation—We are attempting to develop high-pulse-power laser-diode systems for extending the optical ignition of pyrotechnics and explosives to higher threshold materials and faster function times. By furthering as well as integrating semiconductor-laser and waveguiding technologies developed at the Compound Semiconductor Research Laboratory (CSRL), it may be possible to achieve a factor of 5 improvement in laser output power over what is currently commercially available for laser diode ignition (LDI). This will enable a dramatic increase in the utilization of LDI in critical systems where immunity to stray electrical sources is vitally important.

LDI components are already slated to perform several important functions in Sandia's weapon systems, as well as in many commercial and Department of Defense (DoD) areas. Present applications include gas-actuator subsystems within Sandia weapon systems, and explosive-transfer functions for NASA X38, DoD aircraft crew escape systems and commercial launch vehicles. A major road block preventing more widespread use of LDI is insufficient laser output power, which limits our ability to increase operational ignition margins, ignite less sensitive explosives, and decrease function times.

Accomplishment—Work on this project is in the very preliminary stage, since currently there is no funding for proof-of-principle experiments. Several ideas for high power laser structures were considered. A promising scheme, which we wish to pursue, involves a

vertically (i.e. in the growth direction) stacked array of broad-area laser diodes. Novel to this approach is the growth of the epitaxially-stacked lasers in a monolithic chip, where highly-doped tunnel junctions enable current injection through pn junctions stacked in series. Such tunnel junctions have been used in quantum-cascade mid-IR lasers to recycle injected carriers but have yet to be applied to closely couple individual lasers. We would also like to investigate a second technology involving mode-expansion lasers based on the TRAFFiC concept (developed with past LDRD funding), where multiple ridge lasers share a common large-volume waveguide. Either approach is expected to surpass the 20mW-per- μm -width limit for commercial lasers.

Significance—The successful development of a semiconductor laser system capable of producing greater than 5 watts from a 50 μm diameter optical fiber will have important implications to LDI, and will put Sandia in the forefront of this technology. Applications include the surety area because an increase in available laser power will improve reliability and lead to greater handling safety of igniter components. The capabilities of shorter function times and ignition of high threshold materials have stockpile-improvement applications. The increased system flexibility resulting from higher laser power will help LDI make a significant leap forward, towards being the dominant technology for ignition of energetic materials. High power laser diode sources also have many non-explosive-related uses, e.g., in chemical sensing and medicine.

Sponsors for various phases of this work include: DP Research Foundations

Contact: Weng Chow, Semiconductor Material and Device Sciences Dept., 1113

Phone: (505) 844-9088, Fax: (505) 844-3211, E-mail: wwchow@sandia.gov

[This page intentionally left blank]

The Role of Self-Assembly on the Performance of Anti-Stiction and Anti-Friction Coatings for Micromachines

B. C. Bunker, R. A. Assink, J. A. Martin, G. Gulley, M. L. Thomas, M. Hankins, and M. De Boer

Motivation—Self-assembled monolayers (SAMS) based on the fluorinated coupling agent FTDS are being investigated as coatings to relieve the serious problems of stiction and friction in micromachines. Under ideal conditions, such fluorocarbon coatings can provide extremely low friction and adhesion. Unfortunately, the coating process has been highly irreproducible, creating serious problems for the micromachine fabrication line. The purpose of this investigation is to understand the factors leading to poor coatings and to develop more reliable coating processes.

Accomplishment—Factors known to influence the quality of SAM coatings include the deposition temperature, the solvent used, the solvent water content, FTDS concentrations, surface preparations, and even what container the Si substrates are coated in. Sorting out the complex sequence of events leading to the production of FTDS coatings required the use of a range of techniques to probe the physics and chemistry of both the solution and the substrate. ^{17}O nuclear magnetic resonance measurements performed on coating solutions containing H_2^{17}O (Fig. 1) were used to monitor the kinetics of hydrolysis and condensation of the trichlorosilane head group. The NMR results suggested that in isooctane, the head group is converted into a hydroxysilane with -OH groups that can hydrogen bond to each other and to -OH groups in the thermal oxide on Si.

Light scattering experiments on the coating solution show that when hydrolyzed FTDS concentrations exceed the critical micelle concentration, there is a burst of nucleation to form spherical aggregates of FTDS molecules.

Atomic force microscopy results show that the spherical aggregates then deposit on substrate surfaces. The radius of the deposited aggregates is comparable to the radius of gyration of the objects seen in solution, as is the induction time for their formation. Typical aggregates are 300 nm in diameter and 20-30 nm thick.

FTDS coatings containing the aggregates have been shown to exhibit poor anti-stiction properties in tests performed on micromachined beams. Therefore, processing conditions need to be controlled to stabilize true monolayers relative to alternate structures such as inverse micelles and vesicles. Monolayers can be deposited directly by using fresh FTDS solutions and minimizing the solvent water content to maximize the induction time prior to micelle formation. If thick aggregates are deposited, we have demonstrated that it is possible to use rapid thermal processing to reorganize the micelles into multilayer and then monolayer structures. Other modifications predicted to enhance monolayer formation include increasing the chain length of the coupling agent, using mono- and dichlorosilane head groups, and using more polar solvents to inhibit micelle formation.

Significance—The poor reproducibility of chlorosilane coating processes has long plagued researchers who are trying to produce SAMS to control a wide range of surface properties including adhesion and friction. This work has uncovered one of the underlying mechanisms for the formation of poor coatings and has identified several critical parameters, such as solvent water content and processing time, that control whether monolayers or alternate aggregate structures such as micelles are produced.

Sponsors for various phases of this work include: LDRD

Contact: Bruce C. Bunker, Biomolecular Materials and Interfaces Dept., 1115

Phone: (505) 284-6892, Fax: (505) 844-5470, E-mail: bcbunke@sandia.gov

Reaction Kinetics (2 mM FTDS in wet isooctane)

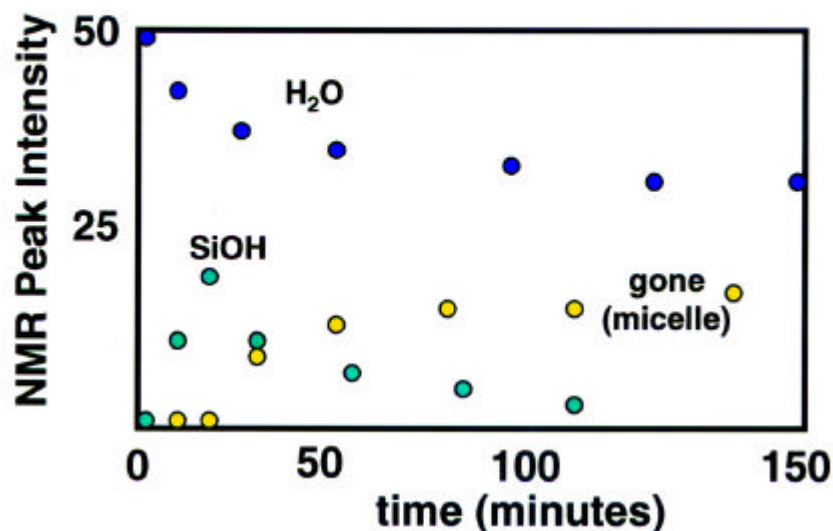


Figure 1. ^{17}O NMR peak intensities as a function of time for isooctane solutions containing 60 ppm water and 2 mM FTDS. Water disappears as it reacts with Si-Cl bonds to form Si-OH + HCl. The Si-OH signal disappears as hydrolyzed FTDS forms micelles in solution.

Tapping Mode AFM Image

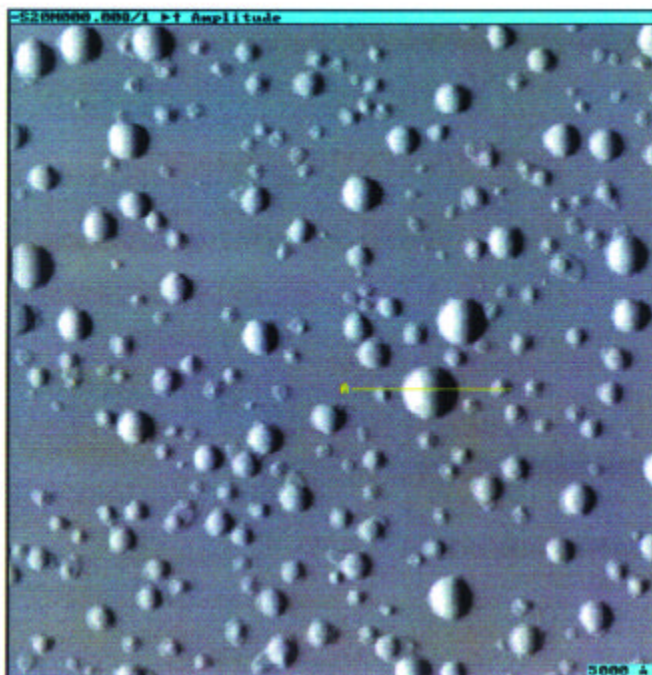


Figure 2. Tapping mode AFM image of Si substrate after one hour exposure to a 1 mM solution of FTDS in isooctane. Object bisected by line is 300 nm in diameter and 25 nm thick.

Optical Triggering of High-Voltage Switches

J. R. Woodworth and R. L. Schmitt

Motivation—Advanced weapon architectures increasingly rely on optical transmission of both signals and power to improve safety and reliability. By eliminating electrical connections between key firing set components, one minimizes the risk that spurious electrical signals (generated by lightning, for example) may cause a malfunction.

As part of the Advanced Firing/Detonation Systems (AF/DS) project, we are developing optically triggered high-voltage switches (sprytrons) to replace electrically triggered switches, thereby enabling an all-optical firing set. This work builds on our expertise in both plasma physics and miniature laser technology.

Accomplishment—We have designed, built, and characterized a miniature laser and specially optimized vacuum switches and we have demonstrated laser triggering of these switches under a variety of conditions, including transmission of the optical trigger pulse through a fiber. A layout of the optically triggered sprytron is shown in Fig. 1. A diode-pumped micro-laser produces a short (~ 2 ns wide) Q-switched laser pulse that is launched into a fiber optic and transmitted to the switch location. The light exiting the fiber is then focused onto the cathode of the vacuum switch, and the plasma generated by the focused laser beam triggers the switch.

Working with engineers in Division 2000, we modified existing sprytron designs to allow laser triggering by adding a hole in the anode and a window allowing optical access to the cathode. Also, based on modeling we optimized the electrode geometry to provide a factor-of-two increase in electric field strength near the trigger

area, significantly lowering the trigger threshold. In spite of the modifications, this sprytron still retains the advantages of vacuum switches: resistance to ionizing radiation, high current capacity, and small size.

Using the micro-laser and other q-switched lasers, we characterized the trigger requirements and performance of optically triggered switches over a broad range of laser pulse lengths, pulse energies and focal spot sizes. One of the most important results of our work, summarized in Figure 2, is the fact that triggering threshold depends on the focal spot intensity, not the total energy of the laser beam. This implies that very small lasers may be used to trigger sprytrons, a benefit from a packaging standpoint. It also shows that only sources of extremely high intensity (i.e. short-pulse lasers) will be able to trigger the switch, strengthening the safety theme this technology supports.

We have demonstrated laser triggering with as little as 2 μ J incident on the switch. For some switch designs, we have measured delay times as low as 5 ns and timing jitter as low as 0.5 ns, both significantly better than in electrically triggered switches. Also, we have shown that the lifetime of laser triggered switches is in excess of 1000 shots with little degradation in performance, important for testing the devices.

Significance—The optically triggered sprytron is an exciting development that will enable the design of an all-optical firing set, an important element in modern weapon architecture safety themes. To further demonstrate its efficacy, we plan to use the technology to switch an optically coupled firing set sometime in FY00.

Sponsors for various phases of this work include: DP Research Foundations and Advanced Exploratory Development

Contact: Joe R. Woodworth, Laser, Optics and Remote Sensing Dept., 1128

Phone: (505) 844-1243, Fax: (505) 844-5459, E-mail: jrwoodw@sandia.gov

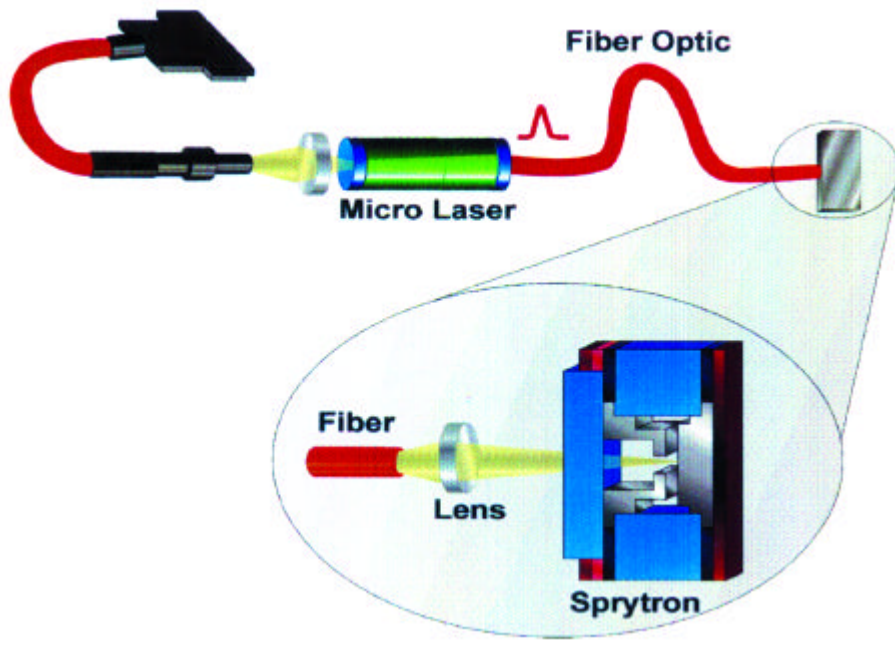


Figure 1. Layout of optically triggered vacuum switch. A diode-laser-pumped micro-laser generates a short pulse of intense laser light. This optical pulse is transmitted to the sprytron through a fiber optic. The inset shows how the trigger light from the fiber is focused onto the cathode of the sprytron.

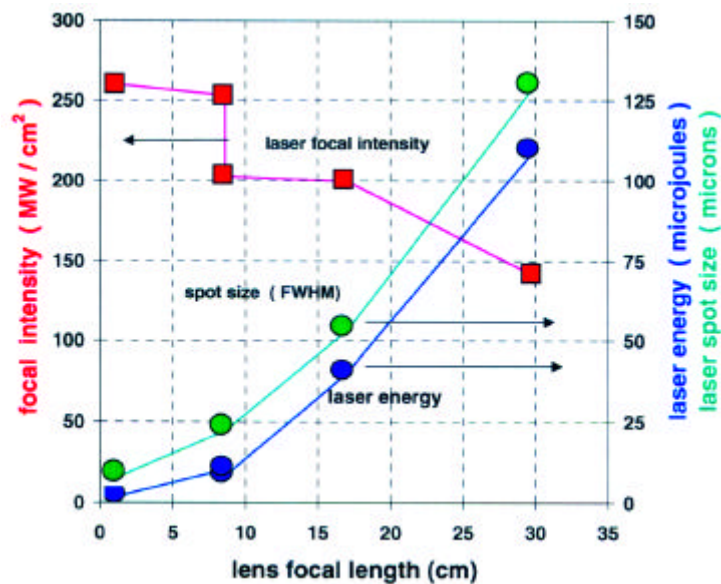


Figure 2. The triggering requirements of the sprytron depend on the laser focal intensity, not the total energy. As a result, relatively modest (several μJ) laser energy can be used to trigger the switch as long as a small focal spot is produced on the cathode.

Lifetime Assessments of Materials, Subsystems & Components



Combinatorial Corrosion Science

*J. C. Barbour, J. P. Sullivan, J. W. Braithwaite, N. Missert,
J. S. Nelson, R. G. Dunn, K. G. Minor, G. Copeland, and S. Lucero*

Motivation—Corrosion studies are inherently difficult because of complex interactions between material interfaces and the environment. A combinatorial approach is demonstrated in this work to examine copper sulfidation (a form of corrosion) using micron-scale Cu lines that are exposed to a humid air environment containing sub-ppm levels of H_2S . The relative rate of Cu_2S growth is determined from the change in resistance of the line.

Accomplishment—Parallel microscopic experimentation (the combinatorial approach often used in solid-state science) was applied to characterize atmospheric copper sulfidation. Specifically, this technique measured relative sulfidation rates for copper containing different levels of point defects and impurities (In, Al, O, and D). The data suggests that vacancy trapping by In and Al impurities slows the sulfidation rate, while excess point defects or deuterium increase the sulfidation rate.

Figure 1 shows a schematic representation of the combinatorial defect experimental matrix, at left. Each element of the matrix contains a patterned resistance line made from a Cu film. The change in resistance was monitored simultaneously for all meander lines to provide an instantaneous, in-situ metric of the amount of sulfide formation. These resistance lines were ion implanted with different species to either form additional point defects in the copper (Cu), impurities (D and O), or serve as Cu vacancy traps (Al and In).

The results of the Cu meander line experiments are shown in Fig. 2(a) and (b). Figure 2(a) shows the change in area, measured from the change in resistance, falls nicely into three

distinctive groupings: (I) rapid change in area for D and Cu implanted samples (upper two curves), (II) moderate change in area for the two control samples (with and without continuous current flow) and the O-implanted sample, and (III) slow change in area for Al and In implanted samples (bottom two curves). Figure 2(a) shows that the In and Al are effective at slowing the sulfidation reaction. For an equivalent amount of damage as created by the In implant, the Cu implantation causes the reaction rate to increase, and notably more quickly than the unimplanted control samples. The flow of current through the lines did not measurably affect the rate of sulfidation nor did the O implantation. However, the D implantation, which produced the least amount of damage, had a sulfidation rate as high as the most damaged Cu-implanted sample. If the initial width of the line is unchanged then the resultant change in resistance can be used to calculate the sulfide thickness as a function of time, shown in Fig. 2(b).

Significance—These experiments demonstrate that it is possible to use micro-combinatorial techniques to efficiently characterize mechanistic aspects of atmospheric copper sulfidation. In this study, the electrical resistance change in micron-sized Cu meander lines illuminated the relative sulfidation rate for Cu with different types of impurities and levels of point defects. The use of the small-size lines proved beneficial because all of the experiments could be performed in-situ, simultaneously, and thereby eliminated questions concerning reproducibility of the corrosion environment. Thus, the micro-combinatorial technique helps to create internal standardization for determining relative corrosion behavior.

Sponsors for various phases of this work include: LDRD and DP Research Foundations

Contact: J. Charles Barbour, Radiation-Solid Interactions Dept., 1111

Phone: (505) 844-5517, Fax: (505) 844-7775, E-mail: jcbarbo@sandia.gov

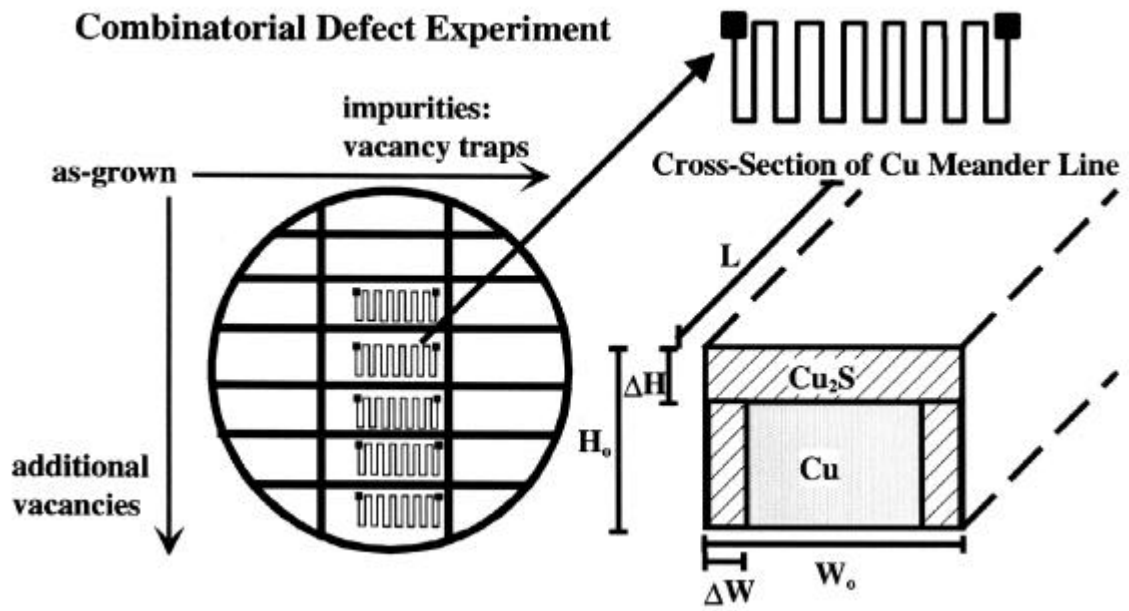


Figure 1. Schematic representation of the combinatorial defect experimental matrix (left). An expanded plan view of a Cu resistance meander line is shown in the upper right. The schematic cross-sectional view of one leg of the resistance line (lower right) also indicates the physical length parameters used to determine a correlation between resistance and the quantity of Cu_2S formed.

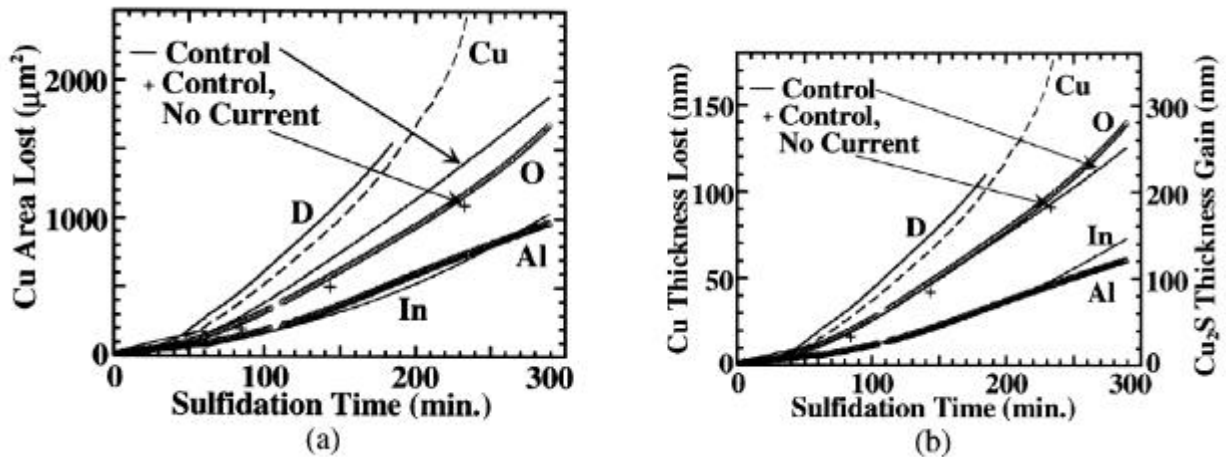


Figure 2. Quantity of Cu lost to sulfidation as determined from change in resistance of ECR-oxidized and implanted meander lines: (a) cross-sectional area, and (b) thickness reduction assuming negligible reduction in line width.

Predicting Corrosion Initiation in Aluminum from the Oxide Electrical Properties

J. P. Sullivan, R. G. Dunn, J. C. Barbour, and N. Missert

Motivation—The mechanism for the initiation of localized corrosion in pure Al is largely unknown. As a result, the ability to theoretically predict the onset of localized corrosion in Al from first principles has not proven possible. This work has focused on the study of electronic defects within the passive Al oxide layer and how localized corrosion (pitting) may be predicted from combined solid state and electrochemical measurements.

Accomplishment—It was discovered that the electronic defect density within Al oxide layers on Al changes as a result of electrochemical polarization and that combined solid state and electrochemical measurements may allow prediction of the potential at which Al undergoes localized corrosion. Naturally-occurring Al oxides as well as synthetic (O_2 plasma grown and deposited oxides) were studied by solid state electrical measurements. It was found that electron transport is controlled by thermal emission of carriers from deep traps within the oxide with the current being proportional to the trap or defect density. This defect density depends on the nature and type of the oxide: the deposited oxide exhibits the lowest defect density and the native oxide the highest, see Fig. 1(a).

Because the oxide electrochemical properties, such as the open circuit potential, are dependent on the rate of electron transport across the oxide, the solid state and electrochemical properties are correlated. Figure 1(b) shows that the open circuit potential is highest for the deposited oxide and lowest for the native oxide. This behavior results from the enhancement of the anodic reaction for the more conductive native oxide and suppression of the anodic current for the deposited oxide.

One model for pitting corrosion in Al is based on dielectric breakdown of the Al oxide in solution. The potential in solution at which breakdown occurs can be determined from knowledge of the solid state measured breakdown field and the open circuit potential; however, the situation is complicated by the observation that the electrical properties of the oxide change as a function of electrochemical polarization (see Fig. 2). The defect density within Al oxide increases upon exposure to an aqueous electrolyte, unless an anodic potential is applied to the Al. This behavior has been correlated with the incorporation of hydrogen within the oxide layer. Hydrogen is considered to be an electronic defect within Al oxide, and it is expected that some of this hydrogen is charged and mobile and can thus drift with an applied anodic field, leading to a reduction in oxide defect density.

With knowledge of how the oxide electrical properties change with applied potential in solution, it is now possible to predict the potential at which dielectric breakdown occurs in solution. These experiments are currently in progress.

Significance—The novel combination of solid state electrical measurements with electrochemical measurements is now leading to the ability to predict the potential at which dielectric breakdown of Al oxide occurs in solution. This information is critical for developing predictive modeling capability for the localized corrosion of passive metals, such as Al, and should lead to better mechanistic understanding of the corrosion process in general.

Sponsors for various phases of this work include: BES Materials Sciences and DP Research Foundations
Contact: John P. Sullivan, Nanostructure and Semiconductor Physics Dept., 1112
Phone: (505) 845-9496, Fax: (505) 844-4045, E-mail: jpsulli@sandia.gov

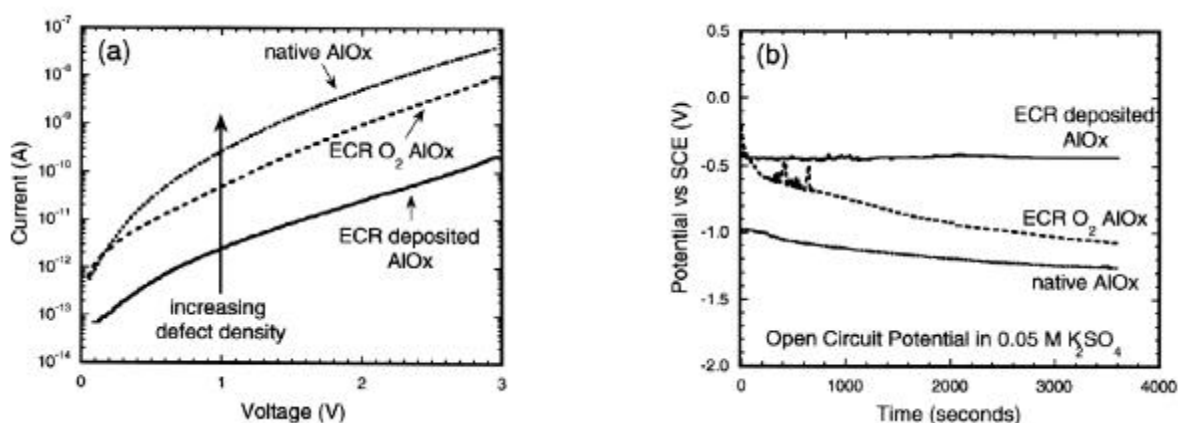


Figure 1. (a) Measured current as a function of voltage for three types of Al oxide layers on Al (a native oxide formed by exposure of freshly evaporated Al to O₂(g), an electron cyclotron resonance (ECR) O₂ plasma grown oxide, and an ECR deposited oxide). The magnitude of the current is directly proportional to oxide defect density. (b) The open circuit potentials measured for these oxides when immersed in 0.05 M K₂SO₄ solution. Higher open circuit potentials result when the oxide is more resistant to electron transport (less conductive).

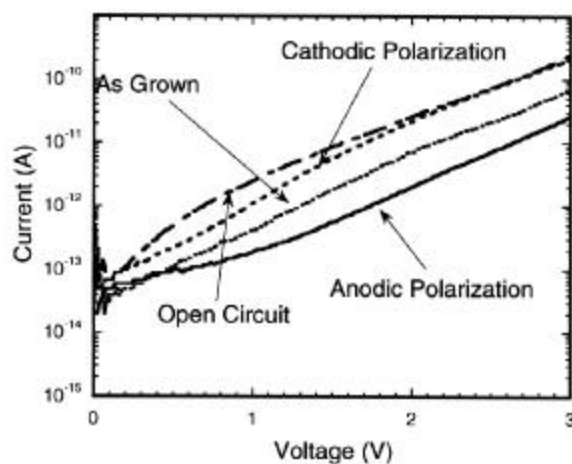


Figure 2. Measured current as a function of voltage for a deposited Al oxide layer after the oxide has been exposed to three different types of electrochemical treatments: application of a 10 nA cathodic current, open circuit conditions, and application of 10 nA anodic current (as grown properties are also shown). The current (defect density) is lowest following anodic polarization. This behavior has been associated with hydrogen in the oxide.

Multi-Phase Reactive Chemical Flow Modeling for Corrosion

H. K. Moffat, K. S. Chen, R. S. Larson, and G. H. Evans

Motivation—Atmospheric corrosion, observed in many stockpile components is a leading degradation mode. It typically occurs due to unknown or unexpected changes in the environment. As part of a larger effort to develop a comprehensive science-to-engineering-to-simulation-tool-set for performing the corrosion-related stockpile certification of electrical sub-systems, we are developing a continuum code to model corrosion processes. Copper sulfidation from H_2S provides the initial focus application.

Accomplishment—We have laid out a plan to develop new code capabilities based on a merger between Goma, an engineering sciences code, and Chemkin, a gas phase transport and kinetics package. The near term goal is to develop a multiphase, solid-state diffusion-reaction model. In later years, subgrid phases will be tackled. Currently, we have linked the two codes up (see example in Fig. 1) and are ramping up the incorporation of Chemkin material property evaluations within Goma.

Upgrades for Chemkin to perform as a liquid and solid materials property package have been planned. Several key concepts needed for solid-phase material property modeling were not needed nor included in the original Chemkin formation. An outline for the incorporation of new features such as volume fractions for multiple subgrid phases that aren't physically co-located, subgrid morphology modeling, the idea of surface and volumetric domains which delineate what species are active in a certain region, and non-ideal surface and volumetric thermochemistry has been completed. Work on an object-oriented implementation of these concepts is ongoing. We have also leveraged

work carried out under a thermal battery modeling LDRD to incorporate liquid electrochemical phase material properties modeling into the revamped Chemkin libraries as well as including Butler-Volmer reactions at liquid-solid interfaces.

Goma's capabilities for following moving phase boundaries have been demonstrated on several model corrosion problems (see Fig. 2). This year, moving phase boundaries with a Chemkin-derived mechanism and level set methods will be implemented.

We have demonstrated that gas-phase mass transport resistance is rate limiting for at least the early stages of copper sulfidation from a H_2S source for copper coupons with native oxides. Humidity levels are not important for this stage of growth, but do become important for later stages. A lower bound of 10^{-4} for the H_2S reactive sticking coefficient has been estimated. The gas-phase mass transport effect hadn't been recognized in previously published results, and has helped to reconcile seemingly contradictory experimental corrosion rate data.

Significance—Potentially great advantages lie in applying numerical modeling to understand corrosion and other allied solid-phase processes. Developing a continuum code has great synergies with Sandia's atomic scale code capabilities. It provides a vehicle for handing off material properties so that their significance may be put into context. We anticipate that the completed Goma-Chemkin code will feed into "downstream codes" that perform electrical analysis of complete systems and that carry out uncertainty analysis to access the significance of corrosion degradation modes.

Sponsors for various phases of this work include: ASCI, DP/ES-RF, BES Materials Sciences, and LDRD

Contact: Harry K. Moffat, Chemical Processing Science Dept., 1126

Phone: (505) 844-6912, Fax: (505) 844-3211, E-mail: hkmoffa@sandia.gov

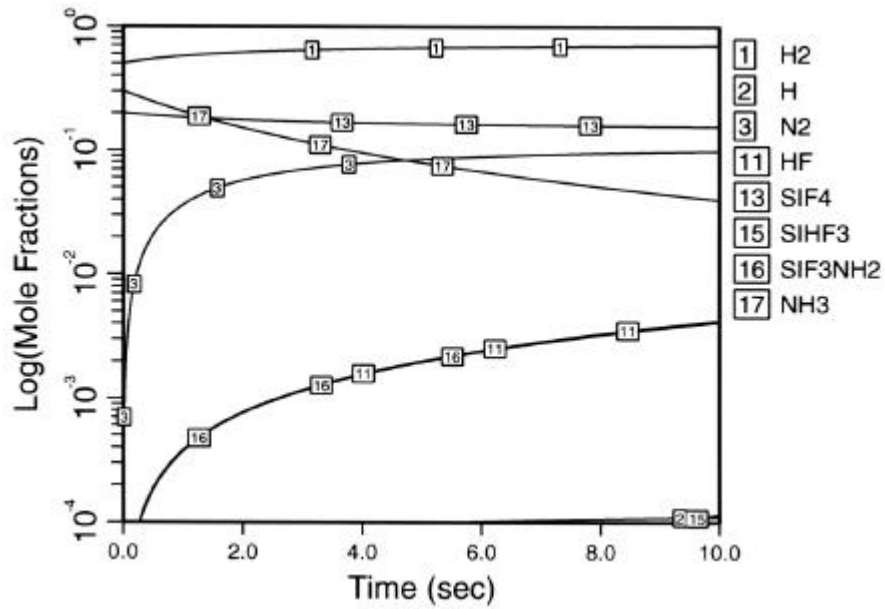


Figure 1. Demonstration of Goma-Chemkin coupling using a SiF_4 NH_3 pyrolysis problem. Mole fractions are calculated in Goma using source terms evaluated from Chemkin).

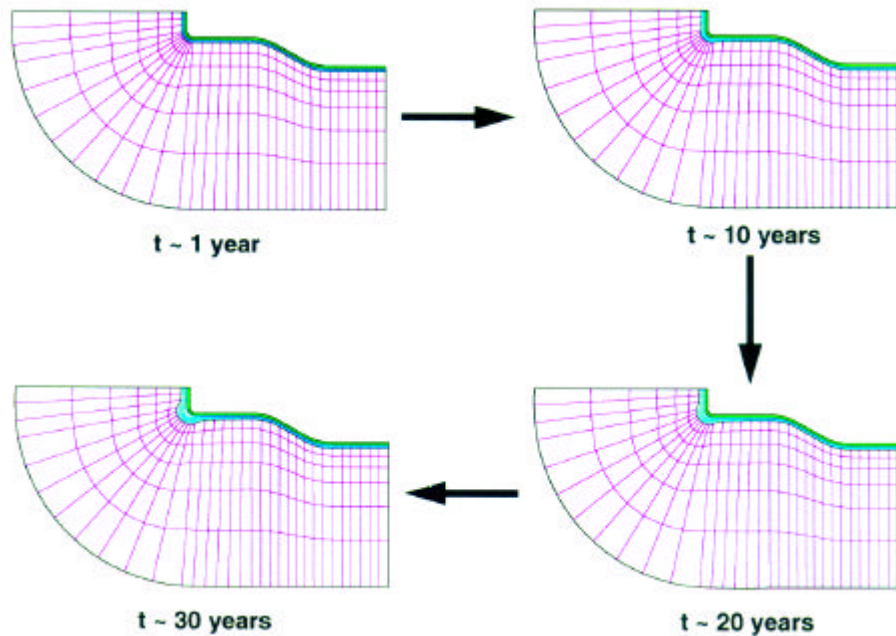


Figure 2. Goma's moving interface capability demonstrated on model H_2S copper sulfidation problem. Regions represent gas, Cu_{2-x}S , and Cu layers from bottom to top. Over time, Cu_{2-x}S layer expands. Regions near corners grow faster due to higher mass transport rates.

Non Proliferation



TRIBICC Measurements of Charge Transport in Gamma-Ray Surveillance Monitors

*G. Vizkelethy, D. S. Walsh, B. L. Doyle**

Motivation—Cadmium Zinc Telluride (CZT) is an emerging material for room temperature radiation detectors. These detectors can replace the currently used γ -ray detectors that either require bulky cryogenic systems (Ge detectors) or have inferior energy resolution (scintillators). An important field for these detectors is γ -ray surveillance where small portable detectors are needed with good energy resolution. Although the quality of the commercially available CZT crystals is continuously improving, there are still problems concerning the yield of the growth process and the quality of the crystals. In order to improve the quality and reduce the manufacturing cost it is important to understand how the crystalline quality and impurities affect the charge transport in the detectors.

Accomplishment—Time Resolved Ion Beam Induced Charge Collection (TRIBICC) provides information about the electronic transport properties of CZT that allows the microscopic scale study of the charge collection process. Several CZT detectors were bombarded with high-energy alpha particles and the preamplifier waveform was recorded. The ion beam was scanned along the axis of the detectors with about 1 mm spatial resolution. By analyzing the waveforms at different distances from the detector's cathode, the drift lengths of both the electrons and holes were calculated. Furthermore, since the holes are moving much slower than the electrons we were able to calculate the drift velocity profile of the holes. Figures 1a-c show typical preamplifier waveforms close to the cathode (a), around the center of the detector (b), and close to the anode (c). Close to the cathode only the electron transport contributes to the signal. In the ideal case, the

signal would increase linearly, but the finite lifetime rounds the top of the signal. This signal also indicates lower electric field at the anode. From the waveform at the center of the detector we can clearly distinguish the electron and hole contributions to the signal, and this lets us calculate the average drift velocities of the electrons and holes. The signal close to the anode is due to the hole transport only. The very long rise time combined with the relatively large signal indicates that trapping and detrapping of the holes take place in the detector. Figure 2 shows the measured charge collection efficiency as the function of the distance from the cathode. It is obvious from the figure that this detector does not have very good hole collection; the charge collection efficiency decreases constantly toward the anode. Electron and hole drift lengths ($\lambda = \mu E \tau$, μ - mobility, τ - lifetime, E - electric field) were fitted to the experimental data using the Hecht equation. The discrepancy between the calculated and measured curves shows that the constant drift length assumption is not entirely true, the electron and hole drift lengths vary along the detector's axis. This can be due to either inhomogeneous mobility or lifetime, or deviation from the assumed constant electric field.

Significance—The study of the electronic transport properties of CZT is necessary to solve the problems currently present in good quality CZT crystal production. TRIBICC using a nuclear microprobe is ideal for these studies. Our preliminary results showed good hole collection properties of this particular crystal, but it also showed that significant hole trapping and de-trapping takes place that contributes to the unwanted hole tailing effect.

*In collaboration with Ralph B. James of SNL, Organization 8330

Sponsors for various phases of this work include: DP Research Foundations and LDRD

Contact: Gyorgy Vizkelethy, Radiation-Solid Interactions, 1111

Phone: (505) 284-3120, Fax: (505) 844-7775, E-mail: gvizkel@sandia.gov

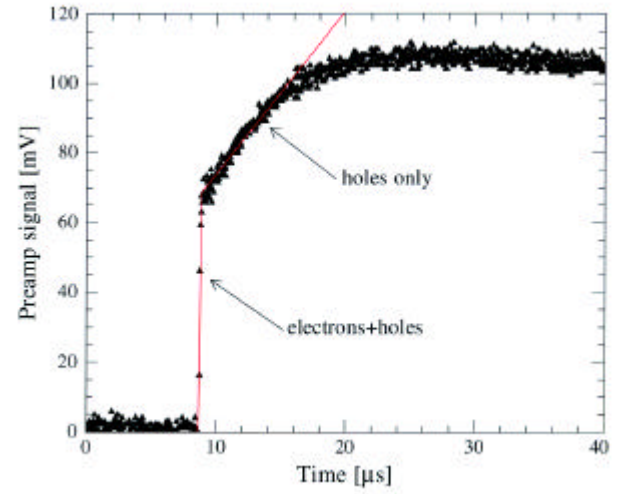
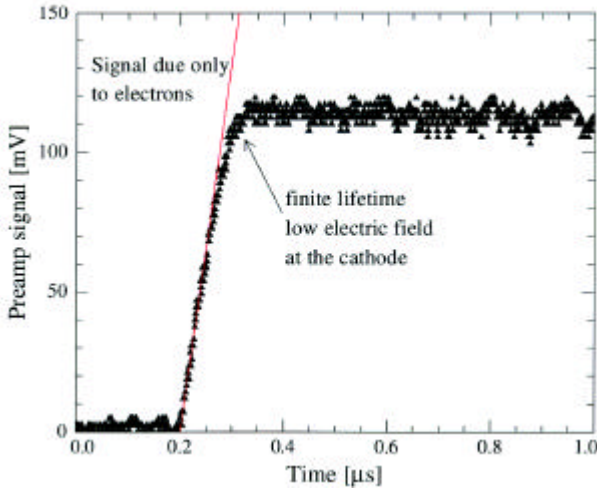


Figure 1a-b. Preamplifier waveforms close to the cathode (a), and at the center of the detector (b).

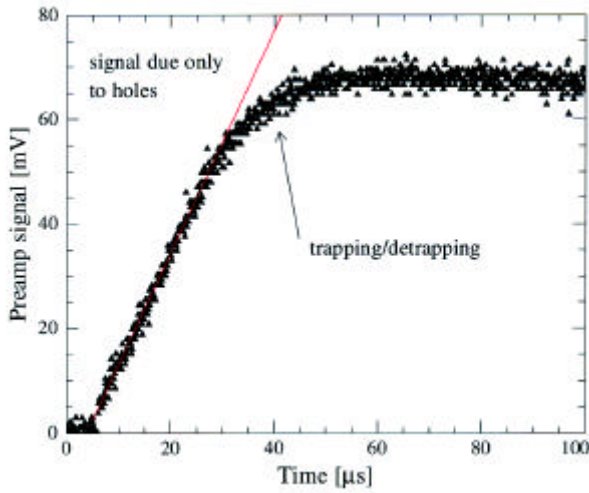


Figure 1c. Preamplifier signal close to the anode.

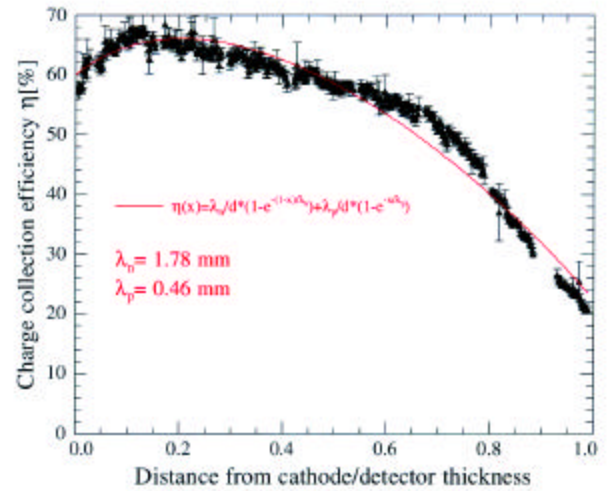


Figure 2. Charge collection efficiency along the axis of the detector. The experimental curve was fitted using the Hecht equation with constant electron and hole drift lengths.

GaN-based UV Light Emitting Devices

M. H. Crawford, J. Han, M. A. Banas, and J. J. Figiel

Motivation—Compact, efficient Light Emitting Diodes (LEDs) and Laser Diodes (LDs) in the ultraviolet (UV) region of the spectrum are not yet commercially available, but are of great interest for a number of applications. Two particular applications that are well-matched to Sandia's missions include Chem-Bio fluorescence based sensors that could use UV LEDs and LDs as fluorescence excitation sources, as well as robust, high efficiency white light sources where the UV light emitters would excite phosphors. These applications require the development of UV light emitters over the 300-400 nm region with powers from 10's of microwatts to several milliwatts.

Accomplishment—Through combined efforts in MOVPE growth, device design and device process development, we have developed UV LEDs in the 355-380 nm region. Our short wavelength structures are based on active regions that include thin GaN multi-quantum wells (MQWs) with AlGaIn barriers (Al composition $x=0.20$). These structures have emission wavelengths in the 350-360 nm region. There are several challenges in fabricating LEDs from these materials including the difficulty in achieving high optical efficiency from the GaN quantum wells, as well as the incorporation of AlGaIn layers without generating large scale cracking in the structure. In 1998, Sandia was the first group to report GaN MQW LEDs, which emitted 12 microwatts at 354 nm. Our most recent structures emit at 358 nm and approach 100 microwatt powers at 50 mA, 3.75 V input conditions. The light output and current-voltage data for one of these devices is shown in Fig. 1. These improvements have been realized through advances in the materials

quality as well as the development of NiO semi-transparent p-electrodes.

A new emphasis in the past year has been the development of LEDs with emission in the 370-380 nm region. These wavelengths are expected to match well with phosphor absorption bands and thus be well suited for white light LEDs. The structures involve InGaIn quantum well layers with AlGaInN quaternary barriers. Very low concentrations of In (e.g. 4%) in the quantum wells are needed to reach 380 nm. Photoluminescence spectroscopy was carried out to evaluate the optical efficiency of InGaIn epilayers in the low In composition regime. As seen in Fig. 2, the addition of only a few percent of In dramatically increased the photoluminescence efficiency of the materials. The integrated PL intensity of a sample with ~ 7% In was 25X higher than a GaN epilayer (no In) grown under similar conditions. Carrier localization at In composition fluctuations is one theory for the increased efficiency. We have recently demonstrated p-n junction LEDs with the InGaIn/AlGaInN MQW active regions. The light output power from these first generation LEDs is already similar to that of the 360 nm GaN MQW LEDs and further improvements are anticipated in next generation structures.

Significance—The ability to replace existing UV lamp systems with robust, compact UV LED or LD light sources would greatly expand our micro-system and sensor capabilities and could impact next-generation lighting systems. Our 360 nm LEDs have already been applied to one of our bio-sensor systems and progress has been made in the development of 380 nm LEDs for lighting applications.

Sponsors for various phases of this work include: LDRD

Contact: Mary H. Crawford, Semiconductor Material and Device Sciences Dept., 1113

Phone: (505) 844-7309, Fax: (505) 844-3211, E-mail: mhcrawf@sandia.gov

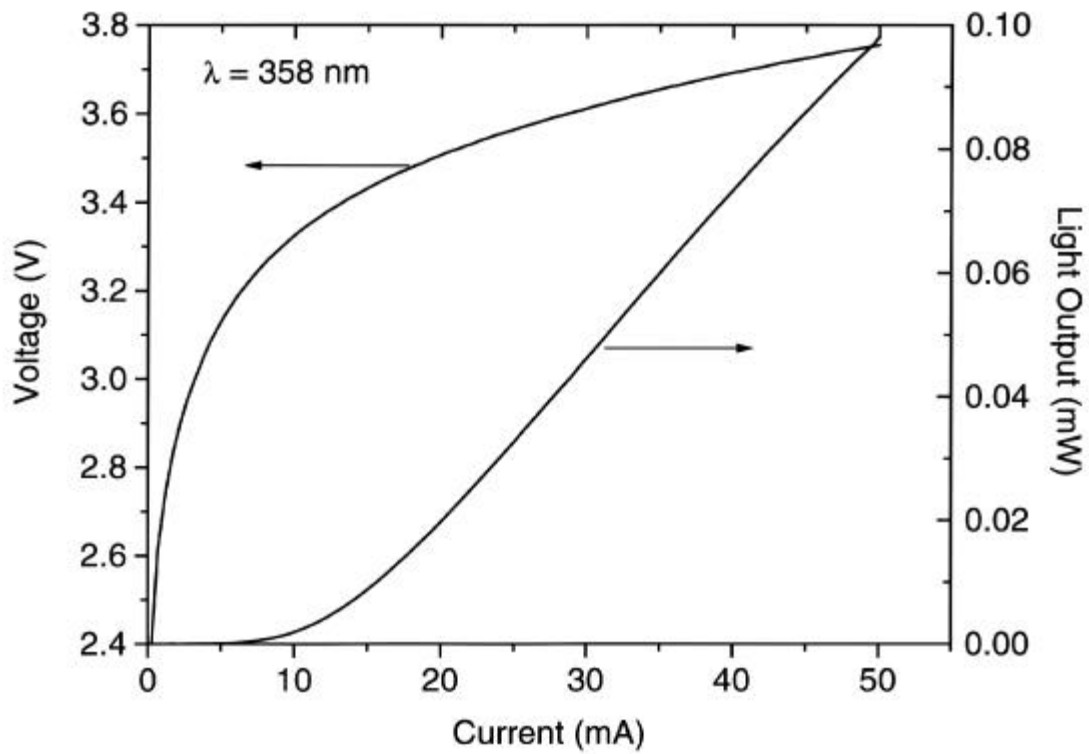


Figure 1. Light output-current and current-voltage data for a 250 micron GaN/AlGaIn MQW LED emitting at 358 nm (Ne0325c).

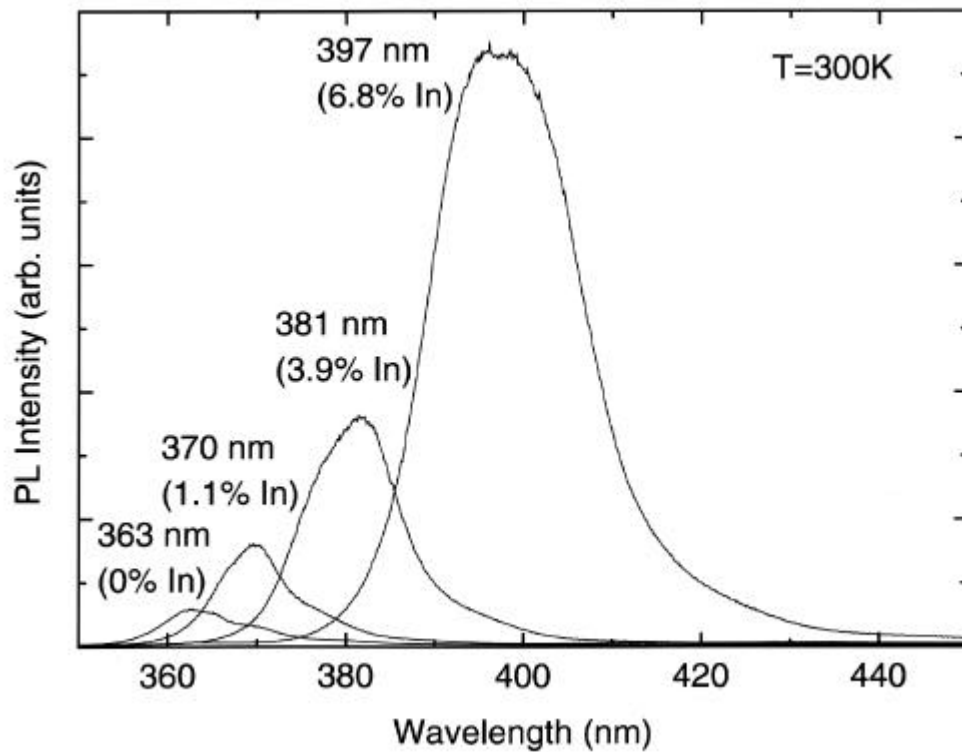


Figure 2. Room temperature photoluminescence of InGaIn epilayers with In composition varying from 0-6.8%.

UV Fluorescence Lidar Field Test Measurements

P. J. Hargis, Jr., R. L. Schmitt, and M. S. Johnson

Motivation—Recent measurements at Starfire Optical Range (SOR) on Kirtland Air Force Base have demonstrated the potential of ultraviolet (UV) fluorescence lidar for the detection of biological aerosols. Measurements made at SOR have, however, been restricted to the detection of aerosols contained in sealed cells. During the summer of 1999, we had the opportunity to verify our SOR lidar measurements under open-air aerosol detection conditions in field tests at Dugway Proving Grounds, Utah and White Sands Missile Range, New Mexico.

Accomplishment—Our UV fluorescence ground lidar trailer completed a successful field test at Dugway Proving Grounds. The trailer left Sandia NM on June 29 and returned on August 5. The lidar system was used to measure fluorescence spectra of biological aerosol clouds. Fluorescence spectra of three different biological aerosols were measured in the clouds for comparison to laboratory measurements previously made at Sandia. Three types of measurements were made at the field test: 1) UV elastic backscatter (used to locate aerosol clouds), 2) fluorescence backscatter (used to pinpoint the location of fluorescent aerosols), and 3) dispersed fluorescence spectra (used to detect biological aerosol clouds). A representative elastic backscatter measurement used to locate a biological aerosol cloud behind a dust cloud is shown in Figure 1. The Sandia lidar trailer participated in the Dugway field test at the invitation of the U.S. Army Soldier and Biological Chemical Command (SBCCOM) to help support U.S.

Army development of a biological detection system.

The Sandia UV fluorescence lidar trailer also completed a successful field test sponsored by the Defense Threat Reduction Agency (DTRA) at White Sands Missile Range. The purpose of the field test was to determine the fate of biological aerosols after a static detonation. Biological aerosols were placed inside a light steel structure (see Figure 2) in steel drums. The trailer arrived at White Sands Missile Range on September 14 to prepare for the September 23 test. Extensive calibration measurements were made between September 14 and September 23 to characterize fluorescence backgrounds under day and night detection conditions. Since the test took place during daylight hours, extensive characterization of the passive solar background was also required. Lidar measurements made prior to, during, and after the static detonation allowed us to characterize the fluorescence properties of biological aerosols after the static detonation.

Significance—Sandia is developing a unique airborne multispectral ultraviolet fluorescence lidar. Data acquired at the Dugway and White Sands field tests are being used to estimate the performance of the airborne lidar system for the detection of biological aerosols. The field test measurements have also been invaluable in fine-tuning the design of the airborne lidar system and in developing concepts for locating and detecting biological aerosol clouds.

Sponsors for various phases of this work include: NN-20 and DP Research Foundations

Contact: Philip J. Hargis, Laser, Optics and Remote Sensing Dept., 1128

Phone: (505) 844-2821, Fax: (505) 844-5459, E-mail: pjhargi@sandia.gov

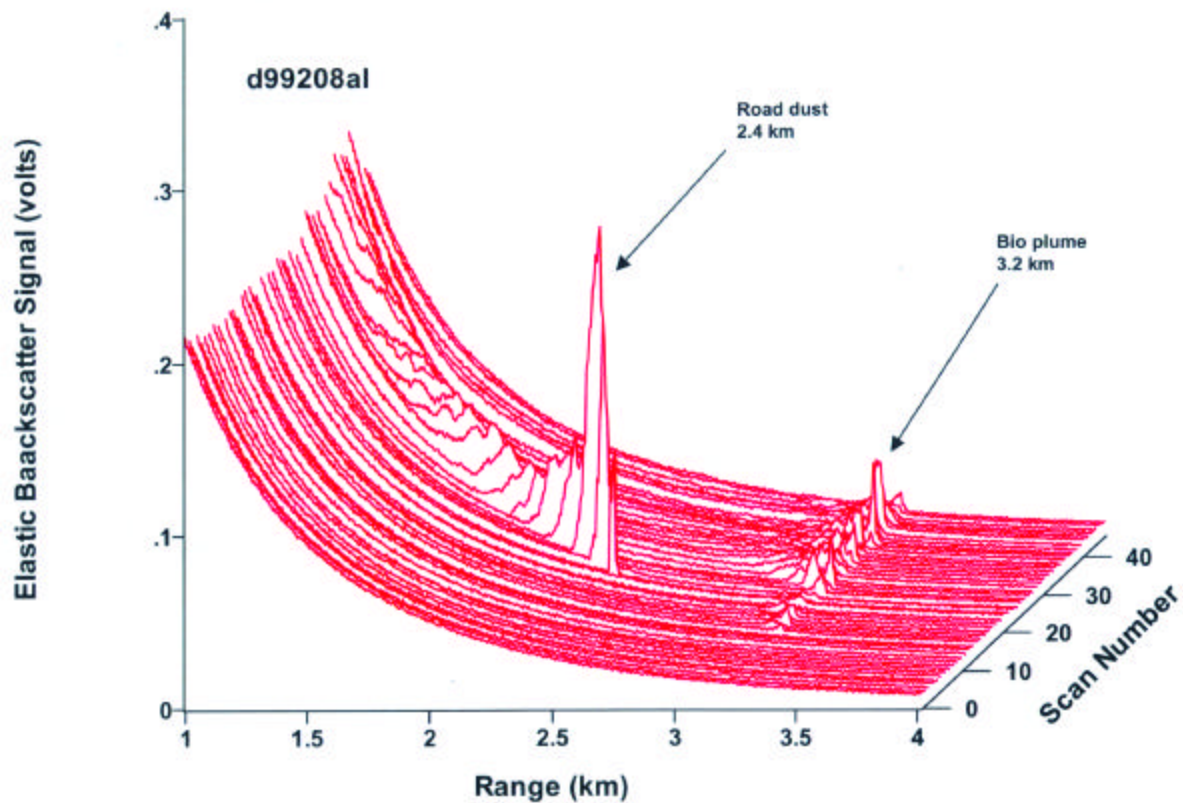


Figure 1. Elastic backscatter signals measured at Dugway Proving Grounds show the ability of UV light to penetrate a dust cloud and detect a biological aerosol plume. The measurements show the dust cloud moving toward the lidar trailer and the biological plume at a fixed standoff distance of 3.2 km.

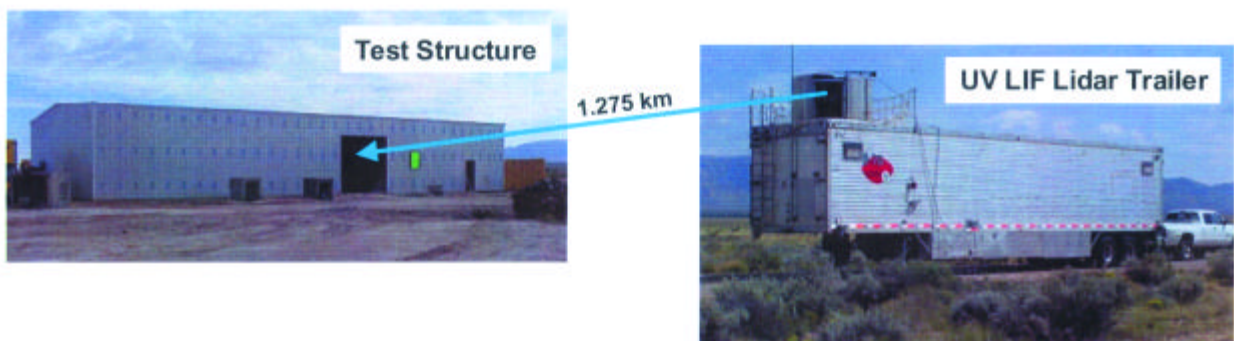


Figure 2. The Sandia UV laser-induced-fluorescence (LIF) lidar trailer deployed at White Sands Missile Range was positioned at a standoff distance of 1.275 km from a light steel structure containing biological simulants. After the static detonation, the lidar system was used to characterize the fluorescence properties of biological aerosols.

Nanoscience Research



Total Destruction of a Toxic Chlorinated Organic Using Visible Light and Nanoparticles of MoS₂

J. P. Wilcoxon

Motivation—Solar photodetoxification is a process wherein sunlight is captured by semiconductor particles in suspension to create electrons and holes that then diffuse to the particulate surface to effect the oxidation and reduction of toxic pollutants (see Fig. 1). Using solar energy to oxidize organic chemicals to carbon dioxide and dilute mineral acids is very energy efficient compared to other methods such as incineration. Finding an efficient catalyst has thus been a focus of research, which has had only limited success, the fundamental problem being that semiconductors that efficiently absorb in the visible portion of the solar spectrum also photocorrode. Our work is focussed on development of chemically stable nanosize semiconductor materials as photocatalysts.

Accomplishment—We have demonstrated total oxidation of several toxic organic chemicals, including chlorinated organics and phenols, using nanosize MoS₂ and visible light. One of the most important of these chemicals is pentachlorophenol (or PCP), a widely used chemical ubiquitous in the environment. Although this chemical can also be oxidized using the best commercially available photocatalytic powder, TiO₂, this wide-bandgap semiconductor is not viable because it requires excitation by UV light, specifically wavelengths $\lambda < 390$ nm, the absorption edge of TiO₂. We demonstrated complete oxidation of PCP using only light with $700\text{ nm} > \lambda > 400$ nm and MoS₂. We studied the chemistry of this process by high pressure liquid chromatography which separates

each of the chemicals in the solution from the MoS₂ photocatalyst. The results of this experiment are shown in Fig. 2 where the relative rate of oxidation of PCP vs. illumination time is shown for several photocatalysts. Using chromatography we have been able to follow the course of the photochemistry and demonstrate that the nanosize MoS₂ used is unaltered by the reaction - it functions as a true photostable photocatalyst. We have also demonstrated that by controlling the size of the MoS₂ nanocrystals we can tune the optical absorption to the desired visible region of the spectrum thereby optimizing MoS₂'s oxidation/reduction potentials as well as the photooxidation kinetics for this photodetoxification process (compare the 4.5 nm and 3.0 nm MoS₂ results in the figure. The 3.0 nm nanocrystals have a higher oxidation potential and much faster kinetics.

Significance—This appears to be the first demonstration of photoredox reactions to completely oxidize and remove toxic chlorinated organics from water using nanosize semiconductors and only visible (i.e. solar-like) illumination. Our MoS₂ nanoclusters are synthesized by an inverse-micellar process. Being a solution technique, this process is low cost and amenable to scale up to any desired size. Additionally, because we have exceptional control over nanocrystal size, we can tune the absorption to the solar spectrum capitalizing on a very plentiful light source - sunlight - to effect the detoxification.

Sponsors for various phases of this work include: BES Materials Sciences

Contact: J. P. Wilcoxon, Nanostructures and Advanced Materials Chemistry Dept., 1152

Phone: (505) 844-3939, Fax: (505) 844-4045, E-mail: jpwilco@sandia.gov

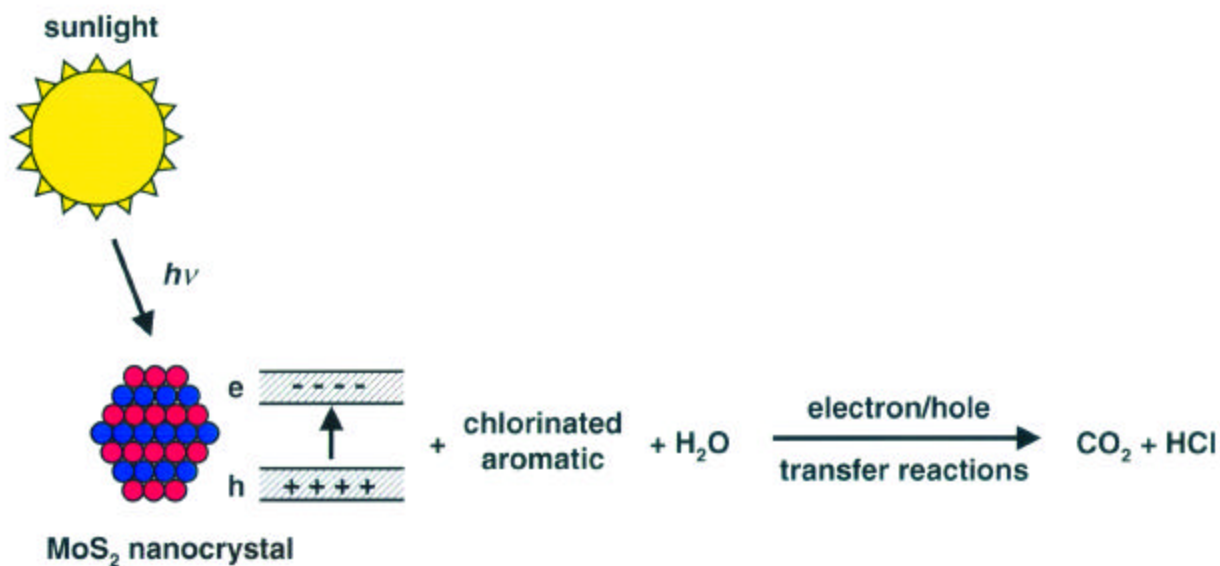


Figure 1 Using a visible band-gap semiconductor to create hole-electron pairs to oxidize organic toxins.

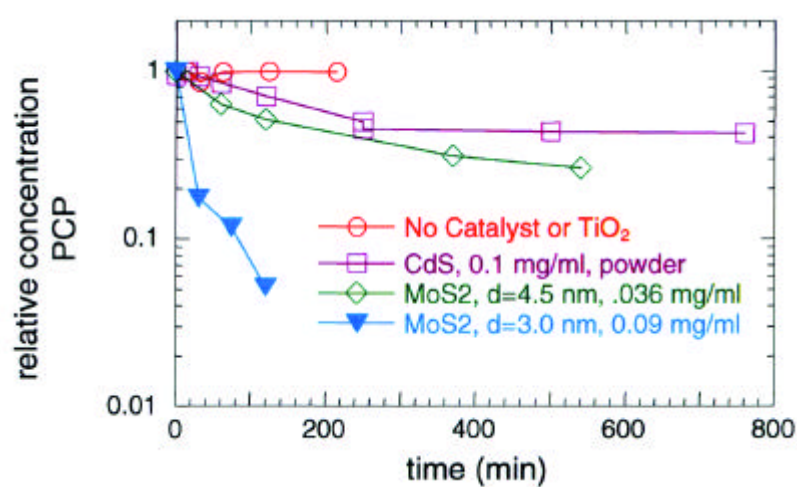


Figure 2. Plot of relative PCP concentration vs. illumination time using visible light, $400 < \lambda < 700$ nm, for two sizes of nanosize MoS₂ compared to a bulk semiconductor, CdS with similar absorbance characteristics, and to TiO₂

The Dynamics of Giant Spins on Magnetic Nanoclusters

E. L. Ventruini, J. P. Wilcoxon, and P. N. Provencio

Motivation—We are exploring the physics of magnetic nanoclusters between 2 and 10 nm in diameter as a function of cluster size. In this size range the clusters have a single magnetic domain and the strongly coupled magnetic spins on each atom combine to produce a particle with a single "giant" spin. Our goals are to identify novel quantum effects at the nm scale and to compare cluster properties with those of the bulk metal. Applications of magnetic particles in important areas such as xerography, ferrofluidics, magnetic data storage and magnetic resonance imaging require detailed knowledge and control of their properties.

Accomplishment—Size-selected nanoclusters of metallic Fe were grown inside inverse micelles formed by surfactant aggregates in an oil-continuous, oxygen- and water-free fluid system. This synthesis prevents formation of a surface oxide on the clusters and facilitates sample transfer to a SQUID magnetometer under inert argon gas for magnetic measurements. High-resolution transmission electron microscopy and high-pressure liquid chromatography studies were used to determine cluster diameter and to confirm the narrow distribution in sizes.

Figure 1 shows the magnetic moment at 100 K for a sample of Fe nanoclusters versus applied magnetic field. The solid line is a least-squares fit to the data using the Langevin function for classical magnetic spins with two adjustable parameters: a "giant" spin of 3500 Bohr magnetons (μ_B) per cluster and 1.6×10^{14} clusters in this sample. Since the sample contains 0.1 mg of Fe, the two fitting parameters yield an average cluster diameter of 5.4 nm (6900 atoms) and a spin of $0.5 \mu_B$ per Fe atom. The latter value is 25% of that for bulk Fe (which has $2.2 \mu_B$ per

atom); hence, the presence of "surface" atoms with reduced exchange coupling plus quantum (finite-size) effects on the "bulk" atoms lead to a substantial reduction in the spin per cluster atom.

Figure 2 shows the static magnetic susceptibility in a constant field of 1 mT versus increasing and decreasing temperature. The strong temperature hysteresis is a classic feature of magnetic nanoclusters where spin reorientation is inhibited by the intrinsic crystalline magnetic anisotropy; this generates an energy barrier to reorientation of the "giant" spins. The thermally activated reorientation occurs on a time scale that decreases exponentially with increasing temperature. When the reorientation time is comparable to the experimental time scale (minutes), the susceptibility reaches a maximum for increasing temperature at the "blocking" temperature (near 25 K for this sample).

Figure 3 compares the static susceptibility data for increasing temperature with three AC measurements at 1, 10 and 100 Hz. These nanoclusters exhibit very strong low-frequency dispersion suggesting a low "attempt" frequency for spin reorientation. The broad peaks and large dispersion confirm the very slow dynamics for the "giant" spins on these Fe nanoclusters.

Significance—This research establishes a knowledge base for "bare" nanocluster behavior. Future work will explore changes in individual cluster properties with different, weakly bound surfactant molecules and strongly bound coatings such as other metals or thin oxide layers. A separate project incorporates these nanoclusters into structured arrays where dipolar coupling of their "giant" spins has a significant effect on the magnetic behavior of the system.

Sponsors for various phases of this work include: BES Materials Sciences

Contact: Eugene L. Venturini, Nanostructures and Advanced Materials Dept., 1152

Phone: (505) 844-7055, Fax: (505) 844-4045, E-mail: elventu@sandia.gov

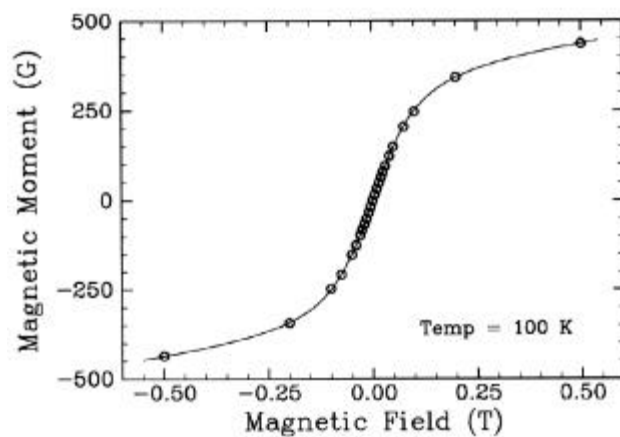


Figure 1. Magnetic moment of Fe nanoclusters at 100 K versus applied field.

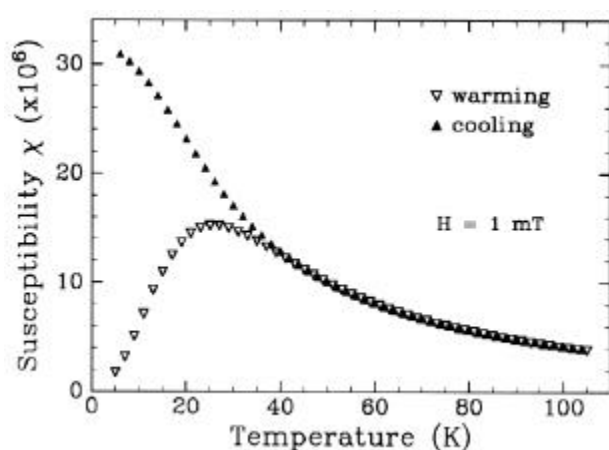


Figure 2. Static magnetic susceptibility of Fe nanoclusters in 1 mT field versus temperature. The peak in the data for increasing temperatures occurs at the "blocking" temperature for spin reorientation.

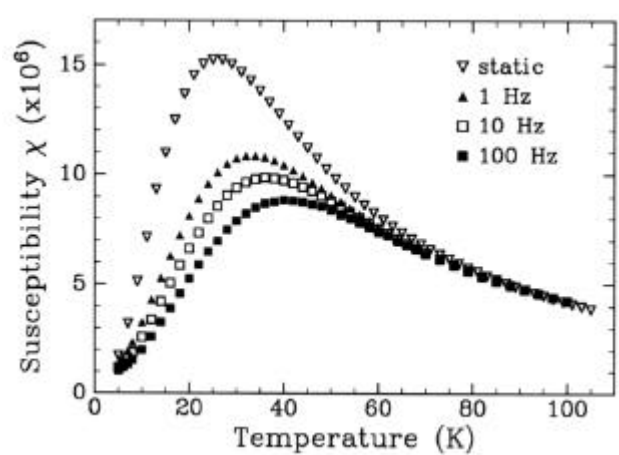


Figure 3. Static and AC magnetic susceptibilities (at 1, 10 and 100 Hz) of Fe nanoclusters versus temperature. The strong low-frequency dispersion reflects the slow dynamics of spin reorientation.

Enhanced Composition Modulation in InAs/AlAs Superlattices

*D. M. Follstaedt, J. L. Reno, S. R. Lee and E. D. Jones**

Motivation—Quantum confinement effects, in which carriers in a semiconductor are restricted to nanometer-scale microstructures, allow the manipulation of electronic properties for advanced devices. Increasing attention is being given to growth of materials that self-organize into wires or sheets for confinement in one or two dimensions. We have shown that short-period superlattices of InAs/AlAs deposited with lateral uniformity form laterally alternating regions that are strongly enriched in In or Al. However, this composition modulation has a complex organization with two modulation directions, making it difficult for investigation of electronic properties and potentially limiting its uses. We therefore investigated whether the modulations can be manipulated by growth on miscut substrates.

Accomplishment—We used transmission electron microscopy (TEM) to examine growth of InAs/AlAs superlattices (~2 monolayers of each) at 540°C by molecular-beam epitaxy on (001) InP substrates miscut by 2 degrees toward various directions. This produces a slight net tension in the superlattice since its average lattice constant is slightly smaller than that of the substrate. Growth on exactly oriented (001) surfaces produces two modulation directions approximately along the [310] and [130] directions. The compositionally enriched "wires" are less than 0.2 μm in length, with the two directions being irregularly interspersed between each other, as seen in Fig. 1.

For substrates miscut 2 degrees toward (101), the [310] modulations become predominant as seen in Fig. 2. Moreover, the wire lengths are now longer, up to 0.4 μm , and the contrast

observed in TEM indicates that the degree of compositional enrichment remains strong. Miscuts toward (10-1) produce the same microstructure. Miscuts toward the (111)A and (111)B surfaces retain two modulation directions; however, with miscut to (111)A the two directions are aligned slightly closer toward the [110] direction.

These observations agree with the simple interpretation that modulations along the direction of miscut are enhanced and their wire lengths extended, while modulations nearly perpendicular to this direction are suppressed. Understanding these effects of atomic surface steps produced by miscutting on microstructure may provide new insight into how compositions are locally enriched and organized into wires during growth, which is not well understood.

Significance—The ability to control modulation geometries will allow the electronic properties of these quantum-confinement structures to be investigated with greater detail and precision. A single modulation direction and extended wire lengths are expected to produce highly anisotropic carrier transport in the growth plane, and to determine a polarization direction for optical emission. This geometry allows magnetic fields to be aligned along the wires or perpendicular to them for examination of magneto-exciton energies. The one-dimensional modulation geometry is also favorable for potential applications of compositionally modulated semiconductors, which may include use as long wavelength detectors, absorbing layers in solar cells, and polarized emission from semiconductor lasers.

*Collaborators: A. Norman and A. Mascarenhas, National Renewable Energy Laboratory; J. Mirecki Millunchick, Univ. Michigan; and R. D. Twisten, Univ. Illinois

Sponsors for various phases of this work include: BES Materials Sciences

Contact: David M. Follstaedt, Nanostructure and Semiconductor Physics Dept., 1112

Phone: (505) 844-2102, Fax: (505) 844-7775, E-mail: dmfol@sandia.gov

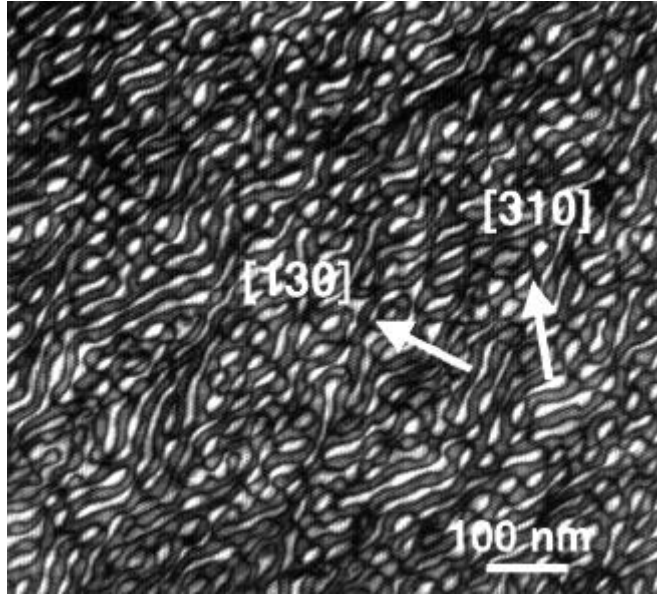


Figure 1. Plan-view image of $(\text{InAs})_2/(\text{AlAs})_2$ superlattice grown on (001) InP substrate, obtained with composition-sensitive (200) dark-field TEM; white areas are enriched in In. The composition modulation is a mixture of two directions near $[310]$ and $[130]$, and wire lengths extend up to $\sim 0.2 \mu\text{m}$. In some regions, the two modulations interfere to produce small, interspersed islands.

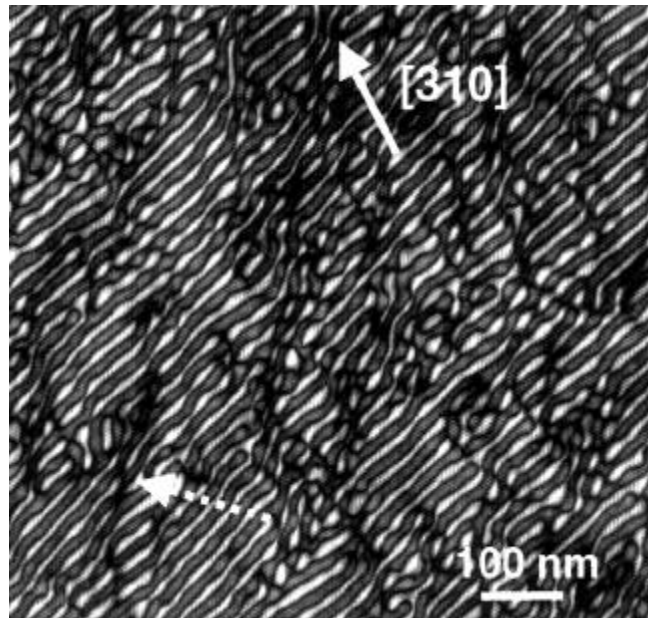


Figure 2. Image of $(\text{InAs})_2/(\text{AlAs})_2$ superlattice grown on (001) InP substrate miscut 2° toward (101). Here the $[310]$ modulation dominates, and wire lengths extend up to $0.4 \mu\text{m}$.

Simulation of H Behavior in p-GaN(Mg) at Elevated Temperatures

S. M. Myers and A. F. Wright

Motivation—Hydrogen is incorporated into GaN during growth and processing, and this gives rise to unwanted passivation and compensation of dopants, particularly in p-type material. The H can be removed by annealing, but this is accompanied by detrimental effects such as N loss. Consequently, such annealing should be tailored to accomplish the desired extent of dopant activation while minimizing unwanted effects. To this end, we are developing a mathematical model of H behavior in GaN at elevated temperatures. Hydrogen energies obtained from density-functional theory are used in a coupled set of diffusion and reaction equations to describe transport, uptake, release, and local equilibrium among the H states within the matrix. Validation is by comparison with experiment. The model is initially being applied to p-type GaN doped with Mg.

Accomplishment—Density functional theory indicates that H in GaN can assume positive, neutral, and negative charge states, form a bound neutral complex with the substitutional Mg acceptor, and exist as interstitial H_2 . Figure 1 shows the computed zero-temperature energies of these states, expressed relative to atomic H in vacuum, as a function of Fermi level. In p-type GaN(Mg), the principally occupied states are H^+ and the Mg-H complex; the elevated-temperature thermodynamics of these species are therefore treated more accurately by including the enthalpy and entropy of H vibration in the harmonic approximation using mode frequencies obtained from density functional theory. Activation energies for diffusion of H^+ , H^0 , and H^- are also taken from density functional theory.

The above theoretical results are used in a coupled set of diffusion and reaction equations describing the behavior of H at elevated temperatures. The solubility of H in equilibrium with H_2 gas is calculated without free parameters and found to be in good semiquantitative agreement with experiment, the disparity corresponding to a shift of only 0.18 eV in the energies of Fig. 1.

Comparison of the theoretical model with experimental results indicates that the surface of GaN is a barrier to the permeation of H. This effect is included in the model using surface properties deduced from a combination of theoretical and experimental information. The resulting formalism provides a comprehensive description of the occupancies of the solution states, transport within the matrix, uptake from H_2 gas, thermal release, and the electron and hole concentrations that result. Figure 2 shows predictions for the technologically important electrical activation of p-GaN(Mg) by isothermal release of H. These results and similar ones for isochronal annealing are in good semiquantitative agreement with the limited experimental information available on H release and electrical activation.

Significance—By accounting for a variety of experimental observations the theoretical model reinforces current understanding of H states within GaN and provides strong evidence for a surface permeation barrier characterized by second-order release kinetics. With further refinement in the light of additional experiments, the model is expected to provide the quantitative description of H behavior needed for device processing.

Sponsors for various phases of this work include: BES Materials Sciences and DP Research Foundations

Contact: Sam M. Myers, Nanostructure and Semiconductor Physics Dept., 1112

Phone: (505) 844-6076, Fax: (505) 844-7775, E-mail: smmyers@sandia.gov

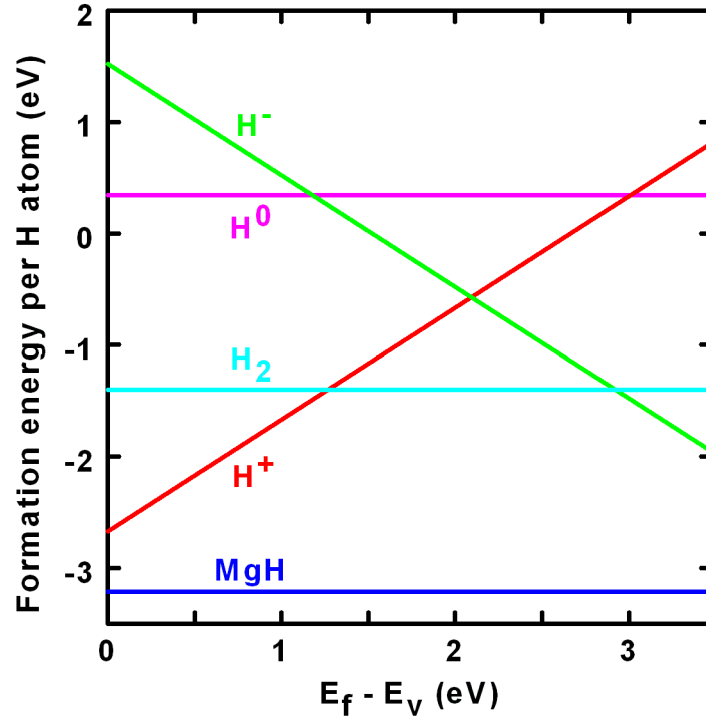


Figure 1. Formation energies of H in GaN at zero temperature expressed relative to the H atom in vacuum, as predicted by density functional theory.

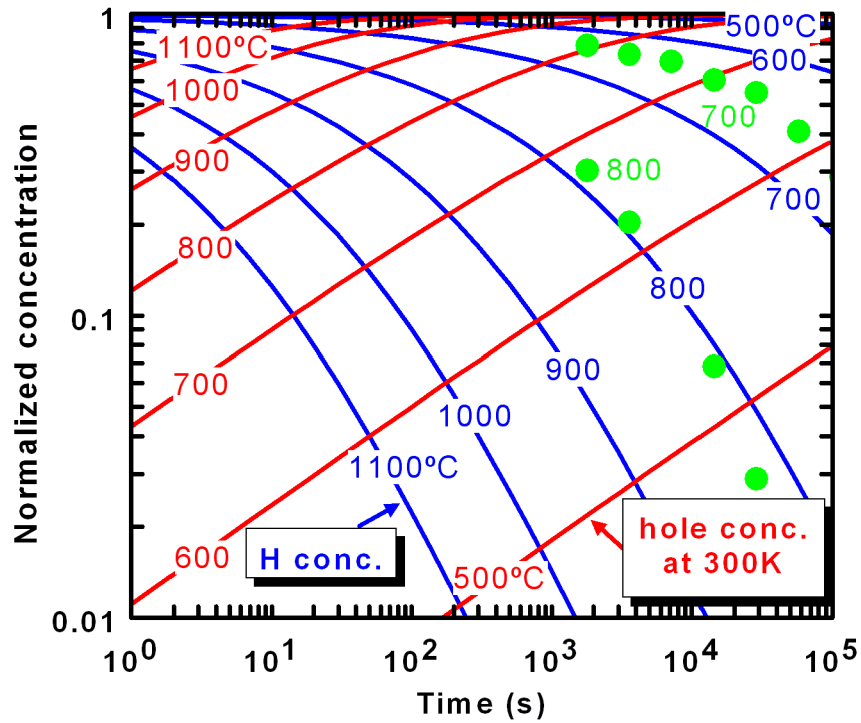


Figure 2. Predicted isothermal release of H from p-GaN(Mg) and accompanying increase of room temperature hole concentration.

Localized Corrosion Initiation at Nanoengineered Cu-rich Defects in Al Thin Films

N. Missert, J. C. Barbour, K.-A. Son, J. P. Sullivan, F. D. Wall, K. R. Zavadil, R. G. Copeland and M. A. Martinez

Motivation—The US spends nearly 5% of its GNP per year on failures due to corrosion. An understanding of the precise pit initiation mechanism at second phase particles in Al-Cu alloys would greatly facilitate the prevention and prediction of localized corrosion phenomena. Elucidation of the mechanism is complicated by the interaction of competing factors such as the galvanic couple action of the particle/matrix, chemistry of the particle/matrix interface, oxide defects in the vicinity of the particle, and local heterogeneous solution chemistry during dissolution.

Accomplishment—This work attempts to distinguish between competing mechanisms by nanoengineering Cu-rich heterogeneities in an Al thin film matrix and using them to study pit initiation at microscopic length scales. This approach allows unique control of the anode/cathode area ratio, the type of oxide grown at the surface of the particle and matrix, and the ability to study the interface chemistry. Ultra-high purity, electron beam evaporated Al thin films are used as the matrix. Arrays of Cu-rich heterogeneities within the Al thin film matrix are created using photolithography followed by Ar ion beam etching and Cu film deposition. Arrays with defect diameters ranging from 2 - 50 μm and spacings of 10 - 400 μm have been fabricated as shown in Fig. 1. X-ray photoelectron spectroscopy (XPS) scans of thin bilayers of Al/Cu indicate that these Cu-rich defects have interface binding energies characteristic of theta phase Al_2Cu , which is known to initiate pitting in Al-Cu alloys and interconnects. In order to study corrosion initiation, the arrays are immersed in a dilute NaCl

solution while monitoring the open circuit potential as a function of time. Transient events consisting of a linear decrease in the potential followed by an exponential anodic decay are observed for all arrays investigated to date. For short time exposures, the frequency of these events decreases as the spacing between defects increases. Scanning electron microscopy (SEM) combined with energy dispersive spectroscopy (EDS) after short time exposure indicates that the Cu-rich defects induce dissolution of the underlying Al in the form of a crevice as shown by the EDS linescan in Fig. 2. Initiation of Al dissolution occurs at the perimeter of the defect, and proceeds inward along the Cu/Al interface over micron length scales before dissolving the 0.2 μm Al film thickness. SEM images of the surrounding Al matrix in the vicinity of the defect indicate preferential partial dissolution of grains within a few microns of the defect perimeter. Similar experiments were performed on identical defect arrays where Al defects were substituted for Cu defects. In this case, corrosion initiation was not observed in the vicinity of the defect.

Significance—These results indicate that corrosion initiation at Cu-rich heterogeneities is driven by galvanic coupling and that a defective Al-oxide interface between the particle and matrix is insufficient to initiate pitting. The crevice geometry observed in the early stages of attack suggests that the nature of the interface between the heterogeneity and matrix, as well as the local chemistry, are critical in governing the initial stages of propagation and in determining whether pitting will be stable.

Sponsors for various phases of this work include: BES Materials Sciences

Contact: Nancy Missert, Nanostructure and Semiconductor Physics, Dept., 1112

Phone: (505) 844-2234, Fax: (505) 844-1197, E-mail: namisse@sandia.gov

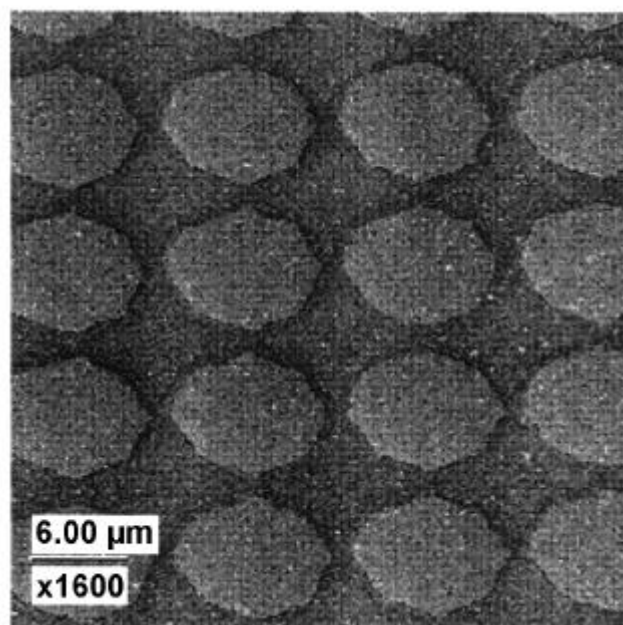


Figure 1. SEM image of Cu-rich defect array in Al thin film matrix. Defects are 8 μm in diameter.

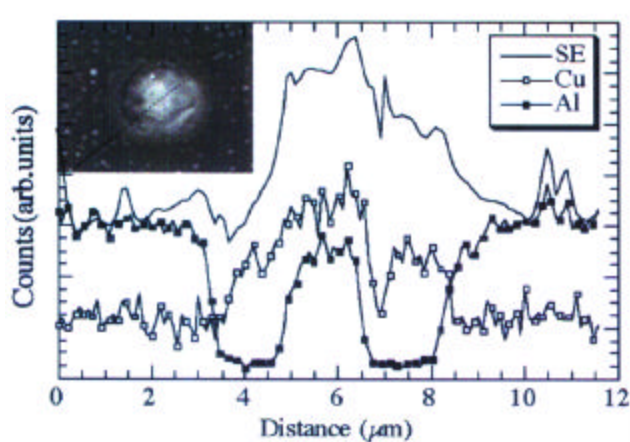


Figure 2. EDS linescan of Al and Cu across a single Cu-rich defect after 10 min. exposure to 0.05 M NaCl. SEM intensity is shown to indicate the position of the defect.

Fracture in III-Nitride Alloys Permits Dislocations to Relieve Tensile Stress

J. A. Floro, S. Hearne, J. Han, D. M. Follstaedt, S. R. Lee, and J. Figiel

Motivation—Aluminum gallium nitride (AlGa_N) is an alloy of GaN and AlN that offers significant potential for use in ultraviolet (UV) light emitting devices. Such devices are needed in a variety of critical sensing applications. AlGa_N is typically grown epitaxially upon GaN epilayers in a state of tensile stress due to the difference in lattice parameters. This can lead to fracture of the AlGa_N, which is deleterious to device operation. Unfortunately, a great deal of confusion permeates the III-nitride literature with regard to the energetics and kinetics of fracture processes.

Accomplishment—We performed real-time stress measurements during chemical vapor deposition of epitaxial AlGa_N layers on GaN in a rotating disk reactor. These novel experiments required synchronization of our Multi-beam Optical Stress Sensor (MOSS), a wafer-curvature monitor developed at Sandia, with a sample spinning 1200 times per minute. Our results clearly demonstrated that relaxation occurred during growth (rather than after), identified the critical thickness for onset of fracture, and determined the overall degree of strain relaxation. The latter revealed the surprising result that the observed crack densities accounted for a small fraction of the relaxation, directly implying the presence of a different stress-relieving defect (Fig. 1). Subsequent transmission electron microscopy exposed the presence of a dense array of misfit dislocations at the AlGa_N/GaN interface that accounted for the majority of the stress relaxation. The cracks do play an important role, however, in that they permit facile propagation of misfit dislocations

in a materials system for which such processes are otherwise highly constrained. The MOSS measurements also mapped out the critical thickness for fracture as a function of the alloy composition. We demonstrated that this data could be consistently described by a simple fracture energetics model (Fig. 2). In some films we observed metastable growth, i.e., the formation of films that are thermodynamically able to crack but are kinetically constrained from doing so. Finally, we showed that cracks can be dynamically overgrown and buried during film deposition. This process may be responsible for erroneous conclusions in previous literature reports that fracture occurs during cooldown after growth, which was inferred from cracks that appeared to propagate upward from the AlGa_N/GaN interface.

Significance—Our work immediately raises the question of whether it is really cracks that cause problems for devices, or whether it is, in fact, the dense misfit dislocation array, whose presence has not been recognized previously. This issue clearly has consequences for how devices are designed. Furthermore, our measurements of the critical thickness boundary and metastability regions will help guide the design of process flows in order to obtain low defect density structures. The ability to overgrow cracks might lead to new growth schemes to reduce crack densities within the active layers of devices. Last, but not least, we have demonstrated that curvature-based stress measurement serves as a valuable diagnostic for real-time process control and characterization during chemical vapor deposition.

Sponsors for various phases of this work include: BES Materials Sciences and LDRD

Contact: Jerrold A. Floro, Nanostructure and Semiconductor Physics Dept., 1112

Phone: (505) 844-4708, Fax: (505) 844-1987, E-mail: jaflo@sandia.gov

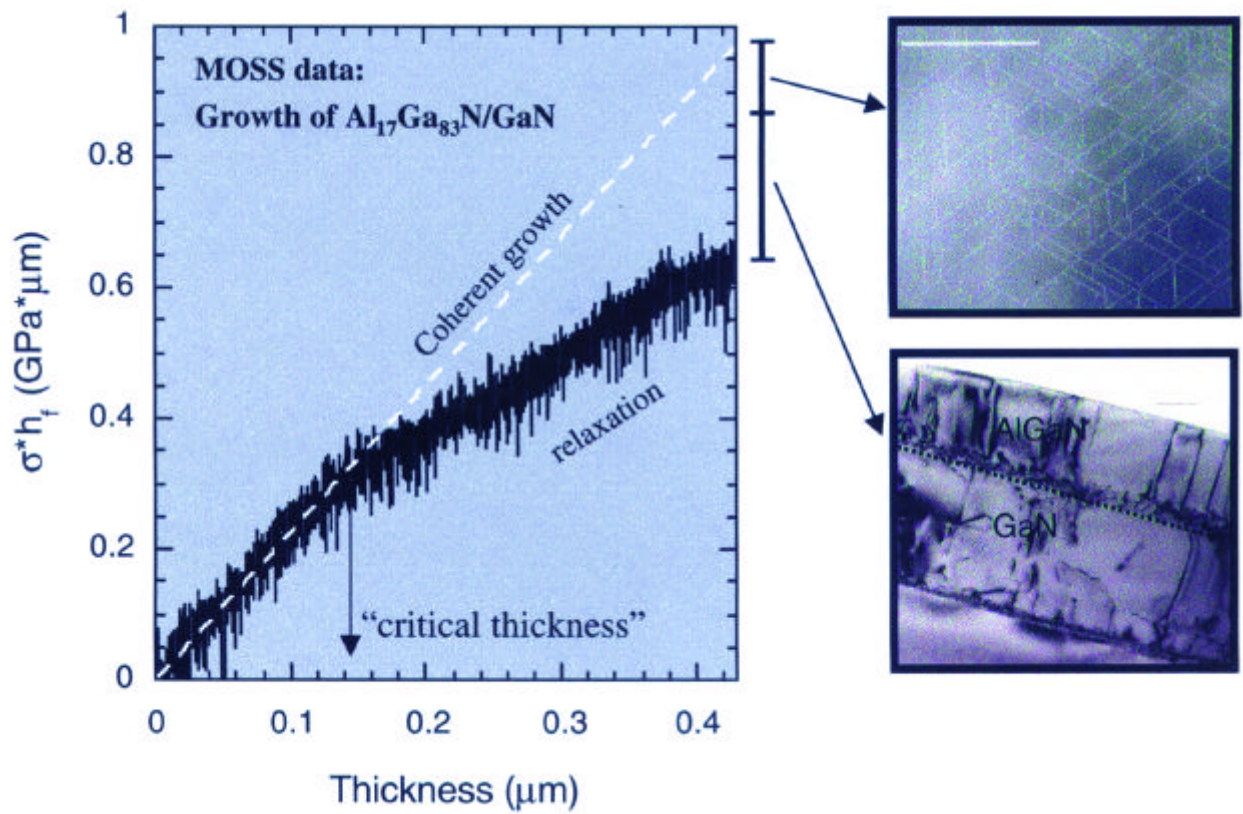


Figure 1. Real-time data on stress evolution during AlGaIn growth on GaN. The bars represent the amount of stress relaxed by cracks (upper right) and misfit dislocations (lower right).

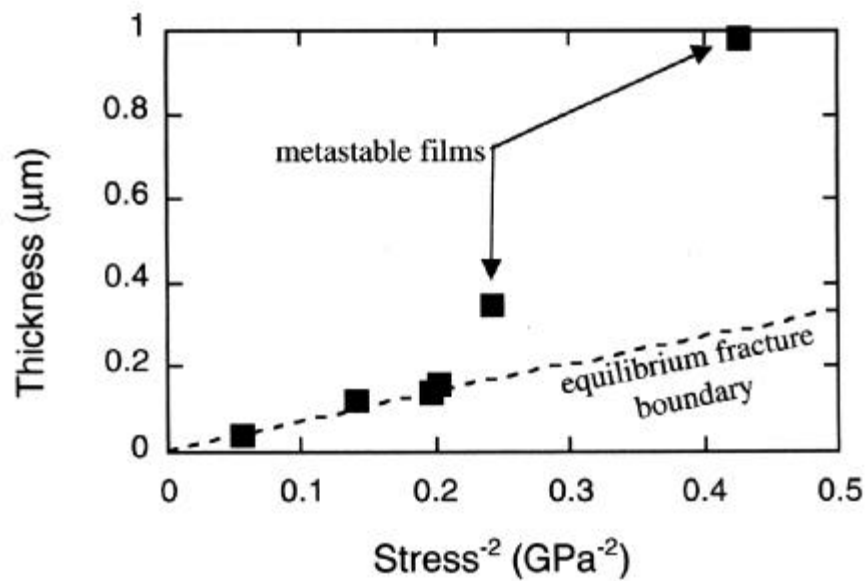


Figure 2. The measured critical thickness for fracture in $\text{Al}_{1-x}\text{Ga}_x\text{N}$ alloys. The dashed line is the calculated equilibrium critical thickness using a simple energetic theory of fracture.

Electronic Transport in Complex Molecular Solids

D. Emin

Motivation—Electronic transport in molecular solids often occurs by successions of phonon-assisted hops between states centered on different molecules. Each jump occurs as an electronic carrier adjusts to atoms' motions by moving between molecules. A hop can occur when atomic motions cause the energy of the electronic state on the final site to fall below that of the initial site. Prior studies of hopping motion have presumed that the carriers occupy rigid states. However, the electronic states of large complex molecules tend to be highly polarizable. As such, these molecular states alter their size and shape in response to atomic motions. To address intermolecular electronic hopping, a means to calculate phonon-assisted transition rates between deformable electronic states needed to be developed.

Accomplishment—The adiabatic (Born-Oppenheimer) approach has been utilized to address the formation and semi-classical hopping motion of molecular polarons. Deformation of a carrier's wavefunction induced by atomic motions is explicitly considered. The sloshing motion of a carrier in response to atomic movement always reduces the stiffness constants of the atomic motions to which the carrier responds. The concomitant carrier-induced reduction of the vibrational free-energy provides a heretofore ignored contribution to the carrier's binding energy.

A scaling approach is used to express the energy of the system as a function of the size of the electronic state. Each contribution to the free-energy manifests a different dependence on the size of the carrier's state. Carrier-induced softening increases in importance with enlargement of the carrier's state. By contrast, the binding produced by displacements of atoms of the

occupied molecule vary inversely with the volume encompassed by the carrier. However, the binding energy arising from a carrier's interaction with ionic surroundings falls more slowly as the size of the carrier's state is increased. The groundstate minimizes the free energy with respect to the carrier's radius. As illustrated in Fig. 1, there are three possible groundstates for a carrier confined to a molecule immersed within an ionic medium. Depending on the values of the physical parameters, the carrier either 1) collapses to a single atom, 2) condenses to a subset of the molecule's equivalent sites, or 3) expands to occupy all equivalent sites of the molecule.

Semiclassical hopping occurs at high enough temperature for atomic motion to be treated classically. In this regime, a hop occurs as atoms pass through a configuration in which the carrier is shared between initial and final sites. As illustrated in Fig. 2, the electronic states at both initial and final sites tend to expand at this coincidence configuration. This expansion can significantly reduce a hop's activation energy. The carrier's deformability also affects the pre-exponential factor for a hop. In particular, changes of the vibrational entropy arising from carrier-induced softening link the hopping activation energy to the pre-exponential factor.

Significance—This work explains the qualitative differences that are observed between hopping between small states in non-polar material and hopping between large states immersed within ionic environments. Carrier-induced softening also provides an explanation of the observed link (Meyer-Neldel, 1937) between the activation energy of a hop and its pre-exponential factor.

Sponsors for various phases of this work include: BES Materials Sciences

Contact: David Emin, Nanostructure and Semiconductor Physics Dept., 1112

Phone: (505) 844-3431, Fax: (505) 844-1197, E-mail: demin@sandia.gov

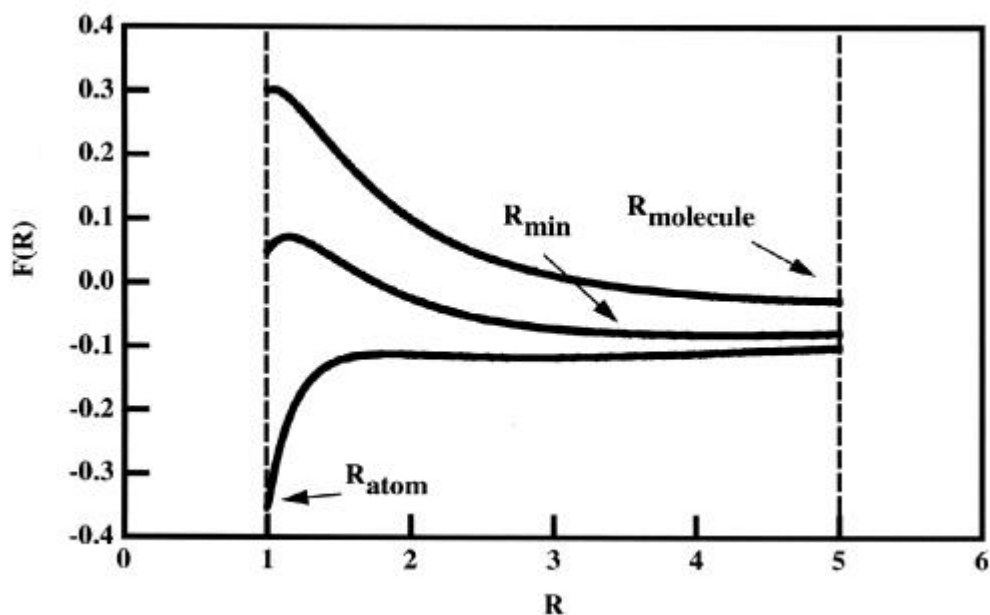


Figure 1. The free energy of the system comprising a carrier confined to a molecule immersed in an ionic medium, $F(R)$, is plotted versus the carrier's radius, R , in dimensionless units. Depending on the physical parameters, the free energy has three possible minima. The carrier collapses to an atom, spreads over a few equivalent sites, or extends over the entire molecule.

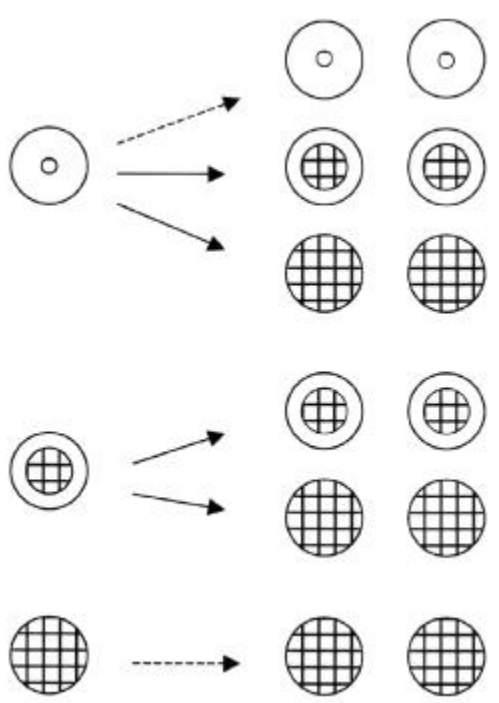


Figure 2. A carrier's local state (hatched regions) tends to expand as it hops between molecules (open circles). Dashed lines designate processes where size changes are limited by geometrical constraints.

Novel Energy Conversion Devices of Icosahedral Borides

T. Aselage, D. Emin¹, W. Zhang, S. Hersee¹, R. Wang¹, R. Ewing², and L. Wang²

¹The University of New Mexico, ²The University of Michigan

Motivation—Large quantities of energy are available from β -particles emitted from radioactive sources. Schemes to capture this energy envision solid-state devices that collect the electrons and holes generated by β -particles passing through semiconductors. However, β -irradiation of conventional semiconductors produces accumulations of displaced atoms that disrupt the electronic transport. This damage precludes using conventional semiconductors in these novel energy conversion devices.

By contrast, icosahedral borides, boron-rich solids built from twelve-atom icosahedral clusters, survive intense bombardments without observable damage. Atoms displaced from icosahedra appear to spontaneously recombine with icosahedral vacancies. This "self-healing" of damage in icosahedral borides removes a fundamental impediment to making solid-state devices that efficiently convert β -particles' energies to electricity. We mean to assess the feasibility of such devices by confirming "self-healing" of radiation damage, by establishing growth of high-quality films of icosahedral boride semiconductors, and by assessing their electrical response to irradiation.

Accomplishment—We have now confirmed the self-healing of icosahedral borides' radiation damage. Samples have been bombarded with electrons having comparably high energies to emitted β particles. Bombardment rates exceeded those from β -emitting sources by many orders of magnitude, with total doses corresponding to hundreds of years of exposure to intense radioactive β -emitters. Despite these severe bombardments, high-resolution TEM images, illustrated by Figs. 1a and 1b of elemental boron, find no evidence of damage.

Icosahedral borides are refractory solids, having melting temperatures above 2100C. Nevertheless, we were able to grow 100 nm thick films of elemental boron and $B_{12}As_2$ in a conventional CVD reactor by operating it at its highest temperature, 1150C. Annealing studies of these films indicate that modifying our reactor to achieve higher growth temperatures, 1300C, will enable us to reliably produce thicker, high-quality films.

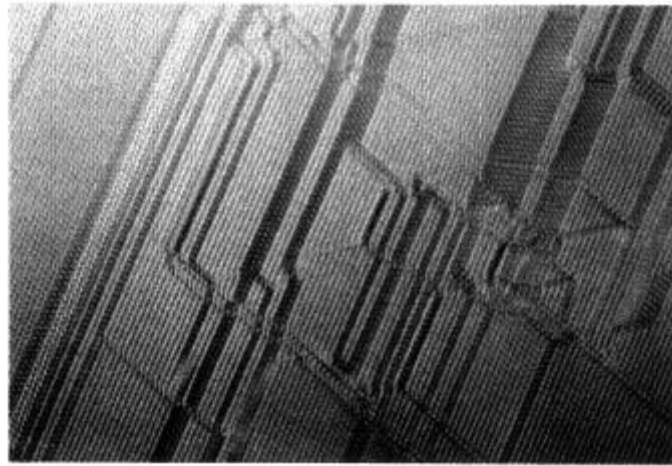
Our first icosahedral-boride films were of elemental boron. Elemental boron is the least promising icosahedral boride for our purpose since its dark transport is dominated by the low-mobility hopping of a high density of localized holes. Nonetheless, exposure of boron films to a photon source whose intensity mimics that of β -emitters produces a sizeable photo-generated current. We have measured the temperature dependencies of the photo-current and its decay rate, the (isothermal) intensity dependence of the photo-current, and the photo-Seebeck effect. The results imply radiation-induced transport being dominated by n-type carriers that recombine with trapped holes.

Significance—The direct conversion of nuclear energy into electricity is a long-held goal. Energy conversion devices that produce electricity from β -decays could be compact, long-lived sources of sustained power. Our confirmation of "self-healing", CVD growth of films and measurement of a significant electrical response mark substantial progress toward demonstrating the feasibility of novel energy conversion devices of icosahedral borides.

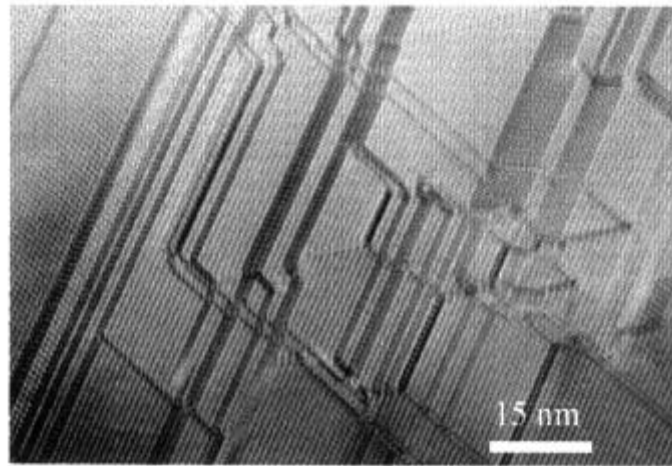
Sponsors for various phases of this work include: DARPA

Contact: Terry Aselage, Nanostructure and Semiconductor Physics Dept., 1112

Phone: (505) 845-8027, Fax: (505) 844-4045, E-mail: tlasela@sandia.gov



(a)



(b)

Figure 1. High-resolution transmission electron micrographs of elemental boron before (a) and after (b) bombardment with 400 keV electrons at 10^{20} electrons/cm²-sec. The net dose of 10^{23} electrons/cm² corresponds to hundreds of years of exposure to ^{144}Ce or thousands of years of exposure to ^{90}Sr . No damage is observed. Even the microstructure (twins and stacking faults) remains unaltered.

Thermophotovoltaic Materials and Device Development

R. M. Biefeld, C. I. H. Ashby, S. R. Lee, S. R. Kurtz, A. G. Baca, and P. -C. Chang

Motivation—We are investigating thermophotovoltaic (TPV) materials and devices for use in converting infrared radiation by means of a semiconductor photodiode to produce electricity. The potentially high power density, quietness, and low maintenance of these devices make them of interest for a variety of military and civilian uses including military and recreational vehicles, portable power sources, and remote dwellings. Practical and cost effective deployment of such systems poses several engineering and materials science challenges. Large arrays of these TPV devices will be needed to generate enough power for some applications. One approach to achieve this power is to use series connected photovoltaic cells in an integrated module. This approach requires that the individual cells be electrically isolated. This can be achieved using either a semi-insulating substrate or an isolation diode if a conducting substrate is used. The goal of this research is to meet this challenge by exploring the development of both cell isolation diodes using AlGaInAsSb device technology as well as lattice mismatched heteroepitaxy on GaAs or InP substrates.

Accomplishment—In order to convert thermal radiation efficiently to electricity one must use a semiconductor with a band gap energy close to the energy of the infrared radiation being emitted by the source. The maximum of the spectral emittance of a blackbody of a radiator at a temperature of 1000°C requires a material with an energy bandgap of about 0.5 eV (2.5 μm). Figure 1 illustrates the variation of bandgap versus lattice parameter for the common III-V

semiconductors. By following a horizontal line at 0.5 eV one can see which materials are available at this bandgap energy. We have chosen to develop photodiodes using InGaAsSb quaternaries lattice matched to GaSb substrates. Because large-scale deployment of TPV systems would require the use of monolithically integrated modules we have chosen to investigate the possibility of using either a semi-insulating substrate such as GaAs or InP or the use of cell isolation diodes involving the growth and doping of AlGaAsSb lattice matched to GaSb substrates. Towards this end we have investigated the growth and doping of InGaAsSb and AlGaAsSb quaternaries lattice matched to GaSb using metal-organic chemical vapor deposition (MOCVD) in a high-speed rotating disk reactor. To date we have grown lattice matched InGaAsSb with n-type doping levels of 1 to 3 $\times 10^{18} \text{ cm}^{-3}$ and undoped p-type levels of 1.5 $\times 10^{16} \text{ cm}^{-3}$.

We have also established plasma etching processes for this material to assist in the device formation for the integrated modules using an inductively coupled BCl_3 plasma. We have used x-ray diffraction and reciprocal space mapping (Fig. 2) to elucidate the structural properties of a variety of grading schemes used to grow lattice mismatched InGaAs and InGaAsSb on InP and GaAs substrates.

Significance—The development of monolithically integrated TPV modules will enable the deployment of a variety of energy sources for both military and private uses.

Sponsors for various phases of this work include: WFO and DP Research Foundations

Contact: Robert M. Biefeld, Semiconductor Material and Device Sciences Dept., 1113

Phone: (505) 844-1556, Fax: (505) 844-3211, E-mail: rmbiefe@sandia.gov

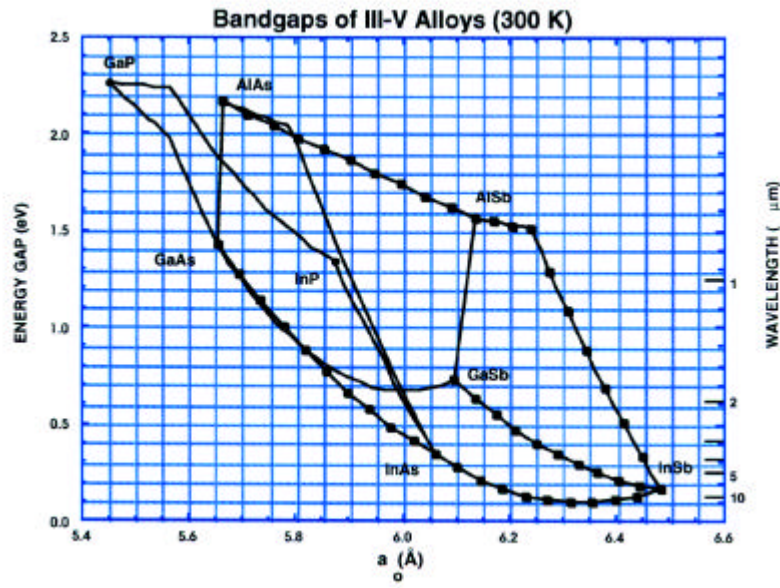


Figure 1. Bandgap versus lattice constant of III-V compound semiconductors.

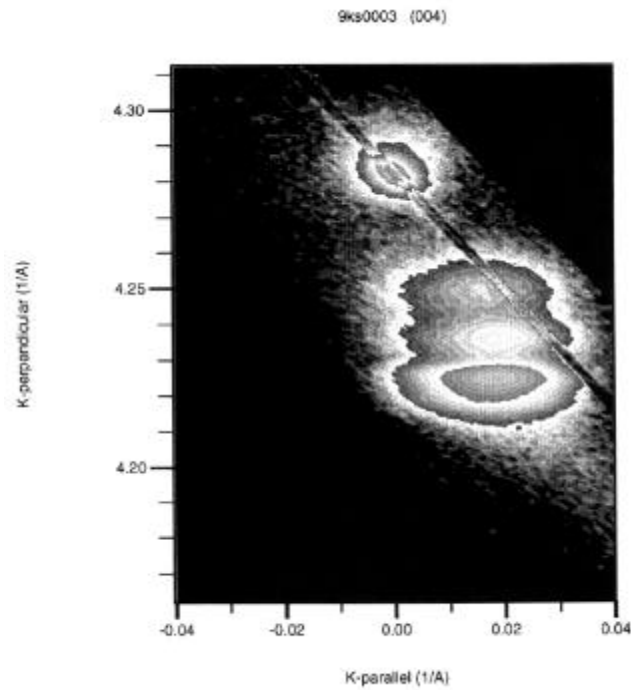


Figure 2. Reciprocal space map of the (004) x-ray diffraction pattern of a three layer InAsP grading scheme on a GaAs substrate.

Terahertz Detection in Double Quantum Well Devices

J. A. Simmons, J. S. Moon, N. E. Harff, J. L. Reno, S. K. Lyo, and W. E. Baca

Motivation—The electromagnetic spectrum from 0.3 to 10 THz is scientifically rich and has substantial potential technological applications, including battlefield imaging, covert space-based ultra-high bandwidth communications, atmospheric sensing, collision avoidance, and biological/chemical sensing and spectroscopy. Despite this tremendous potential, however, solid state THz devices are largely lacking, and an unfilled gap in technology exists in this part of the spectrum. Semiconductor electronic devices are limited by parasitic RC and transit times to below 1 THz, interband semiconductor photonic devices are limited to frequencies above their bandgap, higher than 10 THz.

Accomplishment—Because semiconductor quantum wells (QW's) are man-made systems whose energy subbands can be engineered over a wide range, a device based on intra-band transitions can easily access the THz regime. To help fill this technological gap, Sandia—with P. Burke and J. Eisenstein at Caltech and X. Peralta and S. J. Allen at UCSB—is researching a novel THz detector based on photon-assisted tunneling (PAT) in double QW structures. Independent ohmic contact is made to the 2D electron layer in each QW by locally depleting electrons from the QW one doesn't wish to contact.

In the absence of THz illumination, current flows between the two QWs only when their energy subbands are precisely aligned. This is due to the simultaneous conservation of both energy E and in-plane momentum k . However, under illumination a THz photon can act to complete the energy conservation conditions even when the two subbands are *not* aligned. This PAT process is similar to that observed in SIS tunnel junctions, and is also described by the

theory of Tien and Gordon. Unlike SIS junctions, however, the THz regime can easily be accessed. Further, because only a single photon energy is absorbed, regardless of the momentum of the electron, the detector is extremely narrowband (~ 0.5 meV) in its response. (In a sense, the detector is a quantum cascade laser in reverse.) In addition, a DC bias applied to front and/or back control gates allow the detected photon energy to be tuned over an order of magnitude.

Several initial photodetector structures have been fabricated at Sandia and measured in the free electron laser facility at UCSB. The detector active areas are only of order 10×10 microns. The control gates are attached to large area bowtie antennas in order to achieve efficient coupling of the radiation. While a strong photoresponse has been observed, particularly at lower frequencies such as 0.3 THz, to date it has not been possible from the data to differentiate between photon-assisted tunneling and a purely bolometric response. New growth designs and structure geometries have been created in order to reduce in-plane heating within the QWs and increase power absorption in the tunneling region.

Significance—Semiconductor devices operating in the THz regime are becoming of increasing interest for dual use applications, and will eventually play a large technological role. If successful, present efforts to extend the intra-band quantum cascade laser into the THz band will require a highly sensitive, fast response-time detector. Our research into such a detector based on photon-assisted tunneling in double quantum wells appears highly promising as a means of fulfilling that need.

Sponsors for various phases of this work include: LDRD and WFO (DARPA)

Contact: Jerry A. Simmons, Semiconductor Material and Device Sciences Dept., 1113
Phone: (505) 844-8402, Fax: (505) 844-1197, E-mail: jsimmon@sandia.gov

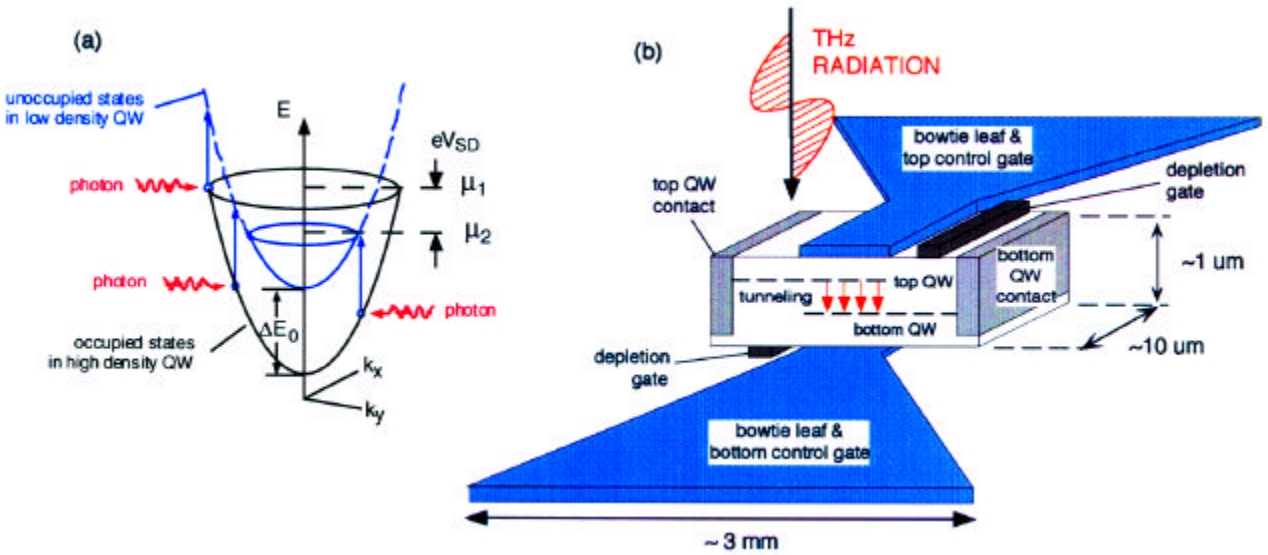


Figure 1. (a) Diagram of the allowed states in a double quantum well plotted in energy E vs. in-plane momentum $k_{||}$ space. Only a THz photon of a precise energy ΔE_0 can provide the energy necessary for an electron to tunnel from one QW to the other, regardless of the value of $k_{||}$. (b) Sketch of the detector geometry. The active double quantum well region is of order 10×10 microns, and has a thickness of only ~ 1 micron. The top and back control gates comprise the leaves of a bowtie antenna of several mm extent, providing efficient coupling of the Thz electric field.

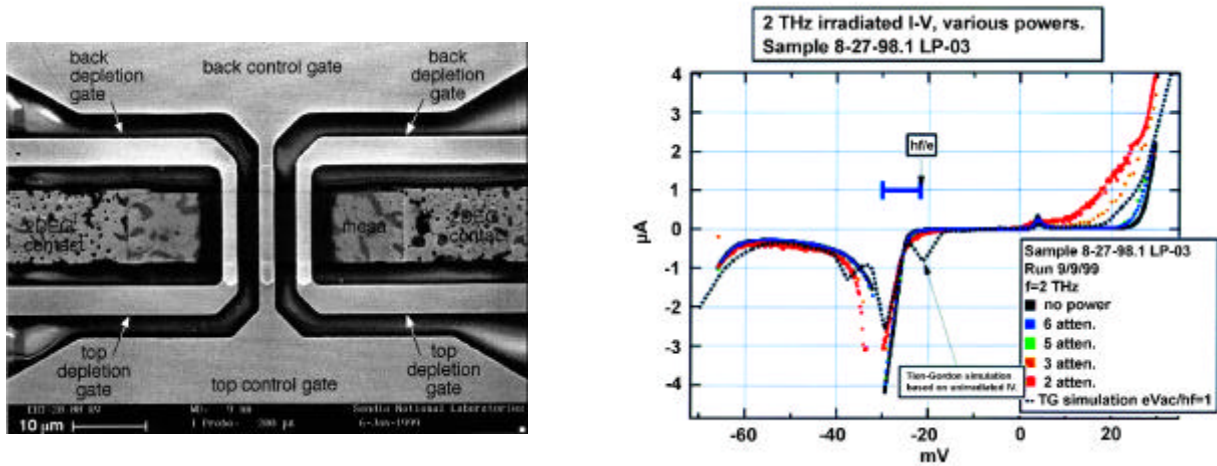


Figure 2. (a) Scanning electron micrograph of a completed bowtie-antenna coupled double quantum well THz detector. The semiconductor epitaxial layers are sufficiently thin to be transparent to the electron beam, rendering features on both the front and back surfaces visible. The 10×20 micron rectangular mesa is visible in the center. Also visible are the ohmic contacts, front and back depletion gates, and the front and back control gates which fan out to form large bowtie antennas outside the photograph. (b) I-V curve of the detector at various 2 THz illumination intensities. A strong bolometric response is observed. The narrow photon-assisted tunneling peaks predicted by Tien-Gordon theory are absent, presumably due to heating of the 2D electrons in the ungated regions.

Exciton Mass in InGaAsN Photovoltaic Materials

E. D. Jones, A. A. Allerman, S. R. Kurtz, N. A. Modine, and A. F. Wright

Motivation—A new semiconductor alloy system, InGaAsN, holds potential as an important material for multi-junction solar cells with efficiencies greater than 40% and for 1eV-range laser systems. The introduction of small amounts of nitrogen (~2%) in the InGaAs alloy system greatly reduces the band gap energy, with reductions approaching 0.5 eV! The initial portion of this research program is thus aimed at understanding the fundamental nature of the effect of adding substitutional isoelectronic nitrogen atoms for arsenic. Also a question of importance is, besides the effect on the bandgap energy, what other material properties are strongly affected or modified by the introduction of a small amount of nitrogen into GaAs?

Accomplishment—A series of InGaAsN alloys with varying nitrogen concentrations and with the indium content adjusted to provide lattice matched conditions were grown using metal organic chemical vapor deposition (MOCVD) reactors. In the first study we investigated the photoluminescence energy and line shape for varying growth conditions. Studies of the photoluminescence line width and intensity for these samples were performed in order to determine the optimum growth parameters and conditions. A typical 4 K photoluminescence spectrum for a 1% nitrogen sample is shown in Fig. 1. The experimental full-width-at-half-maximum (FWHM) line width is about 18 meV. An interpretation of this FWHM value in terms of alloys fluctuation theories can be used to infer the effective exciton mass to be about 0.10 which is to be compared with the pure GaAs value of 0.04! Our recent band structure calculations suggest that the reduction to the bandgap

energy is a result of Γ -X and Γ -L mixing between the GaAs conduction band states. With this strong mixing, we also expect mass changes. In order to study the effect of mixing and the resultant change in mass, we measured the hydrostatic pressure dependence of the FWHM between ambient and 120 kbar with the result shown in Fig. 2. A miniature diamond anvil cell with helium as the pressure medium was used to produce hydrostatic pressures. Using the current theories for the photoluminescence line width based on alloy fluctuations the effective exciton mass can be inferred from the FWHM line width data shown in Fig. 2. Figure 3 shows the increase in the exciton effective mass as a function of pressure. This increase is a direct result of increased Γ -X mixing with pressure, and hence an increased mass change because of the heavy X-point mass. The current theoretical challenge is to accurately calculate the mass and its pressure dependence from a first principles approach.

Significance—Modern satellite performance depends critically on the development of high efficiency solar cells. Calculations show that incorporating a 1 eV band gap material into existing GaAs-based multi-junction tandem solar cells can increase the overall solar cell efficiency by as much as 10%, with maximum theoretical efficiencies for the tandem cell greater than 40%. These increased efficiencies could lead to smaller (and lighter) solar cell panels for spaced-based applications. The present effective mass measurements for these alloys will yield information regarding the ideal and actual values of the carrier mobilities for these kinds of solar cells.

Sponsors for various phases of this work include: BES, LDRD, and CRADA

Contact: Eric D. Jones, Semiconductor Material and Device Sciences Dept., 1113

Phone: (505) 844-8752, Fax: (505) 844-3211, E-mail: edjones@sandia.gov

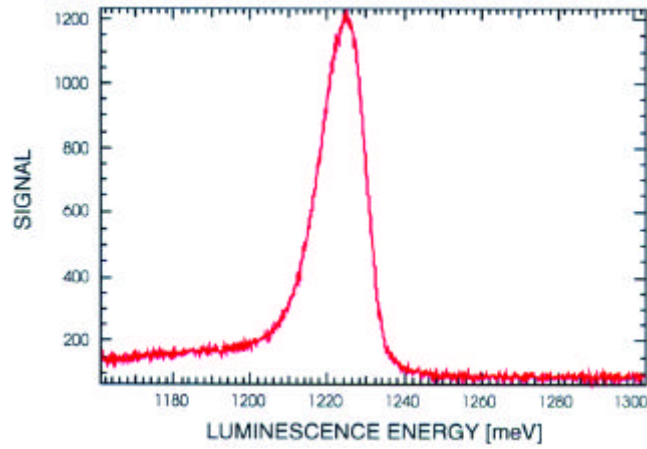


Figure 1. Low temperature (4K) photoluminescence spectrum for an 1%N epilayer film lattice matched to GaAs. The band gap energy is 1222 meV and the FWHM is about 18 meV.

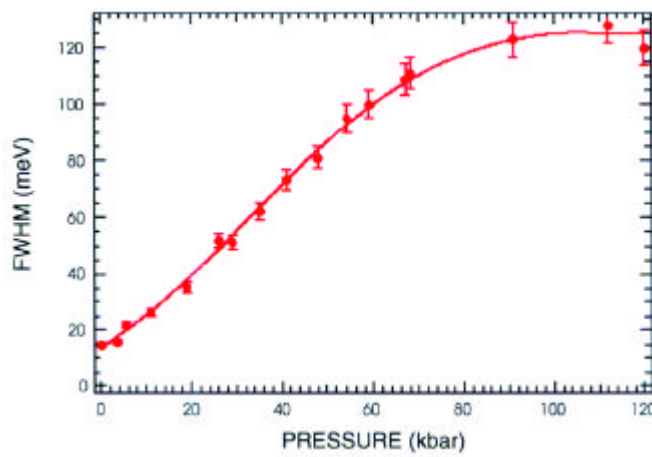


Figure 2. Pressure dependence of the FWHM line width.

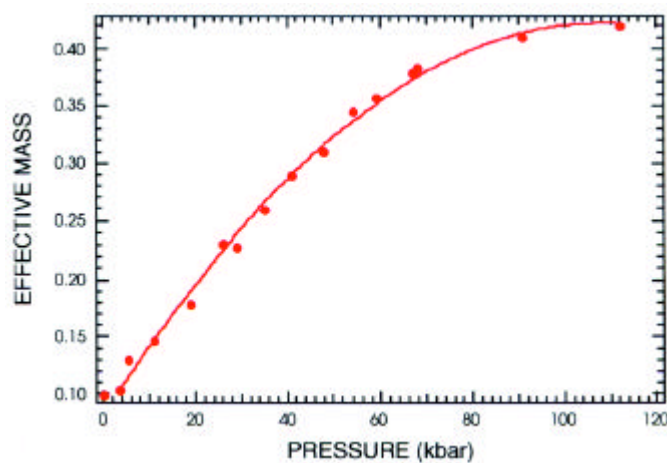


Figure 3. Pressure dependence of the exciton effective mass for 1% N InGaAsN alloy.

Tribological Properties of Self-Assembled Monolayers on Si

J. E. Houston

Motivation—Considerable interest has been generated over the last several years in the possible use of surface anchored, self-assembled molecular monolayers (SAMs) as lubricants in microdevices, e.g., advanced disc drives and micro-electro-mechanical systems. These films offer the advantages that they are "dry", thin and robust with high break-down strength and low friction coefficients. In addition, they can be tailored to adapt to the interfacial surfaces of interest. However, the detailed chemistry behind the tailoring process is, at present, the limiting factor and one of the focus areas of our effort.

Accomplishment—We have used the Interfacial Force Microscope to quantitatively measure both the normal and lateral forces generated by the contact of ~ 100 nm W probes with self-assembled monolayer films on Si surfaces. We compare friction results for films grown by two chemical routes: one by chlorosilane chemistry on the native Si oxide surface using two precursors (ODTS- $\text{CH}_3(\text{CH}_2)_{17}\text{SiCl}_3$ and PFTS- $\text{CF}_3(\text{CF}_2)_7(\text{CH}_2)_2\text{SiCl}_3$) and the other involving a chlorinated clean-Si surface and alkyl-alcohol ($\text{CH}_3(\text{CH}_2)_{18}\text{OH}$) precursor. This second route is being developed by Professor X.-Y. Zhu at the University of Minnesota and looks very promising as a more controllable film. In Fig. 1 we illustrate two ways of observing friction in these thin films. Figure 1a shows the results of force profiles (i.e., loading curves) for the ODTS and PFTS films. We have shown in previous work that the degree of hysteresis in the approach and withdrawal curves is directly related to the friction and we can see from this plot that the friction is nearly equal in the two films. In Fig. 2b we show a direct measure of

the friction force as a function of normal load done by the "friction-loop" method. Thin films generally show friction directly proportional to load which permits the determination of a friction coefficient. We see from these results that under very high stresses (the 3 GPa level is indicated) the coefficients are about 0.13 and similar for the two films (the shorter PFTS being slightly higher). Figure 2 shows a direct comparison for the ODTS and alkyl-alcohol monolayers. Disappointingly, the latter films show higher friction. However, subsequent work indicated that the Si chlorination step had roughened the surface reducing the film's order and increasing the friction. Further work will correct this difficulty. Wear in all three films is very low with no breakdown observed even at very high stresses. Their only negative attribute is an aging effect resulting from an environmental attack on the chemical anchor (head-group bond) to the substrate, e.g., by ozone. Future work will address this problem and its solution in more detail. Although the tribological properties for SAMs on Si are not as spectacular as for alkanethiol films on Au, they still show strong promise as controlled lubricants on small devices.

Significance—These are the first quantitative, nanometer-level measurements of SAM lubricants on Si surfaces. The preliminary results indicate that their tribological properties are truly extraordinary. In addition, the results pave the way for future studies aimed at the development of the proper interfacial chemistry to tailor the films for a broader range of materials, e.g., poly Si, Si nitrides and metals, etc., and to relieve the problem of film aging.

Sponsors for various phases of this work include: BES

Contact: J. E. Houston, Surface and Interface Sciences Dept., 1114

Phone: (505) 844-8939, Fax: (505) 844-4045, E-mail: jehoust@sandia.gov

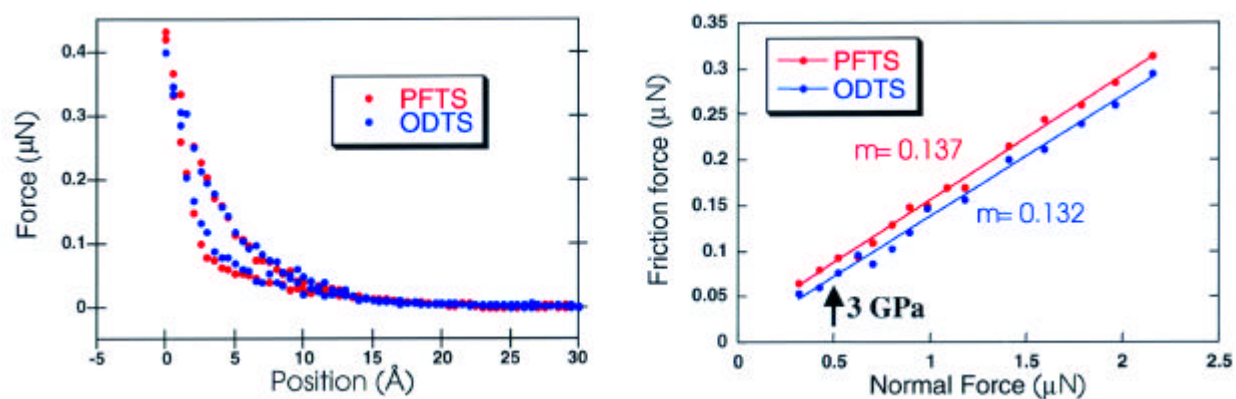


Figure 1. (a) Force profiles (loading curves) for a ~ 100 nm W tip contacting PFTS and ODTS chlorosilane-derived self-assembled monolayer films on the Si(001) surface. The degree of hysteresis between the loading and unloading curves is indicative of the frictional loss in compressing the films. (b) Frictional force vs. normal load obtained by the "friction loop" method. The observed linear relationship between the two forces reflects the thin-film nature of the SAMs and permits a friction coefficient to be obtained. As expected the shorter PFTS film has a slightly higher coefficient value.

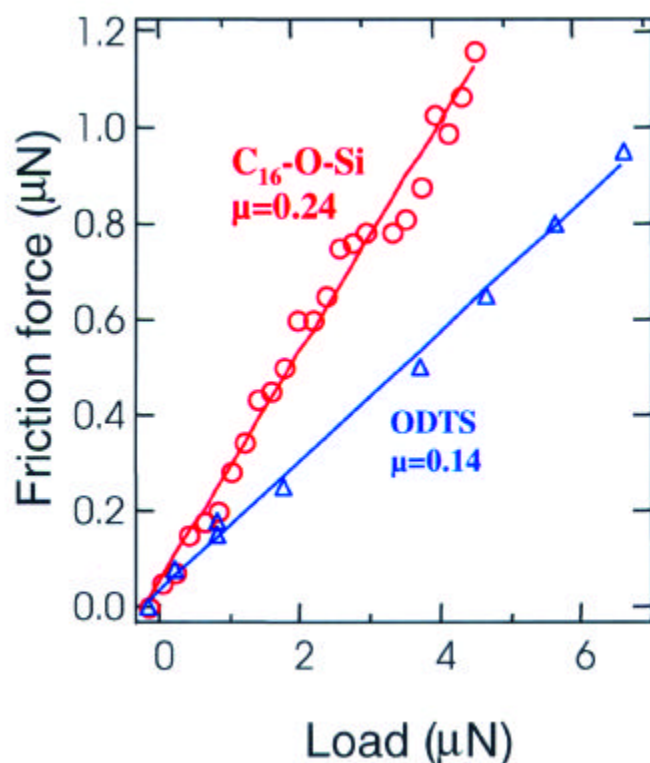


Figure 2. Friction results for a ~ 100 nm W tip contacting a self-assembled monolayer of C₁₈ alkyl-alcohol precursor molecules reacted with a Cl covered Si(001) surface, creating a CH₃(CH)₁₇-O-Si interfacial bond, directly compared with that from an ODTS monolayer similar to that used for the data of Fig. 1. The C₁₈-O-Si film has a friction coefficient more than double that for the ODTS monolayer, which was found to be the result of surface roughness created by the Cl etching of the clean Si prior to the creation of the SAM film.

Self-Assembly and Viscoelastic Response of Alkanethiol Monolayers

N. D. Shinn

Motivation—Molecular self-assembly is a technologically promising but inadequately understood process for nanostructured materials fabrication. Whereas early investigations of self-assembled monolayers reported almost trivial deposition procedures for obtaining ordered molecular arrays, subsequent structural studies have revealed not only hierarchical levels of structural complexity but also sensitivity to the synthetic pathway. Diffraction techniques and scanning microscopies have identified a sequence of ordered equilibrium phases during the growth process but the mechanistic pathway of self-assembly remains unknown. Moreover, the structure:property relationships of these molecular ensembles must be understood before directed self-assembly can be exploited as a useful synthetic tool.

Accomplishment—We have developed a new, high sensitivity acoustic wave damping technique for simultaneous measurements of the growth kinetics and viscoelastic mechanical properties during self-assembly. For alkanethiol monolayers, increasing the alkane chain length opens a new precursor-mediated adsorption channel, yields progressively greater elastic shear moduli, and significantly reduces dissipative losses within the film. The acoustic wave damping technique utilizes the polycrystalline Au(111) electrodes of an vibrating 5 MHz quartz crystal microbalance (QCM), shown schematically in Fig. 1, as the substrate onto which alkanethiol molecules are adsorbed from the gas phase at low pressures. The QCM resonant frequency shift provides a direct measure of the adsorption kinetics. In addition, the oscillatory lateral translation of the electrodes induces a dynamic shear deformation in the molecular

layer, leading to elastic energy storage and energy dissipation. For densely-packed monolayers consisting of well-ordered domains of vertically inclined molecules, the storage modulus increases linearly with alkane chain length. Since the intermolecular van der Waals interactions that stabilize the ordered domains also increase with chain length, these results indicate that monolayer elasticity increases because of stronger forces between aligned molecules undergoing coherent librational motion.

A quantitative comparison of real-time energy dissipation during growth (Fig. 2) shows that dissipation is consistently higher for a nine-carbon thiol than a five-carbon thiol. A twelve-carbon thiol is sufficiently long to switch to precursor-mediated adsorption, in which the initial viscous precursor phase facilitates the growth of a low-loss monolayer. Hence short alkanethiols with weak interactions lead to poor ordering, low dissipation and low elasticity. Monolayers of moderate chain length molecules are ordered with increased elasticity, stronger interactions and subsequently more dissipation modes. Ten-carbon thiols have sufficiently strong interactions to form a new precursor phase and well-ordered elastic domains.

Significance—This work reveals how even subtle aspects of molecular structure can impact both the self-assembly process and monolayer viscoelastic properties. By inertially inducing a shear deformation in the growing monolayer, the acoustic wave damping technique enables phase-dependent intrinsic mechanical properties to be measured without extrinsic contributions due to probe-sample interactions.

Sponsors for various phases of this work include: BES Materials Sciences

Contact: Neal D. Shinn, Surface and Interface Sciences Dept., 1114

Phone: (505) 844-5457, Fax: (505) 844-5470, E-mail: ndshinn@sandia.gov

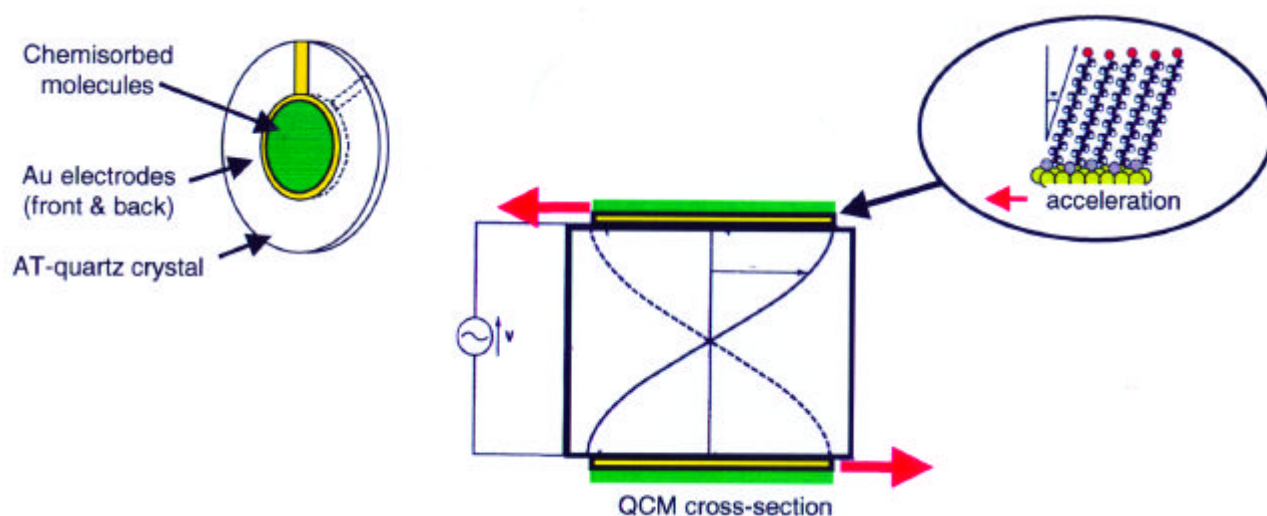


Figure 1. The high frequency lateral acceleration of the Quartz Crystal Microbalance electrodes inertially shears a molecular monolayer chemically adsorbed onto the gold electrode surface. Energy stored and dissipated within the molecular layer is extracted from changes in the QCM frequency response function.

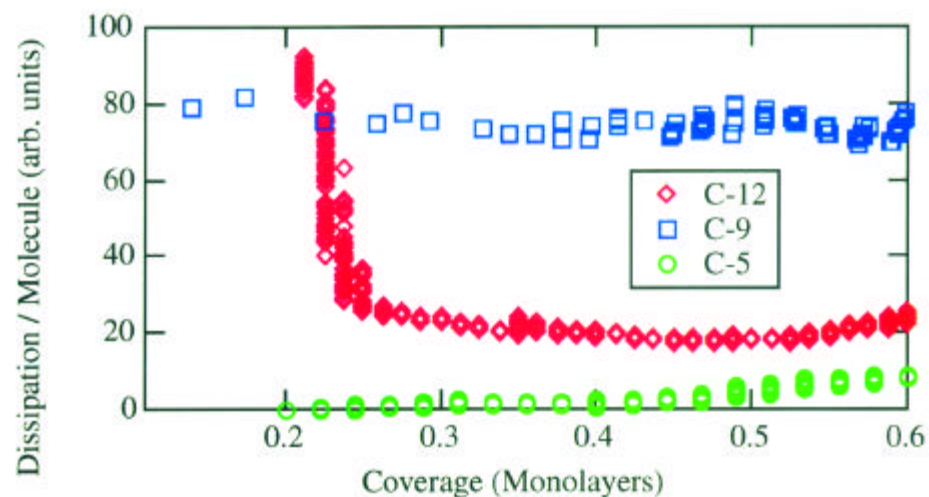


Figure 2. A comparison of the average energy dissipation/molecule measured during monolayer self-assembly for alkanethiols of increasing alkane chain length. Longer chain molecules (e.g., C-12 above) exhibit different adsorption kinetics and ensemble viscoelastic properties due to chain/substrate interactions.

Metal Deposition, Growth and Adhesion at Oxide Surfaces

D. R. Jennison and A. Bogicevic

Motivation—The surfaces of metal oxides are poorly understood compared with semi-conductor or metal surfaces, in spite of wide-spread use in microelectronics, sensors, seals, and heterogeneous catalysts, as well as issues concerning adhesion and corrosion. Frequently, applications involve interfaces between oxides and metal overlayers; however, the strength and even the basic nature of the interaction has been a subject of controversy. Therefore, we have undertaken a systematic study of the binding of both isolated metal atoms and metal overlayers to oxide surfaces, and are also addressing issues such as wetting and the nucleation of metallic islands. Perfect but also realistic defective and contaminated surfaces are being studied.

Accomplishment—Using first principles density functional theory, we first made a systematic study of eleven different metals on a model alumina film. We found a general rule for the basic nature of the interaction, which was first suggested by an earlier study of a few metals on sapphire (also known as corundum or $\alpha\text{-Al}_2\text{O}_3$). Isolated metal atoms are oxidized by the surface, and binding strength is determined by the ionic radii and degree of ionization (a prediction of multiply ionized transition metal atoms to the left of the Periodic Table has just been confirmed by work at Stanford). Meanwhile, metal overlayers have little or no charge transfer to the surface and bind mainly by polarization, influenced quantitatively by the shape of the metal valence orbitals. These trends are likely to apply to all highly ionic oxide materials.

We next studied the widespread belief that isolated vacancies at an oxide surface (a common

defect) would nucleate metal islands. Instead, we found that isolated vacancies in fact destabilize metal dimers, the first step in island growth, but that isolated adsorbed hydroxyl groups (a common contaminant arising from dissociated water) strongly stabilize dimers. This agrees with recent experimental work at the Fritz-Haber Institute in Berlin, which showed that hydroxylation could be used to control the dispersion of metal particles on a model catalyst support.

Finally, we addressed the issue of a high concentration of surface hydroxyl groups. We predicted that 1/3 monolayer of OH on alumina would increase the binding of metallic copper by 2.5 times, and cause it to wet the surface by preventing isolated atoms from diffusing at room temperature. Indeed, this effect has been seen this year in experiments done on hydroxylated sapphire at Univ. North Texas. Further calculations showed that the presence of metal would cause the dissociation of the OH groups, indicating that adsorbed oxygen atoms alone would produce the same effect.

Significance—These results suggest methods of tailoring the adhesion and growth of metals on oxide surfaces. For example, hydroxyl coverage can be produced by exposure to water or water plasma, while adsorbed oxygen atoms can be introduced by a slow cool-down in oxygen plasma, by exposure to nitrous oxide (with a UV source to dissociate the molecule), or by exposure to ozone. Further experimental work using specially prepared oxide surfaces is being encouraged, in order to perfect procedures for improving interface quality during microelectronics processing and/or brazing.

Sponsors for various phases of this work include: DP Research Foundations and LDRD

Contact: Dwight R. Jennison, Surface and Interface Sciences Dept., 1114

Phone: (505) 845-7737, Fax: (505) 844-4045, E-mail: drjenni@sandia.gov

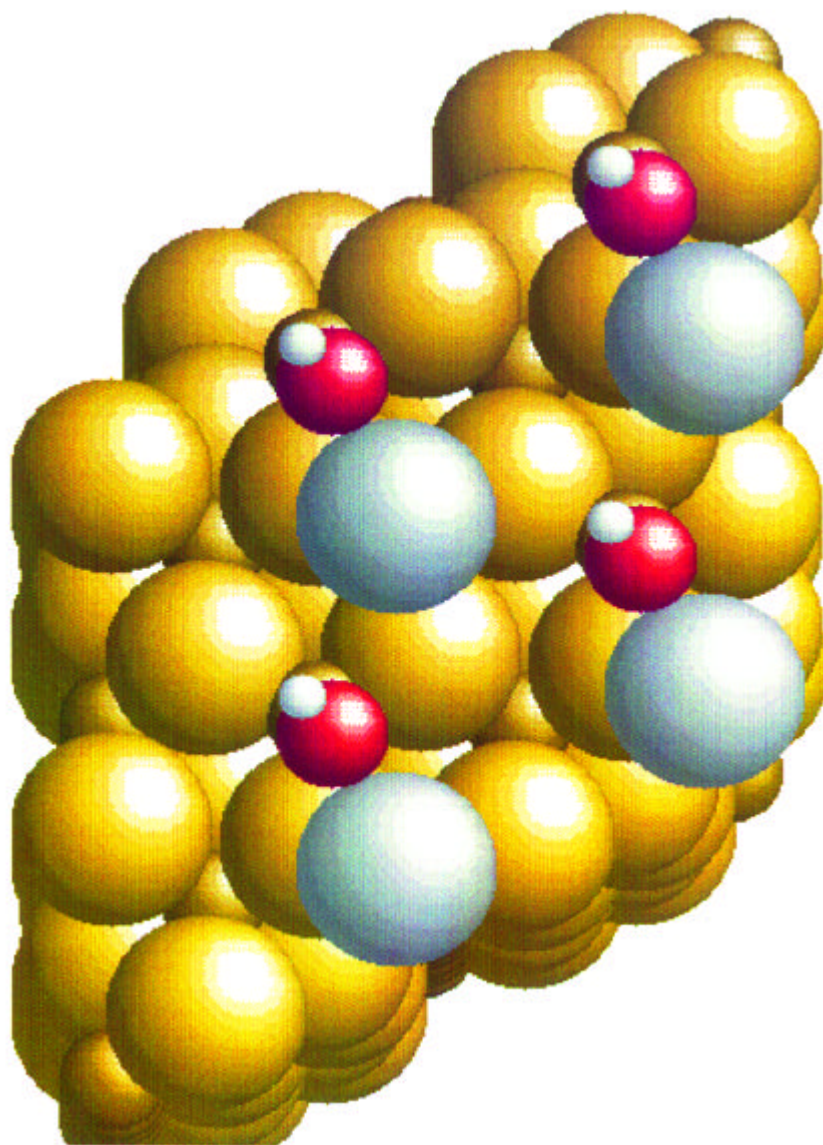


Figure 1. Adsorbed hydroxyl groups pin metal atoms at room temperature, causing wetting and a subsequent dramatic increase in adhesion. Here the relaxed structure of Cu and OH on alumina is shown.

Atom Diffusion Controls Dynamics of Surface Phase Transition on Si (111)

J. B. Hannon, N. C. Bartelt, B. S. Swartzentruber, and G. L. Kellogg

Motivation—Materials that undergo phase transitions can dramatically change their properties as a result of small external inputs. Understanding the dynamics of phase transitions is an important step in the quest to develop responsive materials. In many systems, phase transitions require the transport of atoms from one phase to the other due to differences in atomic density. In these cases, the kinetics of mass transport can be just as important as the thermodynamic differences between the two phases in defining the rate of the transformation. Although such diffusion processes can be treated theoretically, they are difficult to address experimentally. By studying phase transitions on a surface, we are able to quantify the mass transport process and assess its importance in controlling the dynamics of the transition.

Accomplishment—We used low-energy electron microscopy (LEEM) to show for the first time that adatom diffusion controls the dynamics of the phase transition between the 7x7 and 1x1 surface structures on Si(111). The equilibrium structure of the Si(111) surface at room temperature is a complicated reconstruction with 7x7 periodicity. At a temperature of 820C this surface undergoes a first-order phase transition to a structure that gives a 1x1 diffraction pattern. This high-temperature 1x1 phase is a dense overlayer of adatoms (6% more dense than 7x7) residing on the bulk-terminated structure. To study the dynamics of the transition, we made real-time observations of the time evolution of triangular (7x7) domains during growth of the 1x1 phase. Figure 1 shows a series of LEEM images taken as the surface transforms from the 7x7 to 1x1 structure. The bright areas corre-

spond to the 7x7 domains. Figure 2 shows a plot of the area of several domains as a function of time. We find that the domains decay approximately linearly in time with a decay rate determined, not by the domain size, but by the local arrangement of neighboring domains. This observation is counter to the simplest picture of phase boundary motion, in which domain walls move with a constant velocity (independent of environment) determined by the free energy difference between the two phases. We have modeled the effect of this mass transport requirement on the observed decay by solving the two-dimensional diffusion equation for the experimentally observed configuration of 7x7 domains. From this analysis, we find that the decay is limited by the supply of additional material to the boundary. Moreover, the analysis is consistent with a model in which sources of adatoms are uniformly distributed on the surface. The model reproduces the simultaneous decay of all islands in the field of view with only one adjustable parameter (Fig. 2). The results lead us to conclude that random adatom-vacancy generation provides the source of material required for the transition to proceed.

Significance—This work identifies an important aspect of phase transitions that is difficult to address experimentally and therefore often overlooked. We were able to quantify the role of mass transport in surface phase transitions by observing the phase transformation as it occurs. In the process, we discovered a novel precipitation mechanism involving the random creation of adatom and vacancies at the surface and subsequent diffusion of the adatoms to the domain boundaries.

Sponsors for various phases of this work include: DP Research Foundations, BES Materials Sciences, and LDRD

Contact: Gary L. Kellogg, Surface and Interface Sciences Dept., 1114

Phone: (505) 844-2079, Fax: (505) 844-4045, E-mail: glkello@sandia.gov

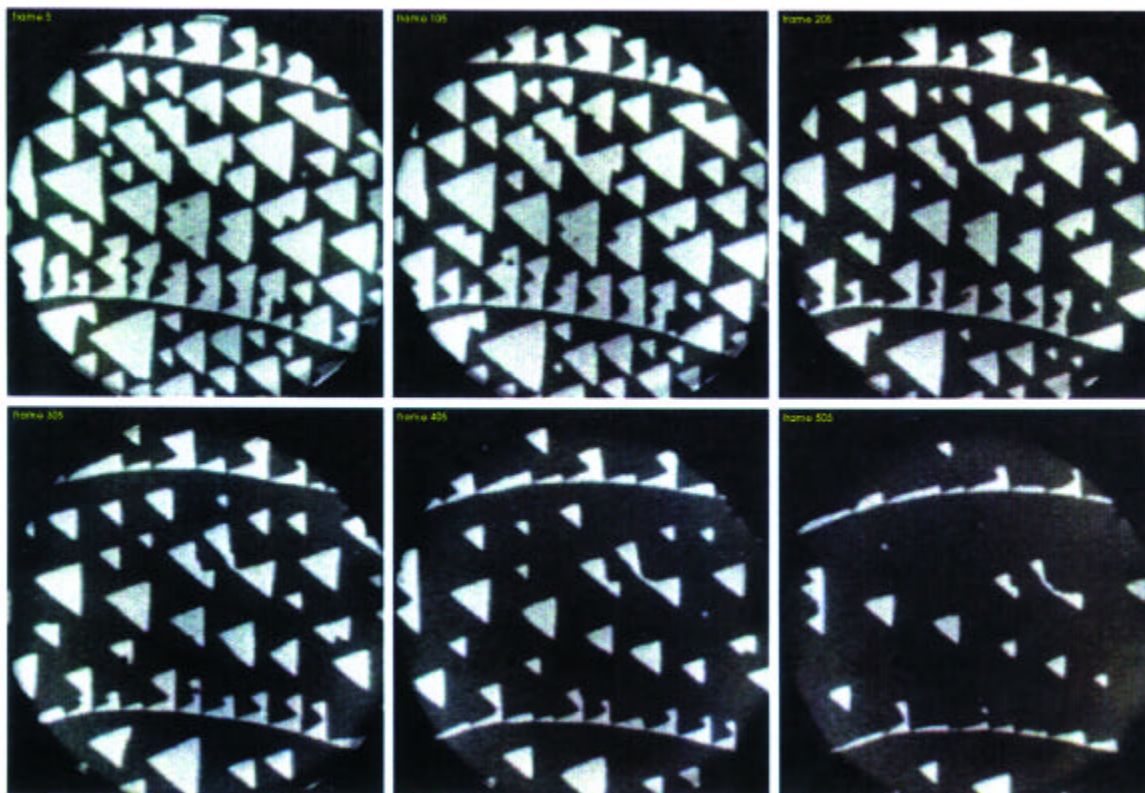


Figure 1. Low energy electron microscope images showing the decay of 7×7 domains during the 7×7 to 1×1 phase transition on Si(111). The field of view is 2.5 microns and the temperature is 830 C.

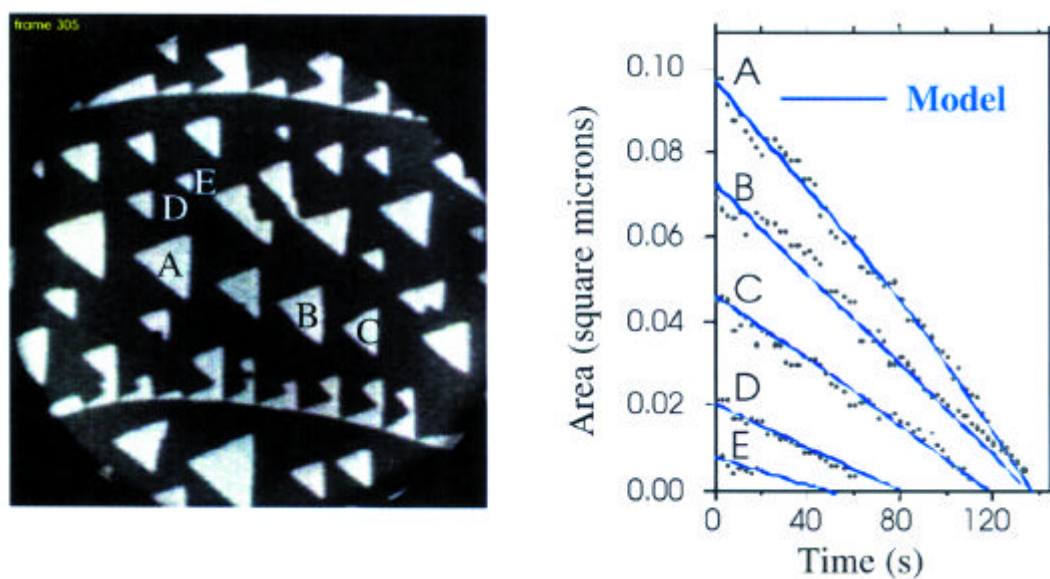


Figure 2. Decay rates for selected 7×7 domains. The LEEM image has a field of view of 2.5 microns. Dots are measured rates from LEEM images. Blue lines are fits from a diffusion equation model with one adjustable parameter.

Membrane-Based Sensors for Detecting Heavy Metal Ions

D. Y. Sasaki

Motivation—Biological cells communicate through a complex series of events that is processed at the cellular membrane. The process involves chemical signals, molecular recognition, molecular reorganization, and signal cascades. These systems are innately precise in chemical specificity, extremely sensitive, rapid in response, and able to detect multiple targets simultaneously - all attributes of an ideal sensor system. Using synthetically prepared, functionalized lipid bilayer membranes we have embarked on an effort to mimic these molecularly dynamic systems for sensor applications, and as an approach towards unique molecular-level architecture.

Accomplishment—Functionalized bilayer membranes composed simply of two lipid components have been prepared and exhibit rapid, highly sensitive, and selective optical response to heavy metal ions in aqueous solution. The fluorescence response is complete in about a second, having a limit of sensitivity at the sub-ppb range. The material can be recycled and readily configured to optical sensor platforms.

The observed fluorescence response is caused by a metal ion recognition event that induces reorganization of the lipid membrane. A synthetic lipid, prepared with a metal ion receptor at the headgroup position and a pyrene fluorophore in the tail, is mixed into a bilayer of distearylphosphatidylcholine (DSPC). Initially, the receptor lipids ($T_c < \text{r.t.}$) separate from the DSPC ($T_c > \text{r.t.}$) matrix forming pools of pyrene aggregates. Irradiation at 346 nm produces a dominant excimer (*excited state dimer*) population with an emission at 470 nm. Addition of metal ions results in ion recognition at the membrane surface, creating charged headgroups and

subsequent ionic repulsion between receptors. The recognition event thus disperses the pyrene aggregates, inverting the excimer/monomer population distribution. The monomer fluorescence at 377 nm increases with a concomitant decrease of the excimer emission. Figure 1 illustrates the process with the corresponding fluorescence spectra. Figure 2 shows color pictures of the metal ion response of the bilayers in solution.

Currently, we have prepared membranes with selectivity for Cu(II), Hg(II), and Pb(II) using iminodiacetic acid, dithioamides, and crown ethers, respectively, as the receptor sites. We have also demonstrated selective response for protein and polypeptides with similar materials.

To configure these self-assembled structures to optical sensor platforms we have developed methods of immobilizing the bilayers in silica sol-gel materials. Thin films and monoliths have been prepared and configured onto fiber optics.

Significance—These molecularly dynamic and chemically responsive materials described above demonstrate just some of the possibilities of cellular mimetic systems. The materials are readily tailored to sense any analyte of interest by simply manipulating the receptor site. And, with the growing interest in biosensors these bio-compatible materials are ideal platforms for biomolecule or cellular detection. Beyond sensor applications, we also hope to develop systems that use molecular recognition on self-assembled structures to prepare complex nanoscale architectures.

Sponsors for various phases of this work include: DP Research Foundations and LDRD

Contact: Darryl Y. Sasaki, Biomolecular Materials and Interfaces, 1115

Phone: (505) 845-0824, Fax: (505) 844-5470, E-mail: dysasak@sandia.gov

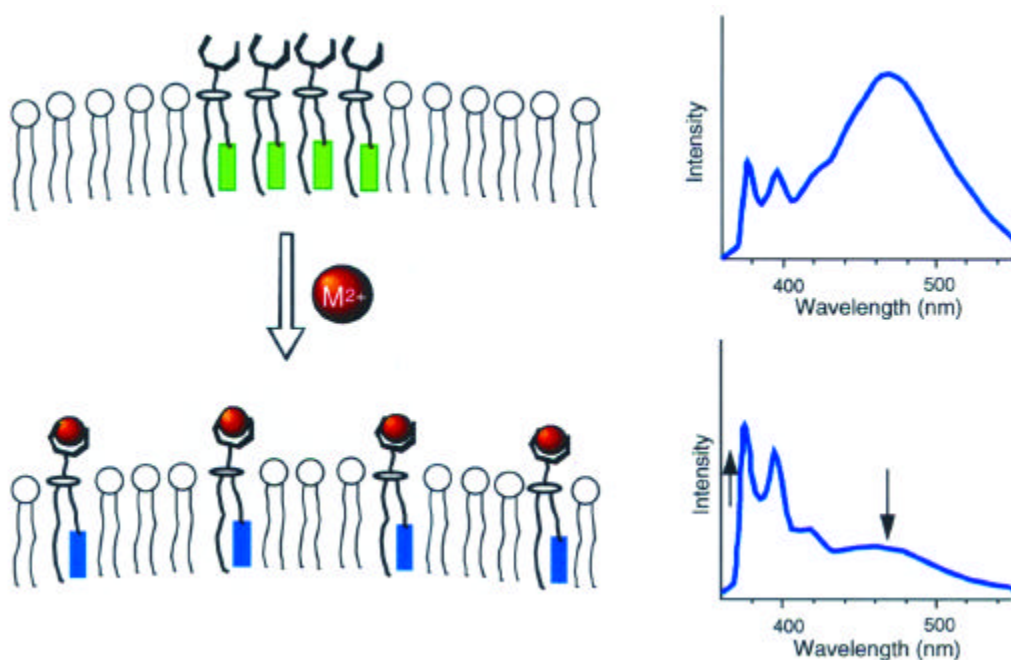


Figure 1. Upon metal ion recognition, initially aggregated receptor lipids disperse into the membrane matrix driven by ionic repulsion (left). The change in aggregational state is sensed by a pyrene fluorophore on the receptor lipid, resulting in an inversion of the fluorescence emission (right).

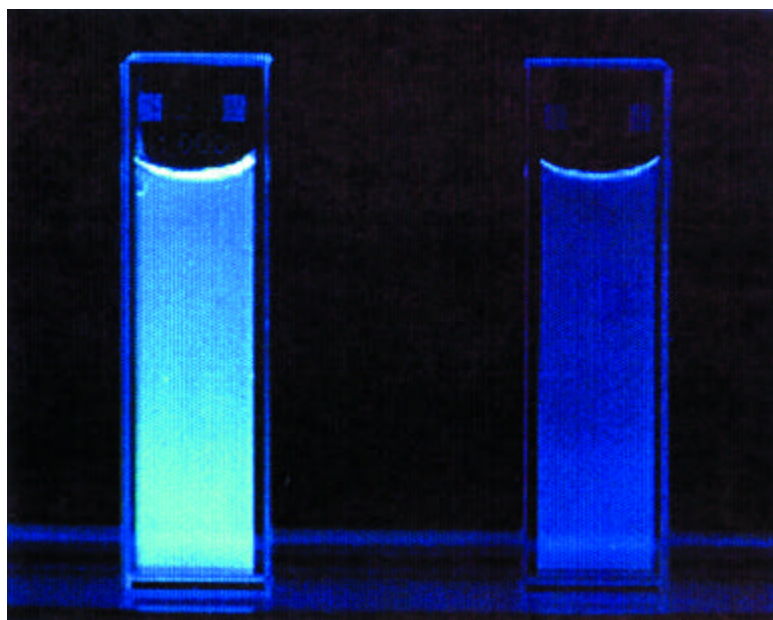


Figure 2. Fluorescence of the lipid bilayers before (left) and after (right) addition of $Cu(II)$ at sub-ppm concentration ($\lambda_{ex} = 366$ nm). Response is complete after one second.

Gallium Nitride Epitaxial Lateral Overgrowth Kinetics

M. E. Coltrin, M. E. Bartram, D. C. Willan, and J. Han

Motivation—Gallium nitride is a wide bandgap semiconductor with a broad range of potential applications, e.g., high-temperature electronics, optoelectronics, chemical and biological sensors, and multifunctional materials integration. Still, GaN is one of the most challenging compound semiconductor materials systems encountered to date. GaN thin films usually contain a high defect density, leading to poor device performance. Epitaxial Lateral Overgrowth (ELO) has been shown to dramatically reduce defect densities, often by 2 orders of magnitude or more. We are conducting fundamental studies of GaN crystal growth kinetics during ELO.

Accomplishment—In ELO, a mask pattern of dielectric material, for example silicon nitride, is deposited on top of a GaN buffer layer. Further growth of GaN occurs selectively on exposed areas of the underlying buffer layer, and not on the dielectric material. Many coupled phenomena potentially contribute to observed ELO behavior, including mass transport, anisotropic growth kinetics, and thermodynamics.

We have designed a custom mask to examine ELO growth kinetics over a wide range of patterning dimensions. Cross-sectional areas of grown features are obtained by scanning electron microscopy (SEM), and are used to study growth kinetics. Results from two deposition runs are plotted in Fig. 1. A wide range of apparent growth kinetics is observed, and a way of systematizing the data must be found. The growth rate on exposed regions depends strongly on the mask pattern, i.e., the size of the exposed window opening (W) and the pitch (P), the repeat distance of the pattern. Because growth does not occur on masked areas, a

growth rate enhancement is observed on the unmasked regions due to lateral mass transport. A finite-element diffusion model shows that the lateral transport of material should have near-unit efficiency. Thus, the cross-sectional area A_i of a feature is expected to increase linearly with the pattern pitch P_i . That is, essentially all of the material that would have deposited over the length P_i (if there had been no mask) ends up contributing to A_i .

In the simplest model, A_i is expected to be proportional to the (unmasked) growth rate, G_o , and the deposition time, t . We propose that features of differing size are self-similar when the proper length scale is used, which we recognize as the exposed window size, W_i . Our new ELO theory predicts that scaled area $a_i \equiv A_i/W_i^2$ should equal $G_o * P_i * t / W_i^2$, which we define as a dimension-less growth time τ_i . Thus, a plot of a_i vs τ_i should yield a straight line. The original data is replotted in this way in Fig. 2, with the solid line representing the ideal, theoretical slope of one. The results are shown as a log-log plot to better display the data, which ranges over 3 orders of magnitude.

Significance—These results have important implications for understanding GaN ELO. Agreement between model and experiment shows that lateral transport from the masked to the exposed regions is essentially 100% efficient. From the discovery that the growth features are self-similar when scaled by the correct length scale W_i , we have found a quantitative way to translate results from different pattern dimensions into a pseudo time basis. This allows us to study a wide range of growth kinetics in a single growth run, i.e., in a "combinatorial" manner.

Sponsors for various phases of this work include: BES Materials Sciences and LDRD

Contact: Michael E. Coltrin, Chemical Processing Sciences Dept., 1126

Phone: (505) 844-7843, Fax: (505) 844-3211, E-mail: mecoltr@sandia.gov

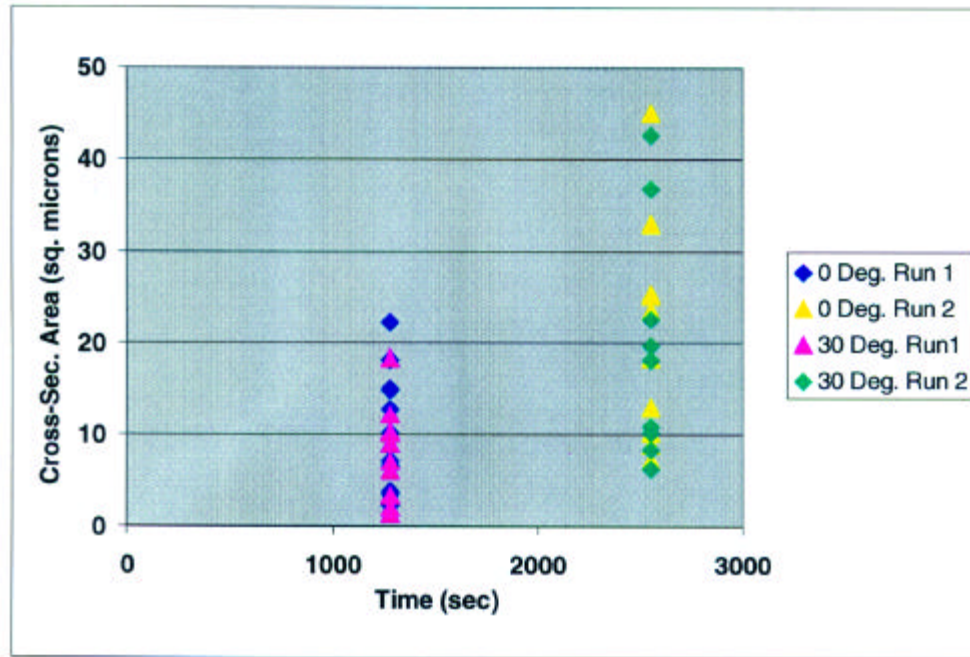


Figure 1. Cross-sectional area of GaN ELO growth features for a wide range of pattern sizes, and two separate growth runs. Line are oriented 0 or 30 degrees with respect to the sapphire substrate.

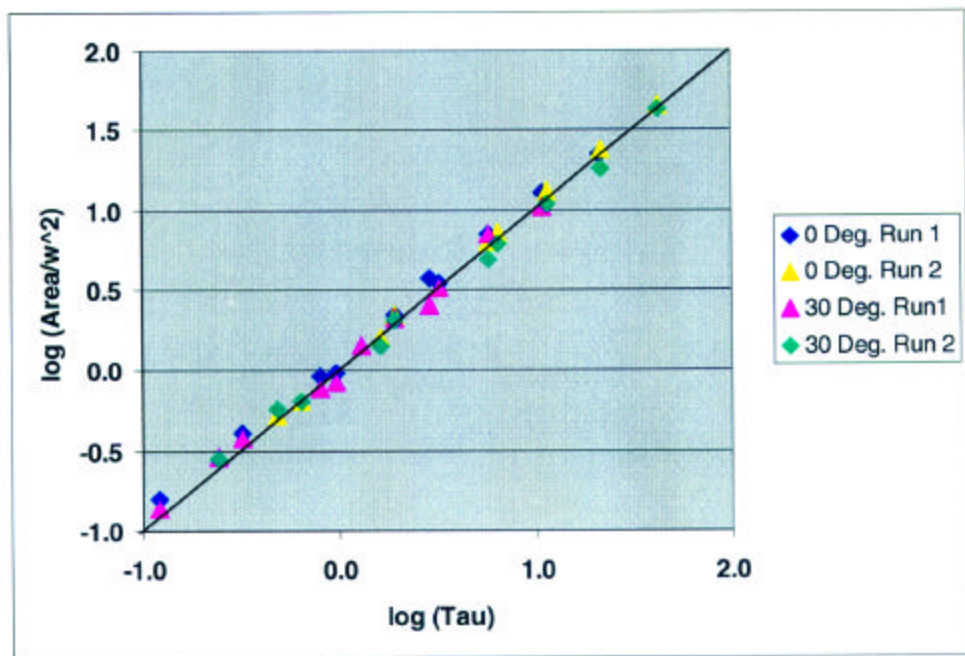


Figure 2. Cross-sectional area scaled by the exposed deposition window width as a function of the dimensionless "time" derived in the text.

Divertor Erosion Eliminated by Using Detached Plasmas on DIII-D

W. R. Wampler

Motivation—Present designs for a Tokamak fusion reactor (for example the International Thermonuclear Experimental Reactor) specify graphite or carbon composites for the divertor strikeplates, which are the regions of most intense interaction with the plasma. The choice of carbon is dictated by the requirement to withstand extreme pulsed heat fluxes during plasma disruptions. Graphite tiles are also widely used in presently operating Tokamaks for this reason. Our studies in the DIII-D tokamak show that the graphite divertor is eroded by the plasma at rates of 10 nm/sec or more (shown in Figs. 1 and 2) which translates to about 30 cm per burn-year. This erosion by the plasma results in two serious problems for a fusion reactor. The first is the short lifetime of a graphite divertor in a reactor. The second problem is a large in-vessel tritium inventory resulting from the fact that the eroded carbon is deposited elsewhere inside the tokamak, along with high concentrations of deuterium and tritium from the plasma. These effects have had little impact on operation in present tokamaks due to their low duty cycle, except during tritium fueled plasma experiments in TFTR and JET. However, in a high duty cycle reactor the erosion rate becomes centimeters per month requiring frequent component replacement. In present Tokamaks about half the deuterium and tritium used to fuel the plasma remains inside the vessel codeposited with carbon. In a reactor such as ITER, this rate of tritium retention would result in a tritium inventory exceeding a kilogram after less than a month of operation which is unacceptable.

Accomplishment—Our recent measurements of erosion in the DIII-D Tokamak show a possible solution to all the problems described above. We found that by operating in a mode

where the plasma is detached from the divertor, erosion in the divertor is eliminated. Detached plasmas are produced by injecting deuterium gas in the divertor, which increases the density and reduces the temperature of the plasma to ~ 2 eV and greatly increases ion-electron recombination in the divertor. The low energy of ions and neutrals impinging on the divertor results in very low erosion or net deposition of material as shown in Fig. 2. With attached plasmas, ions reach the surface with much higher energies of hundreds of eV giving high erosion rates at the strikepoints. The erosion rates were measured using the Divertor Materials Evaluation System (DiMES) on the DIII-D Tokamak. With this facility samples can be exposed at the divertor to well defined plasmas and then removed for analysis. Erosion or deposition of carbon is determined from the shift in depth of a subsurface marker measured by ion-beam analysis before and after the Tokamak plasma exposure. Deuterium retention is also measured by ion-beam analysis. These experiments are conducted by the DiMES team consisting of W.R. Wampler and R. Bastasz, at Sandia, D.G. Whyte, at the University of California at San Diego and C.P.C. Wong, and W.P. West at General Atomics.

Significance—A practical fusion reactor design will open the door to a new long-term energy resource, which also reduces fossil fuel consumption and associated atmospheric pollution by carbon dioxide. Our experiments show that operation with detached plasmas avoids erosion of a carbon divertor and the resulting short divertor lifetime and large tritium inventory. These results show how to overcome a major obstacle in designing a fusion reactor.

Sponsors for various phases of this work include: Fusion Energy Sciences

Contact: William R. Wampler, Radiation-Solid Interactions Dept., 1111

Phone: (505) 844-4114, Fax: (505) 844-7775, E-mail: wrwampl@sandia.gov

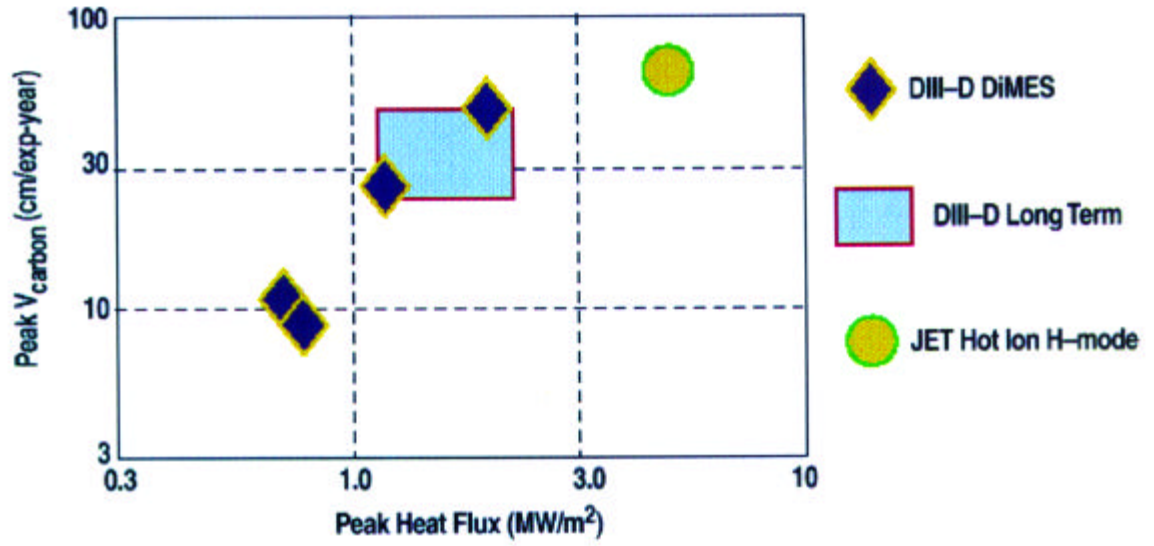


Figure 1. Peak carbon erosion rates measured by DiMES (diamonds), and from long-term changes in divertor geometry in DIII-D and JET for normal attached divertor operation.

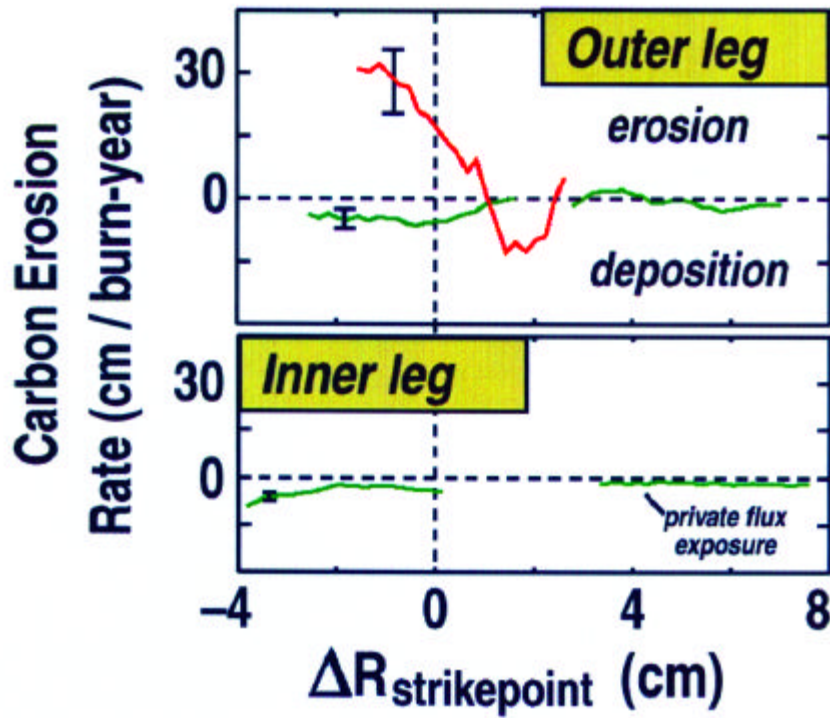


Figure 2. Carbon erosion measured by DiMES at the inner and outer strikepoints and in the "private flux" region between strikepoints for attached (red) and detached (green) plasmas. No erosion is seen for detached plasmas.

Mechanical Properties of Alumina Films are Correlated Primarily to Film Density

J. C. Barbour, J. A. Knapp, and D. M. Follstaedt

Motivation—This work developed an approach to predicting the mechanical properties of thin, oxide-ceramic films, which are often difficult to measure by conventional bulk-sample techniques. It was discovered that the properties of the film could be predicted from bulk properties but by scaling the density down from the bulk to that measured for the thin film.

Accomplishment—For the first time, the mechanical properties of thin alumina films were shown to correlate directly to film density. The mechanical properties varied as a linear and nearly unique function of film density, irrespective of both phase and hydrogen content. The more dense alumina films have a greater hardness, yield strength and Young's modulus of elasticity: a 25% decrease in density was found to reduce the yield strength by a factor of four and the Young's modulus by a factor of three. The density of a sample may be changed by the accumulation of point defects and void space. Hydrogen may help stabilize the lower density structures, but density appears to be the primary parameter determining the mechanical properties of alumina. Nanoindentation was performed to determine the elastic modulus, hardness and yield strength of amorphous and g-phase alumina films formed by electron cyclotron resonance plasma deposition, and of bulk a-phase and an amorphized layer formed by ion irradiation of a-phase alumina. Finite element analysis was used to simulate the effects of porosity (reduced density) on the hardness and strength of alumina films, and showed that a

reduction in density could cause the large reductions observed for the films used in this study. This work provides a better understanding of the parameters which govern the mechanical properties of thin-film and bulk alumina.

Significance—A physics-based understanding of the mechanical properties of thin-film ceramics is required to predict the mechanical reliability of films used as wear resistant and corrosion resistant coatings. The fact that alumina can be formed with densities varying over a 25% range, producing a factor of 4 difference in yield strength, has profound consequences for the use of alumina as a wear-resistant coating. Also, Al corrosion passivation layers are generally low-density, high-H content alumina layers and this work indicates that a high density alumina coating would have superior mechanical strength and be less susceptible to bubble rupture during pitting and corrosion. Knowledge of thin-film mechanical properties has previously been limited because of the difficulty in performing mechanical tests on thin films. In order to have a significant impact on the broad area of high-strength coatings, the first priority is to understand the key parameters governing the mechanical properties of a coating, which in this case is the density. The second objective is then to quantify the relationship between the mechanical properties and the more readily measured density. These findings are expected to be applicable to the broad class of thin-film oxide ceramics.

Sponsors for various phases of this work include: BES Materials Sciences and DP Research Foundations
Contact: J. Charles Barbour, Radiation Solid Interactions and Processing Dept., 1111
Phone: (505) 844-5517, Fax: (505) 844-7775, E-mail: jcbarbo@sandia.gov

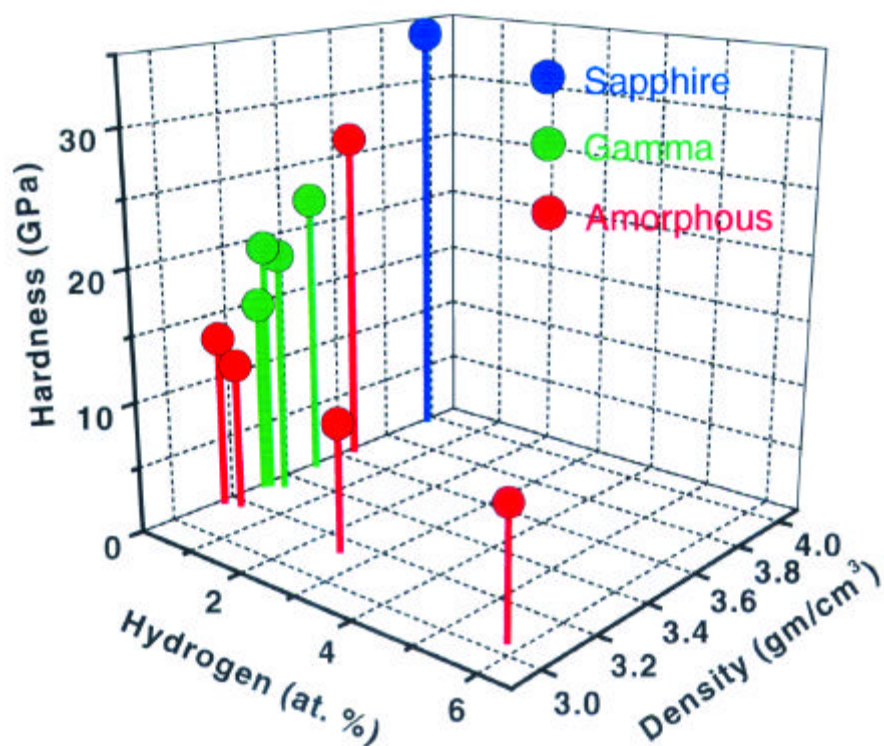


Figure 1. Controlled synthesis using energetic ions allows for exploration of the matrix of hardness, strength and Young's modulus as a function of phase, hydrogen content, and density.

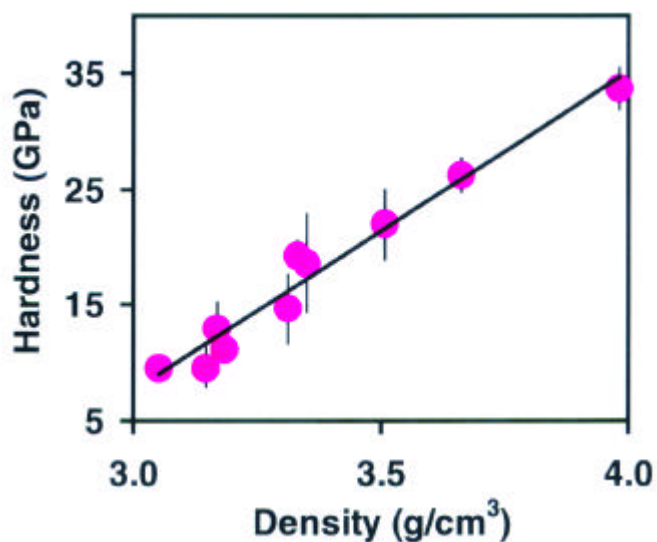


Figure 2. Unifying Relationship: The density of the alumina film determined the resultant hardness. Further, the ultimate density, which is given by bulk sapphire, obeys the same relationship.

Electrostriction in Field-Structured Composites: Basis for an Artificial Muscle?

J. E. Martin and R. A. Anderson

Motivation—There are a number of applications for electromechanical actuators that can exhibit deformations far in excess of those of piezoelectric materials. Such actuators could replace hydraulic actuators in many applications, eliminating the necessity for fluid pumps, flexible fluid couplings, etc. Current concepts are based on materials such as electromotive polyelectrolyte gels, which deform in the presence of small applied voltages, due to the migration of ions into the gel. However, electromotive gels are mechanically weak, and the response time is both large (>1 s) and size dependent, since water must diffuse out of the gel for it to deform. We have developed and explored a different concept, based on the electric-field-induced dipolar interactions of submicron size particles preorganized into column- or sheet-like structures in a polymer, (Fig. 1). These tough field-structured composites (FSCs) should respond on submillisecond timescales, and should exhibit large strain deformations.

Accomplishment—We have completed an analysis of electrostriction in particle/elastomer composites. This treatment is for the case of contacting parallel electrodes, and is based on the change in the electrostatic energy of a capacitor, in the point dipole, self-consistent field approximation, subjected to strains along principal axes. Measurements of the effective susceptibilities of FSCs demonstrate that this

approach is reasonable. We consider various lattice packings of particles, as well as FSCs produced from Brownian dynamics simulations, (Fig. 2). In all cases the electrostriction effect increases rapidly with the effective dielectric constant of the composite, and the largest electrostriction effect was found for the body-centered tetragonal lattice, which is the electrostatic ground state for a uniaxial FSC. For simulated uniaxial FSCs, we found that the electrostriction effect is 3-5 times larger than that of a random particle dispersion - depending on the particle concentration - and increases with particle concentration (Fig. 3). The effect is independent of particle size, which is not obvious, since the induced dipole moment increases as the cube of the particle size.

Significance—These calculations demonstrate that FSCs are promising candidates as artificial muscles. The stress response should be the polarization time of the particles, which can be exceedingly short for particles having an intrinsic polarization mechanism, such as incipient ferroelectric particles. Future directions for this research include electrostriction measurements, and the consideration of the more complex case where the composite material does not contact the electrodes. This case is relevant to the magnetostriction of magnetic particle FSCs, where it would not be convenient to have the material contact the magnetic poles.

Sponsors for various phases of this work include: BES Materials Sciences

Contact: James E. Martin, Nanostructures and Advanced Materials Chemistry, 1152

Phone: (505) 844-9125, Fax: (505) 844-4045, E-mail: jmartin@sandia.gov

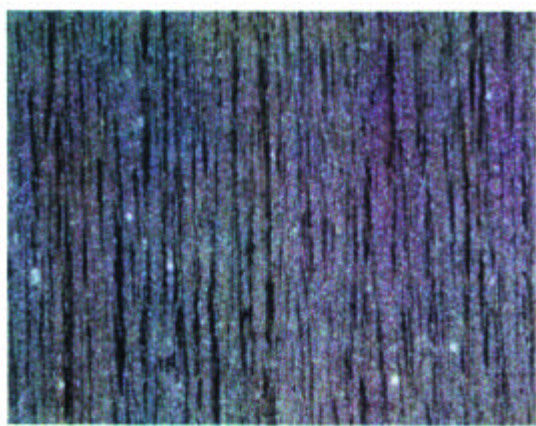


Figure 1. A uniaxial FSC of micron size particles. The structuring field was vertical.

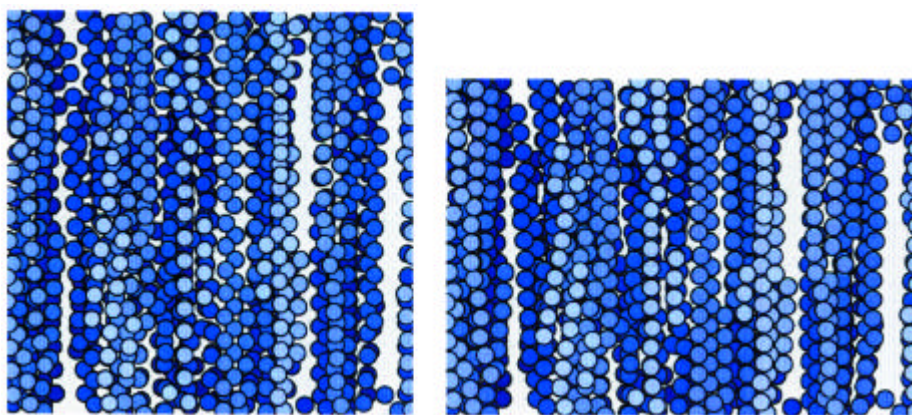


Figure 2. A simulated uniaxial FSC compresses in the vertical direction when a field is applied along this axis. The expansion is due to the incompressibility of the polymer.

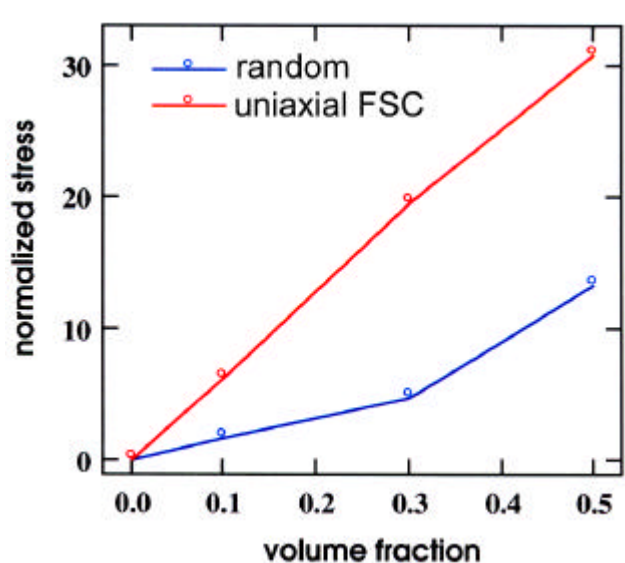


Figure 3. Compressive stress normalized by the Maxwell stress vs. particle volume fraction.

Recent Awards & Prizes



Recent Awards and Prizes

National and International Awards

- 1999 — American Chemical Society Earle B. Barnes Award for outstanding leadership in chemical research management: "For visionary leadership in managing laboratory and inter-laboratory research in the National interest at the frontiers of materials science."
(George A. Samara)
- 1997 — Peter Mark Award for "Pioneering studies of atomic-scale, kinetic and thermodynamic aspects of the morphology of Si surfaces, and significant innovations in scanning tunneling microscopy that make such measurements possible" - American Vacuum Society
(B. S. Swartzentruber)
- Edward Orton, Jr., Memorial Lecturer Award - American Ceramics Society
(T. A. Michalske)
- 1996 — DOE Young Independent Scientist Award (B. S. Swartzentruber)
- The Medard W. Welch Award for "His insightful predictions and explanations of surface phenomena based on first principles calculations" - American Vacuum Society
(P. J. Feibelman)
- 1993 — International New Materials Prize for "Originating the Field of Strained-Layer Superlattice Electronics and Optoelectronics" - American Physical Society (G. C. Osbourn)
- Shock Compression Science Award - The American Physical Society (R. A. Graham)
- 1990 — E. O. Lawrence Award, Materials Science - DOE (S. T. Picraux)
- 1989 — Davisson-Germer Prize "For his pioneering work in developing the theory of electromagnetic fields at surfaces" - American Physical Society (P. J. Feibelman)
- Weyl International Glass Science Award - International Glass Commission
(T. A. Michalske)

DOE Basic Energy Sciences, Material Science Awards

- 1998 — Sustained Outstanding Research--Condensed Matter Physics "Quantitative Measurements and New Mechanisms of Atom and Cluster Diffusion on Surfaces" (G. L. Kellogg)
- Significant Implications for DOE Related Technologies--Condensed Matter Physics "Semiconductor Materials Science Enables a Biological Microcavity Laser for Early Detection of Disease" (P. L. Gourley, M. H. Crawford, W. Chow, M. Sinclair and A. E. McDonald)
- 1996 — Outstanding Scientific Accomplishment--Solid State Physics "Development of Atom-Tracking Scanning Tunneling Microscopy for Direct Measurements of Surface Dynamics" (B. W. Swartzentruber)
- Significant Implication for Department of Energy Related Technologies--Materials Chemistry "Nanoclusters for Energy Applications" (J. P. Wilcoxon, P. P. Newcomer, D. E. Bliss, G. A. Samara, and A. Martino)
- 1994 — Sustained Outstanding Research--Solid State Physics "Surface Atom Energetics" (P. J. Feibelman)

-
- Sustained Outstanding Research--Metallurgy and Ceramics "Science of Surface Processes in Beam-Enhanced Growth" (E. Chason, J. Y. Tsao, J. A. Floro, K. M. Horn, T. M. Mayer, P. Bedrossian, D. K. Brice, A. J. Howard, S. T. Picraux, D. L. Buller, and K. J. Penn)
 - Significant Implication for Department of Energy Related Technologies--Materials Chemistry "Real Time, In Situ Materials Growth Monitors Using Remote Optical Probes" (K. P. Killeen, S. A. Chalmers, W. G. Breiland, and T. M. Kerley)
 - 1993 — Sustained Outstanding Research--Metallurgy and Ceramics "Strained Layer Superlattices and Artificially Structured Semiconductors" (P. Gourley, I. Fritz, E. Jones, K. Lyo, J. Nelson, R. Schneider, G. Osbourn, B. Biefeld, and R. Dawson)
 - Significant Implication for Department of Energy Related Technologies--Metallurgy and Ceramics "Interfacial Force Microscope" (J. Houston and T. Michalske)
 - 1992 — Sustained Outstanding Research--Materials Chemistry "CVD Sciences" (W. G. Brieland, M. E. Coltrin G. H. Evans, P. Ho, and R. Kee)
 - 1991 — Sustained Outstanding Research--Metallurgy and Ceramics "Advanced Ion Beam Techniques for Materials Analysis" (B. L. Doyle, S. T. Picraux, J. A. Knapp, and S. M. Myers)
 - Outstanding Scientific Accomplishment--Solid State Physics "Surface Diffusion by Atomic Substitution" (G. L. Kellogg and P. J. Feibelman)
 - Significant Implication for Department of Energy Related Technologies--Metallurgy and Ceramics "Exceptionally High-Strength Aluminum Alloys" (D. M. Follstaedt, R. J. Bourcier, M. T. Dugger, and S. M. Myers)
 - 1990 — Sustained Outstanding Research--Metallurgy and Ceramics "Model of Hydrogen-Defect Interactions in SiO₂ and at the SiO₂-Si Interface" (K. L. Brower, S. M. Myers, P. M. Richards, and H. J. Stein)
 - 1989 — Significant Implication for Department of Energy Related Technologies--Solid State Physics "Development of Tl-Ca-Ba-Cu-O High Temperature Superconducting Thin Films and Demonstration of Novel High-Performance Devices" (R. J. Baughman, D. S. Ginley, J. F. Kwak, B. Morosin, and E. L. Venturini)

Other Awards

- 1998 — Technology of the Year Award, Industry Week Magazine for the Double Electron Layer Tunneling Transistor (J. A. Simmons)
- NM Software Author of the Year Finalist (M. E. Coltrin)
- 1997 — R&D Award for "Development of a Biological Microcavity Laser" (P. L. Gourley)
- R&D Award for "For Development of the Filmetrics F30" (W. G. Breiland)
- 1995 — Norbert J. Kreidl Award from the New Mexico Ceramics Society Glass Division (K. S. Simmons-Potter)
- 1994 — R&D 100 Award for "Interfacial Force Microscope" (J. E. Houston and T. A. Michalske)
- 1993/
- 1994— J. J. Thomson Award for "Temporal and Spectral Gain Dynamics in an Actively Mode-locked Semiconductor Laser" (W. W. Chow)

Resources and Capabilities



Resources and Capabilities Physical and Chemical Sciences Center

-- Diagnostics and Characterization --

Atomic-Level Imaging and Spectroscopy

We have developed technical capabilities in:

- Scanning Tunneling Microscopy (STM) with the ability to track the diffusion of single atoms on surfaces;
- Low Energy Electron Microscopy (LEEM) in terms of spatial resolution and spectroscopic imaging capability;
- Field Ion Microscopy (FIM) in terms of single atom resolution and accurate temperature control to 1 Kelvin;
- Atom Probe Microscopy (APM) in terms of pulsed laser desorption capability; and
- Interfacial Force Microscopy (IFM) with feedback for accurate force profile measurements.

Simultaneous Measurement of H, D, and T in Materials

We have designed and implemented a new ion beam analysis (IBA) system to simultaneously measure the absolute quantities of H, D, and T in materials using an elastic recoil detection (ERD) technique. The technique uses an E-dE detector arrangement, or particle telescope, to provide for accurate separation of the H, D, and T signals. The system can also simultaneously acquire information about medium and high Z elements in the sample using Rutherford backscattering spectrometry (RBS). Measurement of other light elements is possible using the nuclear reaction analysis (NRA) technique, which is isotope specific. The system will have an accuracy of < 2% for measuring the composition of solids.

Ion Accelerator Nuclear Microprobe

We have facilities for nuclear microscopy and radiation effects microscopy based on a 6 MV tandem Van de Graaff ion accelerator. We generate ion species from hydrogen to bismuth

for both radiation effects research and quantitative high-energy ion beam analysis of materials containing light elements (hydrogen to fluorine) using heavy ion elastic recoil detection (ERD) and heavy elements using high-energy backscattering spectrometry, and Heavy Ion Backscattering (HIBS) (Includes Patent 3 5059785 issued October, 1991). An external Micro Ion Beam Analysis (X-MIBA) capability enables multi-elemental analysis and ion irradiation of samples which are vacuum incompatible or extraordinarily large. The Sandia Nuclear Microprobe with micrometer size high energy ion beams is used to study materials and devices. Special emphasis is given to the evaluation of the radiation hardness of microelectronic devices using three new advanced diagnostic techniques invented at Sandia: Single-Event-Upset Imaging, Ion-Beam-Induced-Charge-Collection Imaging (IBICC), and time-resolved IBICC.

Materials Microcharacterization

Our capabilities in this area include optical microscopy, scanning, electron microscopy, analytical transmission electron microscopy, double crystal x-ray diffraction, ion beam analysis of materials (RBS, channeling, ERD, PIXE, NRA), Hall measurements, microcalorimetry, photoluminescence, light scattering, electronic transport, deep level spectroscopy, magnetization, and dielectric and magnetic susceptibilities.

Surface and Interface Spectroscopies

We maintain strong capabilities in Auger electron spectroscopy (AES), x-ray photoelectron spectroscopy (XPS), low energy electron diffraction (LEED), ultraviolet photoelectron spectroscopy (UPS), thermal desorption spectroscopy (TDS), infrared reflectance-absorption spectroscopy (IRAS), and quantum state resolved laser surface probes.

Vision-Science Laboratory

The vision science laboratory consists of state-of-the-art hardware and software capabilities for carrying out video inspection, multi-spectral image analysis, and sensor-based pattern recognition. (Includes Imaging Processing System, Patent # 5495536.) These capabilities are used in applications ranging from microsensor-based chemical detection and recognition to automated video/SEM inspection of semiconductor materials and circuits. (Patent applied for December, 1996 for “a new cluster analysis method”). This is a new approach to pattern recognition, coupling perception-oriented research with machine algorithms.

Chemical Vapor Deposition (CVD)

Our experimental tools for investigating CVD include optical probes (such as reflectance-difference spectroscopy) for gas-phase and surface processes, a range of surface analytic techniques, molecular beam methods for gas/surface kinetics, and flow visualization techniques. These tools are integrated in a unique manner with research CVD reactors and with advanced chemistry and fluid models.

Growth Science Laboratory

Capabilities for in situ characterization of materials during thin film deposition, molecular beam epitaxial growth, and low energy ion beam simulated growth, include intensity profile sensitive reflection high energy electron diffraction (RHEED) for surface structure, energy dispersive x-ray reflectometry for in situ surface and interface structure, multibeam wafer curvature for strain (Patent filed 1997), and Auger electron spectroscopy for surface composition.

KMAP X-ray Diffractometer

Based on double crystal x-ray diffractometry in combination with position sensitive x-ray detection, our KMAP x-ray diffraction analysis is used to determine the lattice constant, strain relaxation, composition, layer orientation, and mosaic spread for a large variety of advanced epitaxial semiconductor material systems.

Nanoelectronics Laboratory

We have the capabilities for fabrication of nanoscale quantum device structures together with capabilities for ultra-low-noise measurement of transport from 0.3 Kelvin to ambient at high magnetic fields.

Lasers and Optics

We provide characterization and advanced understanding in the area of solid-state lasers and non-linear optics, especially as coherent sources of broadly tunable light in rugged, compact geometries. We also have established expertise in long-term and transient radiation effects characterization of optical materials. (Includes patented Wavefront Sensor Patent 3 5493391, and Monolithic Optical Amplification Devices Patent # 5463649). Capabilities include the combined modeling and laboratory validation of the performance of non-linear optical materials as well as their radiation response characterization (pulsed nuclear reactor, and X-ray generators).

Laser and Optical Spectroscopies

Our capabilities in characterizing semiconductor materials by photoluminescence and magnetoluminescence extend down to low temperatures by optical laser imaging and laser microscopy, by laser excitation spectroscopy, and by the time-resolved measurements of optical emission. We also have developed a high lateral resolution, near-field scanning optical microscopy (NSOM) capability with time and frequency resolution. (Patent filed June, 1994 for Chemical Recognition Software.)

Low-Temperature Plasma Analysis

We have state-of-the-art capabilities for the analysis of low-temperature plasmas as found in commercial processing reactors. These include emission spectroscopy, electrical characterization, laser and microwave-based measurements of species concentrations, in situ electric field measurements, and others. Sandia is the only lab which combines new diagnostics, relevant process chemistries (complex mixtures), and massively parallel (MP) computer models for simulation of continuous and transient plasmas.

-- Synthesis and Processing --

Nanocluster Laboratory

We have developed and patented a process based on the use of inverse micelles for the synthesis of large quantities of monodisperse clusters of metals, semiconductors, and oxides.

Electron Cyclotron Resonance (ECR)

This plasma facility has been built for studying fundamental processes governing the growth of oxide and nitride dielectric films used in optoelectronics and used as hard coatings. This is the only system in the U.S. which combines ECR plus e-beam evaporation.

Molecular Beam Epitaxy (MBE)

We have research semiconductor growth laboratories for ultra-pure and ultra-flexible MBE growth of III-V materials. In addition, we have research systems for Group IV semiconductor growth.

Metal-Organic Chemical Vapor Deposition (MOCVD)

We maintain research facilities with capabilities in MOCVD of compound semiconductor materials. These capabilities include research reactors designed specifically for studies of CVD chemistry, fluid dynamics, the development of advanced in situ diagnostics, and the development of advanced semiconductor heterostructures.

Crystal and Thin Film Growth

Capabilities in this area include a pulsed laser deposition chambers, a high vacuum metal deposition chamber, a thin film oxide deposition chamber, a diamond-like carbon deposition chamber, a hot filament chemical vapor deposition chamber, and various apparatus for single crystal growth. Our capabilities for stress relief of diamond-like carbon films and structures produced by pulsed laser deposition are not available elsewhere.

400 kV and 180 keV Ion Implanters

These systems are equipped with a variety of sources (gas, sputter, and metal vapor). This facility provides ion species from hydrogen to bismuth which can be used for studying fundamental irradiation mechanisms and selective chemical doping in semiconductors, metals, ferroelectrics, and superconductors.

High Pressure and Shock Wave Physics and Chemistry Laboratories

Our capabilities in this area include large volume static high pressure apparatus which can be operated at temperatures ranging from 2° to 700° K and in magnetic fields, as well as gas gun and explosive loading facilities with state-of-the-art, time-resolved diagnostics. Recovery fixtures have been developed for use with the gas gun and explosive shock loading facilities which allow unique material synthesis over broad ranges of shock pressures and temperatures.

-- Theory and Simulation --

Electronic Structure and Linear Scaling

We have developed state-of-the-art massively parallel electronic structure algorithms, based on *ab initio* pseudopotentials and plane-wave/Gaussian basis functions. These codes are used to develop a fundamental understanding of physical phenomena and materials, including compound semiconductor band structure, diffusion of point defects, dopants and impurities, optoelectronic properties of extended defects, adsorbate interactions on surfaces, bonding at metal-oxide interfaces, and enhanced reactivity of nanoparticles. To allow the investigation of more complex systems and phenomena, we have developed new computationally efficient algorithms, e.g., self-consistent linear scaling density functional theory, and variable and real-space gridding.

Chemical Processes

We have extensive capabilities, including massively-parallel computation, to model complex chemically reacting flows such as occur in chemical vapor deposition manufacturing processes. Our numerical simulations can include the coupled gas-phase and gas-surface chemistry, fluid dynamics, heat, and mass transfer to provide predictive models of a chemical process.

Low-Temperature Plasmas

We have extensive capabilities in massively parallel codes to simulate the time and space evolution of low-temperature plasmas, focusing on new theoretical techniques for achieving rapid convergence and on direct comparisons with experimental results.

Optical and Wave Propagation

We have developed advanced simulation codes for understanding wave propagation in optical parametric oscillators and amplifiers for the purpose of designing highly efficient, tunable laser sources. We also have capabilities in novel optical designs, including resonators for compact laser geometries. These capabilities are coupled to in-house micro-optics construction facilities and state-of-the-art optics testing.

Physical and Chemical Sciences Center FY00 Budget-By Customer

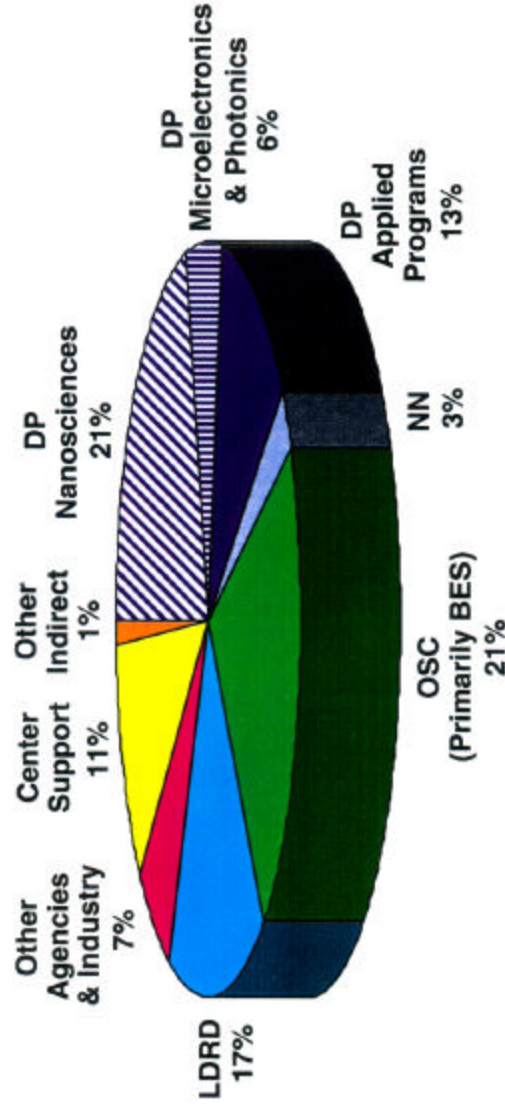


Physical and Chemical Sciences Center FY00 Budget - By Customer

Capital (\$1.3M)



Operating (\$28M)*



*Excludes major NN pass-through item.

SAND2000-0933: Prepared by Sandia National Laboratories, Albuquerque, New Mexico 87185 and Livermore, California 94550. Sandia is a multiprogram laboratory operated by Sandia Corporation, a Lockheed Martin Company, for the United States Department of Energy under Contract DE-AC04-94AL85000

Printed April 2000
